Li/S accumulators : Electrochemical mechanism investigation using operando analysis by absorption and X-Ray diffraction tomography

Guillaume Tonin

Communauté
UNIVERSITÉ Grenoble Alpes

THÈSE

Pour obtenir le grade de

DOCTEUR DE LA COMMUNAUTE UNIVERSITE GRENOBLE ALPES

Spécialité : **Matériaux, Mécanique, Génie Civile, Electrochimie**

Arrêté ministériel : 25 mai 2016

Présentée par

Guillaume TONIN

Thèse dirigée par **Fannie ALLOIN, Directeur de recherche, LEPMI**, et
codirigée par **Céline BARCHASZ, Ingénieur-Chercheur, CEA-LITEN**, et par **Gavin VAUGHAN, Ingénieur-Chercheur, ESRF**

préparée au sein du **Laboratoire Matériaux (LITEN) et de la Ligne Chimie et Génie des matériaux (ESRF) et du Laboratoire d'Electrochimie et de Physicochimie des Matériaux et Interfaces (LEPMI),**
dans **l'École Doctorale I-MEP²**

Caractérisation *operando* des accumulateurs Li/S par tomographie d'absorption et diffraction des rayons X, vers une meilleure compréhension des mécanismes électrochimiques

Thèse soutenue publiquement le **5 juin 2019**,
devant le jury composé de :

Monsieur Lorenzo STIEVANO
Professeur, ICGM, Montpellier, Rapporteur
Monsieur Mathieu MORCRETTE
Ingénieur de recherche, LRCS, Amiens, Rapporteur
Madame Claire VILLEVIEILLE
Chercheur, Examinateur
Monsieur Renaud BOUCHET
Professeur, LEPMI, Grenoble, Président
Madame Fannie ALLOIN
Directeur de recherche, LEPMI, Grenoble, Directeur de thèse
Madame Céline BARCHASZ
Ingénieur-Chercheur, CEA-LITEN, Grenoble, Co-encadrant de thèse
Monsieur Gavin VAUGHAN
Ingénieur-Chercheur, ESRF, Grenoble, Co-encadrant de thèse

Remerciements

La toute fin de rédaction de ce manuscrit est dédiée à l'écriture des remerciements. Ces remerciements s'adressent à toutes les personnes qui ont participé et contribué, de près comme de loin, à ce travail. Sans elles, ce travail ne serait pas à la hauteur de celui présenté ici. Ces quelques mots sont bien peu pour vous témoigner ma plus sincère reconnaissance.

La thèse a été proposée au sein du CEA-Liten dans le Laboratoire Matériaux (LM). Je remercie Sebastien Patoux et Didier Bloch pour leur accueil et la confiance qu'ils m'ont accordée. Cette thèse s'est également déroulée au sein de l'ESRF sur la ligne ID15a et je remercie donc Veijo Honkimäki pour son accueil.

Je témoigne ma gratitude aux membres du jury qui ont jugé ce travail. Merci à chacun d'entre vous, pour l'intérêt porté à ce travail ainsi que pour la qualité de la discussion menée et les interrogations soulevées.

Des remerciements les plus sincères pour mes deux encadrants de thèse. Ce fût une réelle chance de travailler avec vous. Vous avez été bienveillants pendant tout le déroulement de la thèse. Toujours de très bon conseil, vous avez su me laisser l'autonomie nécessaire pour mener à bien mes initiatives tout en m'aiguillant vers les bons chemins à suivre. Cette thèse a permis de me développer personnellement et scientifiquement et ceci vous est dû en grande partie.

Céline, que dire si ce n'est un énorme MERCI. Depuis le jour où tu m'as présenté la thèse jusqu'à la soutenance, tu as toujours été présente. Merci pour ta disponibilité, ton écoute, ta bonne humeur, tes conseils judicieux et ta grande implication dans la thèse. Je pense que notre travail minutieux et rigoureux a conduit au bon déroulement de ce travail.

Gavin, également un énorme merci. Tu as toujours été là pour m'expliquer, me montrer et me former aux techniques de caractérisations poussées et à l'analyse de données liées à l'utilisation du synchrotron. Tu as su me laisser l'autonomie nécessaire pour mener à bien mes propres expériences tout en me conseillant avec ton expertise de ces grands instruments.

Je remercie également Fannie Alloin, directrice de thèse, pour son dévouement, son implication et le temps alloué à la thèse. Ton expertise scientifique, ton expérience de la recherche et ton intérêt pour la thèse m'ont permis de pendre un réel plaisir à mener à bien ce sujet. Tu as toujours été très disponible et de bonne humeur. Ceci a rendu les échanges et les réunions très agréables avec une excellente ambiance de travail.

Merci également à Renaud Bouchet pour avoir suivi et participé à la thèse. Tes contributions scientifiques ont été d'une très grande richesse. Une grande partie du développement de la cellule électrochimique te revient ainsi que beaucoup d'explications et d'hypothèses sur les phénomènes/processus régissant le système. Je n'oublierais jamais tous ces « crobars » dessinés ☺.

Merci également aux laboratoires LM et L2PC pour leur bonne humeur et leur accueil chaleureux ayant conduit à 3 ans de thèse passés dans les meilleures conditions. Les conseils avisés en électrochimie, en impédance, en manip et dans bien d'autres domaines, ont permis d'avancer aux mieux, entouré d'experts toujours prêts à rendre service. Je remercie tout particulièrement Lionel Blanc pour la réalisation des cellules ainsi que Benoit Chavillon pour

ses soudures de haute volée ☺ et tous ceux qui ont participé aux manips à l'ESRF. Sans ces valeureuses personnes, ayant pris sur leur temps extra-travail, ces expériences n'auraient pas pu être possibles et votre aide a été très précieuse. Merci également aux personnes du LEPMI et de l'ESRF qui ont apporté leur expertise spécifique. Merci à Bernard Ferrari et Vincent Martin pour la réalisation des pistons et des tubes en verre pour la cellule électrochimique ainsi qu'à Marco Di Michiel pour les nombreuses explications concernant la tomographie.

Merci également à tous mes amis, rendant mon quotidien des plus agréables, notamment grâce à la « Dream Team CEA ». Les sorties en montagne, au bar, les BBQ, les escapes games, la course à pied, les soirées jeux et bien d'autres sont tant de bons souvenirs passés ensemble. Je vais surement en oublier certain mais ils savent que je pense à eux ☺. Pour éviter d'écrire un roman, je vais tous vous remercier de la plus simple des manières. Merci à: GLe, Juju, Alice, Virginie, Lauréline, Matthieu, Lucie, Xavier, Laurent, Natacha(tte), Ogi, PKz, Claire, BMG, Dadou, Laz, Thomas, Alex, Annaig, Remi, Eric, JBDs, Raphaphou, Vincent, Eddy, Léo, DBBn, Nico, Maxime, Djamel, Carolina, Caroles(s), Tim.

Je remercie également ma famille qui m'a toujours soutenu et poussé dans mes choix. J'ai ainsi pu mener mes études dans les meilleures conditions pour finalement aboutir à cette thèse marquant la fin d'un cycle de formation riche en émotions et en rencontres.

Et enfin, « the last but not the least » merci à Gaëlle pour ta présence au quotidien et ton soutien sans faille !

Table of content

General introduction

The CO_2 emissions in the atmosphere have reached record in the last few years (Figure 1). With more than one million kilogram emitted each second in the atmosphere, the concentration rate has reached record with 403 ppm in 2016[1].

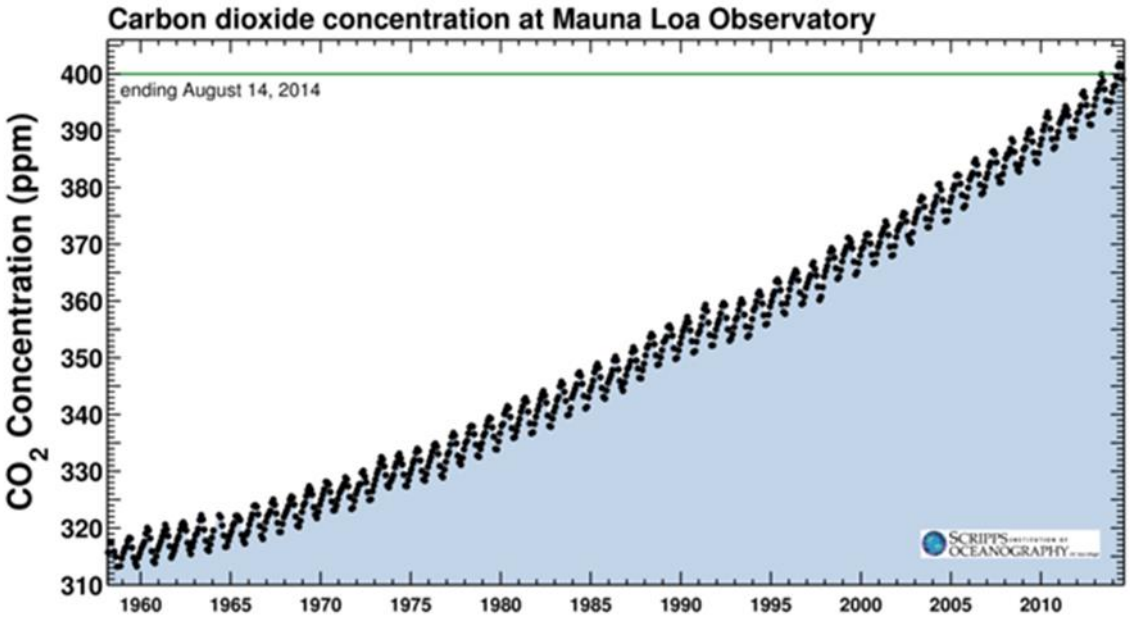

Figure 1[1]: Carbon dioxide concentration evolution in the atmosphere (taken at Manua Loa, Hawai, Etats-Unis).

Nevertheless, the CO_2 emissions have reached a plateau in 2016, with three consecutive years of stagnation. First, this is due to the reduced use of coal, in particular in China. However, developing countries such as India produce more and more greenhouse gas, as shown in the representation of CO_2 concentration in the atmosphere per country (Figure 2).

Figure 2[1]: CO_2 concentration in the atmosphere per country (2012 figures).

Intergovernmental panel on climate change (IPCC / GEIC) works about predicting the next few years' scenarios. According to their actual research, and as the worst scenario, the global warming at the earth surface could achieve 5°C in 2100[2] if the world continues to deal with fossil fuels, as seen in the Figure 3.

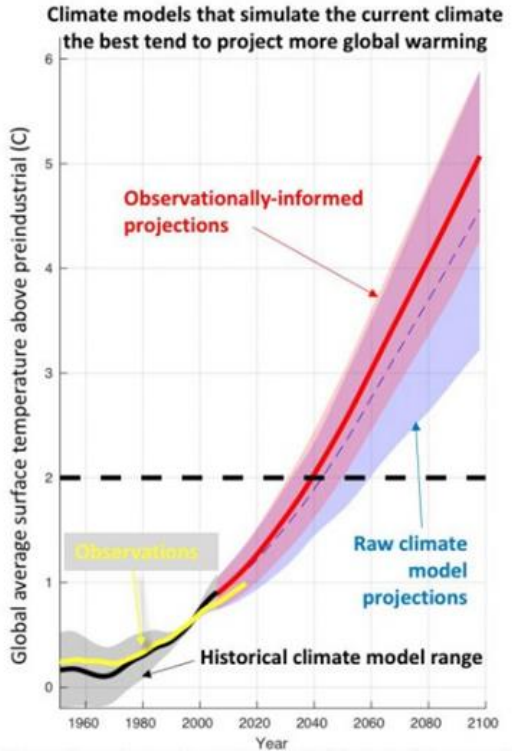

Figure 3[2]: Comparison between different simulation models about climate change.

Such temperature increase will have dramatic consequences on Earth. It could lead to an elevation of the sea level and thus in an irreversible manner : littoral erosion, vulnerability of storm, glacier melting , increase of the ocean level, modification of migration and possible flooding of coastal areas[3]. The ozone layer could also be impacted with higher UV transmitted to the population, reaching a maximum value in the Artic area. The biodiversity will also be impacted with the migration of thousands of species.

Fortunately, this grim report could be balanced. Always thanks to the IPCC research, the development of alternative energies, that is to say green and sustainable energies, could counterbalance the scenarios and limit their consequences. By reducing the emission of 80% to 95% of greenhouse gas until 2050 (compared to those emitted in 1990), the global warming will be limited to 1.5°C. To address this issue, actions must be done by developing relevant and powerful renewable energy systems. Still below nuclear power plants, fossil fuels and gas, the renewable energies are the fourth sources of energy production in France. Until 2030, the production of electricity must reach 32%[4]. However, these renewable energies, such as wind turbine or photovoltaic, are intermittent and must be coupled with energy storage. The battery system is one on the solutions being highly considered. Indeed, thanks to its polyvalence and application at different length scale, the energy storage by using batteries seems to be a suitable solution for future electric network.

Besides, the mass transportation has also a high impact factor on the worldwide pollution with ¼ of the CO_2 emits due to transport and ¾ of these CO_2 transport emission due to camion bus and cars[5]. That is why, the automobile industry is more and more concerned by developing hybrid electric vehicle (HEV) or electric vehicle (EV).

The fourth major popular batteries systems are lead acid (PB), nickel-metal hybrid (NiMH), nickel cadmium (Ni-Cd) and lithium-ion (Li-ion). Among battery systems, the lithium-ion (Li-ion) batteries are one of the most promising and have attract most of the attention since the 90's. This technology has been a real success in portable devices and seems to be the good compromise between cost, weight density and volumetric density to be implemented in EV[6] or HEV in a large scale. In that sense, gigafactories have been constructed in order to largely increase the volume production and therefore diminish the cost of the kWh to reach US$150/kWh until 2020[7].

However, despite the large success and development of Li-ion systems, these batteries seem to reach their performance limits[8]. That is why, other materials chemistries have been developed

in parallel thanks to high theoretical attractiveness in term of energy density and availability of materials[8]. One of the most promising, is the lithium/sulfur (Li/S) system[8] which is largely considered to replace the current lithium-ion system. The main reasons, for using such a technology, are the abundancy of sulfur material, its low cost, nontoxicity and its high specific capacity. It promises to double or triple the actual lithium-ion performance in term of weight density[9]. This technology has attracted high attention and has been largely characterized, but still issues remain preventing the industrialization and commercialization at a large scale[10,11]. The thesis is positioned in that sense to better understand the complex electrochemical mechanism and the limitation processes occurring while cycling, to further improve the viability of this system. A more detailed presentation of the Li-ion batteries and Li/S system is given in the chapter 1.

References

[1] www.planetoscope.com

[2] https://www.sciencesetavenir.fr/nature-environnement/climat/

[3] https://www.notre-planete.info/terre/climatologie_meteo/

[4] "Les enjeux pour la France," http://www.enr.fr/editorial/65/Les-enjeux-pour-la-France,

[5] Futura, "Transport et CO2 : quelle part des émissions ?," can be found under https://www.futura-sciences.com/planete/questions-reponses/pollution-transport-co2-part-emissions-1017/,

[6] T. Ioannis, Li-ion batteries for mobility and stationary storage applications, *JRC* **2018**.

[7] "Tesla Gigafactory | Tesla," https://www.tesla.com/gigafactory

[8] P. G. Bruce, S. A. Freunberger, L. J. Hardwick, J.-M. Tarascon, *Nature Materials* **2012**, *11*, 19.

[9] G. Li, Z. Chen, J. Lu, *Chem* **2018**, *4*, 3.

[10] T. Cleaver, P. Kovacik, M. Marinescu, T. Zhang, G. Offer, *J. Electrochem. Soc.* **2018**, *165*, A6029.

[11] R. Demir-Cakan, *Li-S Batteries: The Challenges, Chemistry, Materials and Future Perspectives*, **2017**.

Table of figures

Chapter 1: Literature review

1.1. Introduction to Li-ion batteries

Due to the high demand for portable storage, the development of new means energy storage system have been conceived to meet these needs. Rechargeable batteries are one of the most well adapted storage systems in term of energy density, cyclability, power and cost efficiency, required in the large field of portable devices. The lithium-ion (Li-ion) batteries have been considerably developed in the last few years, motivated by their high energy density, high cyclability and good specific power compared to lead-acid (Pb) or nickel batteries (Ni-Cd / Ni-MH), as shown the Figure 1.

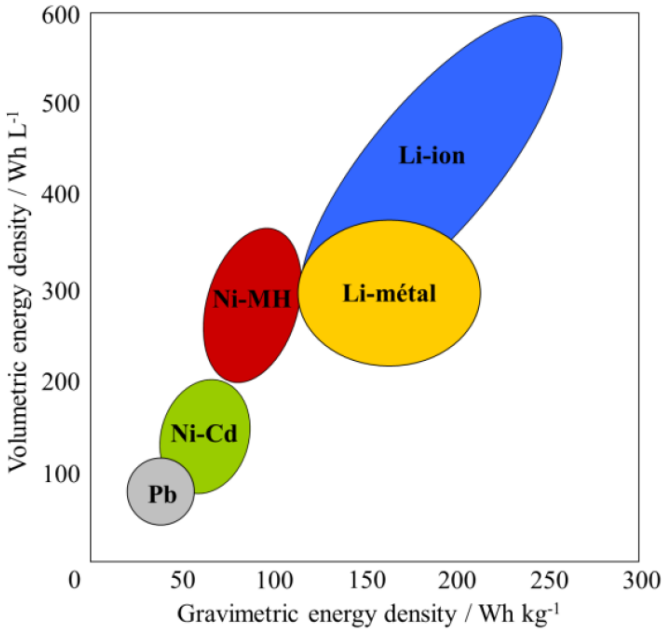

Figure 1: Comparison of different battery technologies in terms of volumetric and gravimetric energy densities[1].

The first work on lithium batteries started in 1912 by G.N Lewis, while it has not seen significant improvement since the 70s when the first lithium battery was commercialized[2]. For these first systems, lithium metal was used as the negative electrode but they suffered from safety problems and poor reversibility. In parallel, the first Li-ion battery was launched by Sony in 1991[3]. Despite lower practical energy density than lithium metal batteries, this technology was much safer and is dominant in the current battery market for portable devices. Classically, these batteries[4,5] are composed of a positive electrode and a negative electrode physically separated by a porous separator soaked in a liquid organic electrolyte. They rely on an

intercalation mechanism of lithium ions into the host structures of the cathode and anode materials[6]. Metal oxides such as $LiMn_2O_4$, $LiFePO_4$ or $LiNi_{1/3}Mn_{1/3}Co_{1/3}O_2$ are often employed in these systems as positive electrodes. The negative electrode is generally made up of graphite, which allows the intercalation and desintercalation of lithium ions during charge and discharge[5,7]. Separators act as a physical barrier between the two electrodes. They are generally soaked with a liquid electrolyte, composed of organic solvents and salts which allows the transport of lithium ions from one electrode to the other. During the discharge process, the lithium ion diffuses through the electrolyte from negative electrode to the positive one, in which it is intercalated. The electrochemical reactions induce an electron flux (from the positive electrode to the negative one) in an external circuit and thus the production of an electrical field. A reversible mechanism is observed during the charge; the lithium ion diffuses from the positive to the negative electrode. A schematic representation of the mechanism is shown in Figure 2.

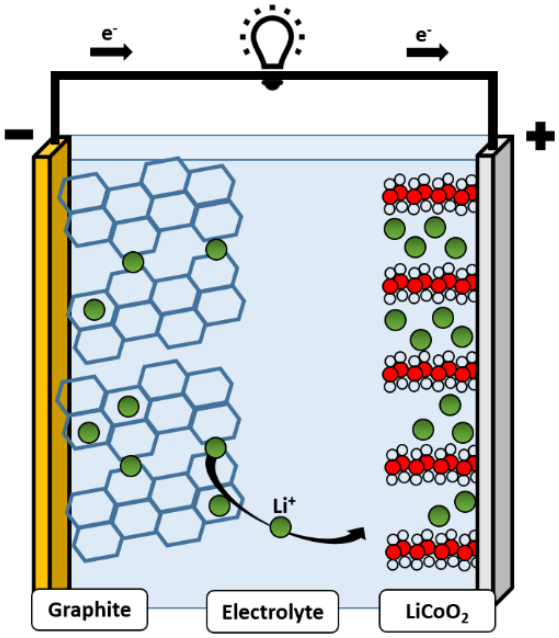

Figure 2: Schematic representation of a lithium-ion battery (discharge mechanism).

Meaningful improvements have been made in the last decade, during which the energy densities of Li-ion cells has been almost doubled from 150 $Wh.kg^{-1}$ to 240 $Wh.kg^{-1}$. A large volume of research has been done in order to increase repeatedly the battery capacity and power. However, even if Li-ion batteries are currently the most powerful technologies in terms of energy density, cyclability and specific power, this technology could not meet the high demand linked to energy storage, in particular due to the growing interest for renewable energy sources, stationary storage and electromobility. Therefore, batteries based on new chemistries must be developed

to meet the increasing demand for energy storage at competitive cost, taking into account the availability of raw materials as well as their toxicity and environmental footprint.

For that reason, different systems have emerged over the last twenty years, motivated by their attractiveness in terms of energy density. One of them is the lithium-sulfur (Li/S) system[8–10], with companies such as Sion Power[11] and OXIS Energy[12] planning to industrialize prototypes with very promising energy density in the near future (Energy density is in the range of 400-600 $Wh.kg^{-1}$ [13] compared to 240 $Wh.kg^{-1}$ for classical Li-ion system). This system has a complex electrochemical mechanism, different as current Li-ion systems, which is discussed in the next section.

1.2. Introduction to Li/S batteries

In the 60s, Herbert and Ulam[14] introduced sulfur as a positive electrode. Since this period, there have been considerable advances in sulfur metal technology but it is solely after 2008 that this technology has attracted the battery community. Indeed, this system is one of the most promising solutions to replace the current Li-ion technologies, for a large range of field such as military applications, stationary storage or space applications. Consequently, the number of publications in this field has considerably increased, as shown in Figure 3. The recent research conducted by TKM[15] shows that 2700 scientific articles (as of 2016) are linked to electrochemical system composed of sulfur, which corresponds to an increase of 5500% compared to 2009. The brevet portfolio is about 1400. All figures are summed up in Figure 3.

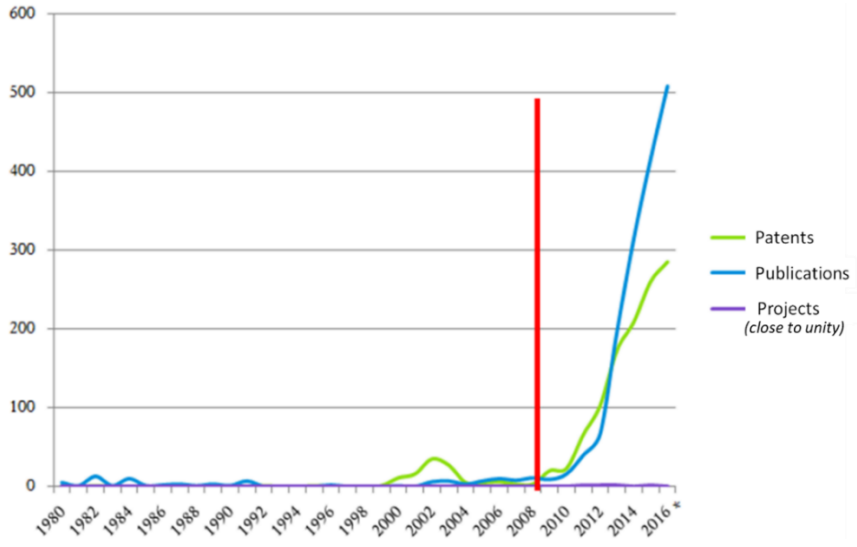

Figure 3[15]: Number of publications, patents & projects linked to the lithium/sulfur battery technology.

TKM shows also that in 2016, approximately 1900 papers are linked to lithium metal electrodes (increase of 700% compared to 2009) with a portfolio of 1500 patents. The sulfur is generally linked to the lithium metal electrode with 10% of papers dealing with both sulfur and lithium metal.

The use of lithium metal as a negative electrode has numerous advantages. Indeed, the lithium metal has a theoretical specific capacity of 3860 $mAh.g^{-1}$ and is the best negative electrode in term of energy density[16]. Moreover, it is a good candidate to be coupled with sulfur electrode due to its low electrochemical potential (-3.04 V *vs.* SHE).

Sulfur, with a theoretical capacity of 1675 $mAh.g^{-1}$ [17], is one of the higher specific density materials for positive electrodes. With respect to diminishing the battery costs, sulfur also appears to be a good candidate because it is an abundant material on Earth, cheap and non-toxic. The expected practical volumetric energy density could be approximately between 400 to 600 $Wh.kg^{-1}$, with proof-of-concepts done by Sion Power®[11] at 350 $Wh.kg^{-1}$ and more than 400 $Wh.kg^{-1}$ by Oxis Energy. With this system, it is thus possible to more than double the gravimetric energy density compared to current Li-ion systems[13]. The different technologies are compared in Figure 4 in term of gravimetric and volumetric energy densities.

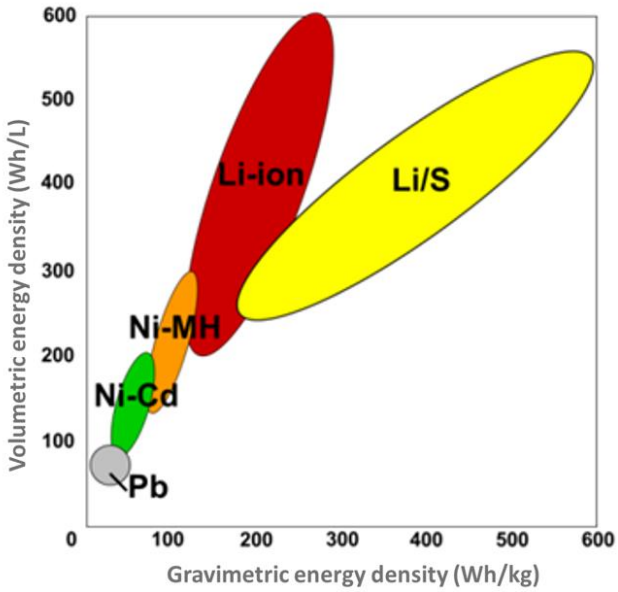

Figure 4[1]: Positioning of the Li/S system versus other rechargeable battery systems.

Even if theoretically this system shows numerous advantages, it has several technological challenges and constraints which must be addressed. The next section describes the functioning of the Li/S system and its limitations.

1.2.1. Working mechanism of Li/S system

The Li/S system is usually composed of a composite electrode based on sulfur and a negative electrode of lithium metal with a porous separator soaked with electrolyte.

A schematic representation of a "classical" Li/S system is shown in Figure 5.

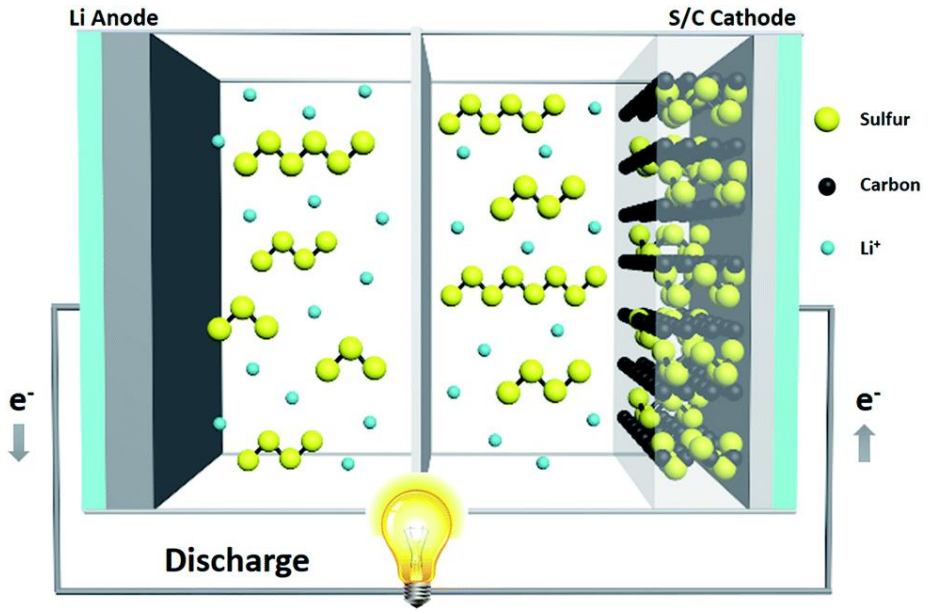

Figure 5[18]: Schematic representation of a "typical" Li/S battery.

The use of commercial elemental sulfur is possible. Nonetheless, it is necessary to add carbon additive(s) to have a sufficient electronic conductivity in the bulk of the electrode and counter balance the insulating nature of sulfur. In addition, a polymer binder is added to ensure a good cohesion between electrode components and adhesion to the current collector.

Elemental sulfur is in the orthorhombic alpha phase (α- S_8), stable at room temperature[19], existing as a cyclic molecule of 8 atoms of sulfur. The density is 2.07 $g.cm^{-3}$ and the molar mass is 32.066 $g.mol^{-1}$. Other allotropic forms of sulfur exist. In particular, sulfur can be found in the metastable phase (β-S_8), when produced electrochemically during the charge of the battery[20–22]. The lithium electrode is composed of metallic foil.

The initial state of the cell after assembly is charged.

Discharge mechanisms are based on electrochemical reactions between elemental sulfur and lithium metal to form lithium polysulfides. During the discharge, the lithium metal is oxidized at the negative electrode thus forming a lithium ion (Li^+) following the reaction:

$$16\ Li^0 \rightarrow 16\ Li^+ + 16e^-$$

At the positive electrode, sulfur is reduced through the following reaction:

$$S_8\ + 16e^- \rightarrow 8\ Li_2S$$

The total reaction occurring during the discharge is thus:

$$16\ Li + \ S_8 \rightarrow 8\ Li_2S$$

This reaction is produced at an average potential of 2.15 V vs Li^+/Li. The specific capacity obtained for one gram of sulfur is 1675 mAh in theory.

Mechanisms involved in this system are different[23,24] compared to the intercalation mechanism in the current lithium-ion systems[5,7]. Indeed, the Li/S cell relies on complex mechanisms, involving chemical equilibrium, *i.e.* disproportionation reactions, with the active materials changing their physical state while cycling. Sulfur initially exists as a cyclic and solid powder. While being reduced by lithium, it forms lithium polysulfides (Li_2S_x, $2 \leq x \leq 8$), which are soluble species, dissolved in the electrolyte. Along the first "quasi-plateau", at 2.4 V vs Li^+/Li, elemental sulfur is reduced to form long-chain polysulfides, i.e. composed of 6 to 8 atoms of sulfur (Li_2S_x, $6 \leq x \leq 8$). After this "quasi-plateau", all the active material has been dissolved in the electrolyte and the electrochemical reduction further proceeds in solution. Lithium polysulfides are gradually reduced to shorter chains (Li_2S_x, $2 \leq x \leq 4$) during the second plateau at 2.1 V, while final discharge products Li_2S_2 and Li_2S are formed and precipitate at the positive electrode[25]. A similar multistep process is observed during the recharge, with the re-formation of sulfur into the beta allotropic form[20,21].

A schematic representation of a typical electrochemical curve of a Li/S cell is shown Figure 6. This mechanism is a simplified and generalized one, and the next section discusses more precisely on the reactions occurring while cycling.

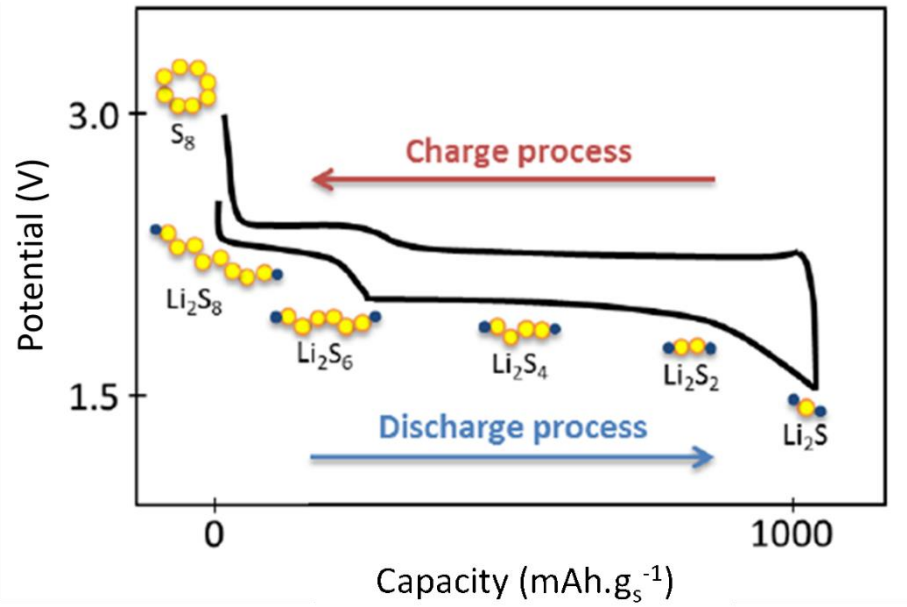

Figure 6 [1]: Typical voltage profile of a Li/S cell.

Despite the promise of this technology in terms of energy density, technological limitations have to be considered with attention, as discussed in the next section.

1.2.2. Limitations

The system limitations are diverse and concern not only the positive electrode, but also the negative electrode and the electrolyte. The most used keywords in the literature when discussing with Li/S limitations are, according to the study leads by TKM[15]:

Shuttle mechanism, capacity loss, complex electrochemical mechanisms, ageing of electrode and high loaded electrode. As a lot of work has been done on the system, solely the principal limitations, linked to the presented work, are detailed below and grouped in 3 categories.

- ***Positive electrode:***

Sulfur is an electronic insulating material ($\sigma = 5.10^{-30}$ S.cm^{-1} at RT [26]). That is why carbon additive(s) must be added to have sufficient kinetic reactions. The content of carbon in the mixture has to be optimized and can be very high, more than 50wt% in some studies[27,28]. However, the addition of carbon species reduces the volumetric and weight density of the system, as not participating to electrochemical reaction. Sulfur is also partially soluble in the organic electrolytes commonly used in Li/S batteries, leading to possible self-discharge[29,30]

when the system is stored in the charge state. The self-discharge is depicted in Figure 7[29] where it can be seen that the system storage time before cycling influences the obtained capacity in the first discharge.

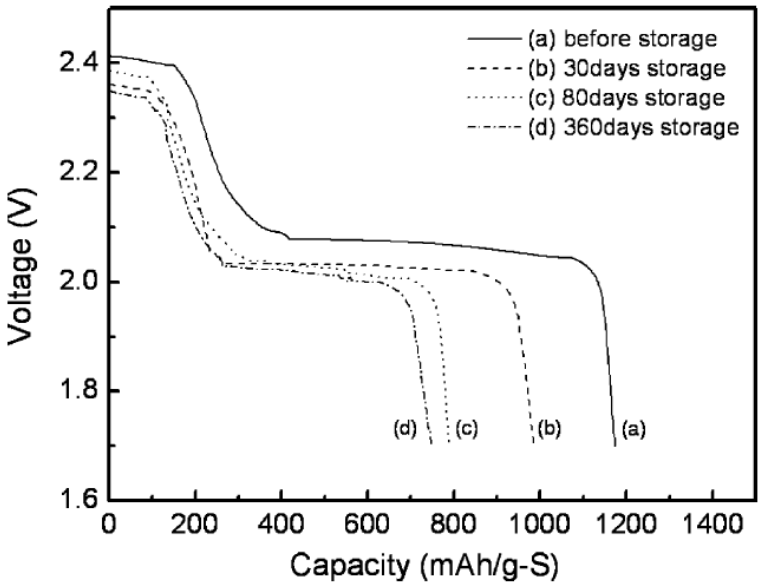

Figure 7[29]: First discharge curves of Li/TEGDME/S batteries as a function of storage times at 25°C: (a) initial, (b) 30 days, (c) 80 days, and (d) 360 days.

Generally, a quick capacity fade is observed after the first cycle with a stabilization of the capacity after about 10 cycles. The capacity loss is generally observed and associated with morphological changes[31–33], active species diffusion[34], reactivity at the negative electrode[34,35] and loss of electric contacts occurring in the system[31], especially in the first discharge but also in prolonged cycling. Indeed, the active materials change from a solid to a soluble state, creating drastic morphological changes in the electrode. When the sulfur (up to 80%wt) is reduced, porosity is created in the electrode that affects the mechanical properties which could lead to a loss of mechanical integrity.

In addition, during the discharge, Li_2S discharge products, precipitate, but with a different density compared to initial sulfur, with respectively 1.66 $g.cm^{-3}$ and 2.07$g.cm^{-3}$ for Li_2S and S_8[36] . This volume variation while cycling can lead to volume expansion of the electrode during the discharge and finally damage the electrode structure[37,38]. While cycling, these phenomenon of active material dissolution/precipitation can lead to electrode collapsing and possible loss of electronic connection between some electrode areas and the current collector, resulting in a loss

of electro-active surface and polarization. These changes, taking place from the first cycle, are responsible of the high capacity fade usually observed in the initial cycles [32,33].

As said before, Li_2S discharge products, precipitate on the active surface of the positive electrode and, due to its isolating electronic property, forms a thin isolating layer on the carbon particles which can limit the conversion reaction by blocking the active surface.

- ***Negative electrode:***

The negative electrode is generally composed of a lithium metal foil and presents numerous technological challenges. In commonly used liquid organic electrolyte, lithium plating is usually inhomogeneous while cycling, with possible formation of foam and/or dendrites[39–41]. The dendrites (Figure 8) formed could puncture the separator and lead to short-circuits between the two electrodes and other safety issues[42]. This phenomenon is even more important at the high current densities required for fast charge.

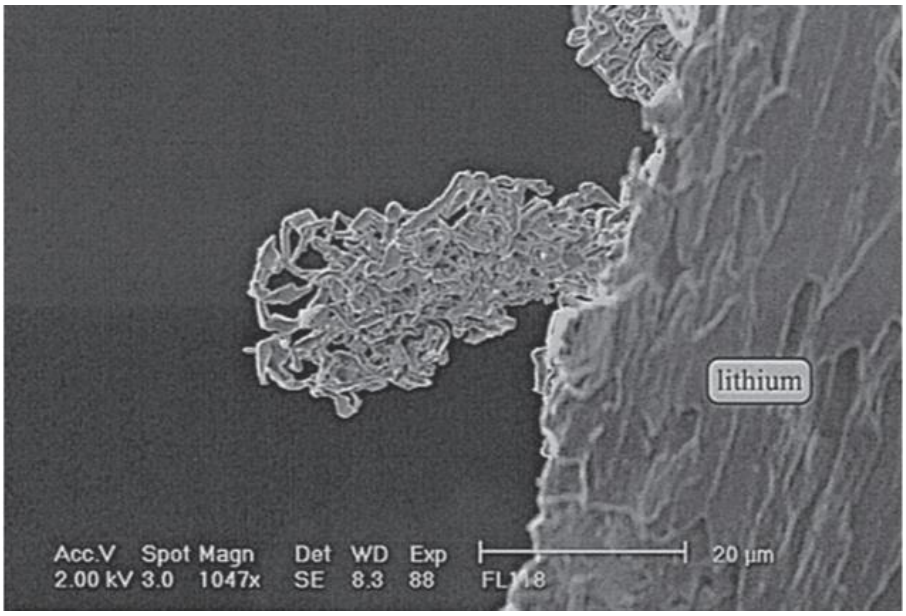

Figure 8[43]: Dendrite formed in a lithium battery after one charge at 2.2 mA/cm².

Moreover, lithium metal is highly reactive facing the electrolyte used[44]. It creates a passivation layer (Solid Electrolyte Interphase: SEI) at the electrode surface, composed of lithium and electrolyte degradation products[45–47]. This layer creates an additive resistance in the system, which increases the cell polarization and can limit the performance at high cycling rates, *i.e.* current densities. Moreover, the SEI is usually not mechanically stable enough to accommodate lithium metal volume changes, and cracks can appear in the SEI layer. Fresh and highly reactive

lithium metal, obtained both by heterogeneous lithium deposition and SEI crack formation, is thus in contact with the electrolyte and continuous SEI formation is observed, which progressively consuming both lithium and electrolyte. As a consequence, lithium and/or electrolyte depletion can occur. The SEI formation is in turn responsible for poor cyclability of the lithium metal cells. This is even more important when the lithium foil is transformed to a lithium mossy, which becomes progressively electrochemically inert during cycling[48].

All these characteristics limit drastically the electrochemical performance, lifetime, security and cyclability of the cells.

In particular, in a Li/S system, the use of highly loaded sulfur electrodes requires high current densities at the lithium metal negative electrode, as well as significant depth of charge/discharge for the lithium layer. With 10 $mAh.cm^{-2}$[49], the thickness variation of the lithium electrode is about 50 µm. As said before, this high volume variation could cause two phenomena:

(1) : The electrolyte depletion in contact with the "fresh" lithium.
(2) : Dendrite formation due to heterogeneous lithium surfaces.

- ***Electrolyte:***

The organic electrolyte plays also an important role in the system. While discharging the cell, the reduction of sulfur forms soluble polysulfides in the electrolyte. The electrolyte viscosity is thus changed, which affects the ion transport and the internal cell resistance[50–52].

Moreover, a "shuttle mechanism" occurs between the two electrodes while charging, which limits performance during the charge. Indeed, during the discharge, the long-chain polysulfides migrate to the negative electrode and are reduced on the lithium surface to shorter-chain polysulfides which migrate to the positive electrode and are oxidized and so on. This transport is essentially due to gradient concentrations of theses chains in the electrolyte. It is generally accompanied by potential plateau at 2.45 V vs Li^+/Li during the charge and largely limits the coulombic efficiency of the system[53].

1.3. System improvements

Much works has been done with the purpose of improving the system. As the system is very complex, strategies of improving all the cell parts are necessary. That is why the positive electrode, the negative electrode and the electrolyte must all be improved. Numerous publications exist dealing with such system improvements. Here, the focus is on the state of the art related to the work done in this thesis.

1.3.1. Electrolyte

The electrolyte choice is a key parameter in the Li/S system. Indeed, this electrochemical system could be considered as a semi-liquid due to the fact that the active material is solubilized while cycling and so soluble species are involved in the overall electrochemical reactions. The use of carbonate electrolyte (such as dimethyl carbonate, propylene carbonate or ethylene carbonate), generally used in Li-ion system[54], is not possible in the Li/S system due to the high reactivity between polysulfides and the carbonate based electrolytes[50].

Thus ether based solvents, with properties (donor number, dielectric constant and viscosity) allowing high dissociation and mobility of polysulfides without detrimental reactivity versus the lithium metal electrode, are chosen.

Most of the commonly used electrolyte are based on 1,3 dioxolane (DIOX) with tetraethylene glycol dimethyl ether (TEGDME)[55,56] or 1,3 dioxolane with 1,2 dimethoxyethane (DME)[57,58]. A majority of studies have been carried out with these two ether mixtures but the use of polyethylene glycol dimethyether (PEGDME) or diethylene glycol dimethylether (DEGDME)has also been reported[23,51].

Other organic solvents such as sulfolane[59], tetrahydrofuran (THF)[60] or dimethylformamide (DMF)[61] have also been investigated by other groups. They allow tuning of polysulfide equilibria in solution and the electrochemical processes involved during cycling, with in return higher viscosity or lower boiling point.

The most common used lithium salt is the lithium bis(trifluoromethanesulfonyl)imide (LiTFSI) due to its high ionic conductivity, good thermal and chemical stabilities. The active potentials for the Li/S system, between 1.5 and 3.0 V vs Li^+/Li , avoid the aluminum corrosion[50,62] which is the drawback associated with the use of LiTFSI in classical Li-ion battery.

Different additives have been tested such as the lithium nitrate $LiNO_3$, firstly used by Aurbach *et al.*[63] . The use of $LiNO_3$ allows the formation of a stable SEI at the lithium metal electrode surface and limits the shuttle mechanism and so improves the coulombic efficiency[64]. Nonetheless, below 1.6 V vs Li^+/Li, $LiNO_3$ is reduced at the surface of the positive electrode and is detrimental to prolonged cycling.

1.3.2. Positive electrode

Much works has been done to control the polysulfide diffusion, enhancing the low electronic conductivity of Li_2S and sulfur and limiting the self-discharge. The architecture of the composite electrode has also been extensively investigated. One strategy, is to confine the active materials, *i.e.* the sulfur species, in the carbon structure. This could limit the polysulfide diffusion in solution[65].

Ji *et al*. [66], with the use of mesoporous carbons, have reported a simple carbon structure with a high electronic percolation and good affinity between carbon and active sulfur materials. Porous carbon networks have been intensively studied, including microporous carbons (pore size below 2 nm) to confine the active materials and increase the electronic percolation[27,67] and mesoporous carbons[68,69] (pores size above 50 nm) acting as a polysulfide adsorbing agent, limiting their diffusion in the electrolyte. Finally, it is possible to obtain the advantages from each carbon structure in term of confinement, electronic & ionic percolation and specific capacity improvement.

Other structures with carbon nanotubes have already been tested such as carbon-nanotube (CNT)[70,71] or carbon-multiwall-nanotubes (CMWNT)[72]. The aim of such architectures is to accommodate the volumetric expansion while discharging the cell by keeping a good reversibility. These structures allow also a good absorption of polysulfides thanks to the high surface of carbon. More complex structures and architectures were used, notably the graphene structure with its high adsorption ability towards lithium polysulfides[38,73]. In this way, a number of 3D structure even more ingenious has been studied and developed such as reported in Figure 9[74].

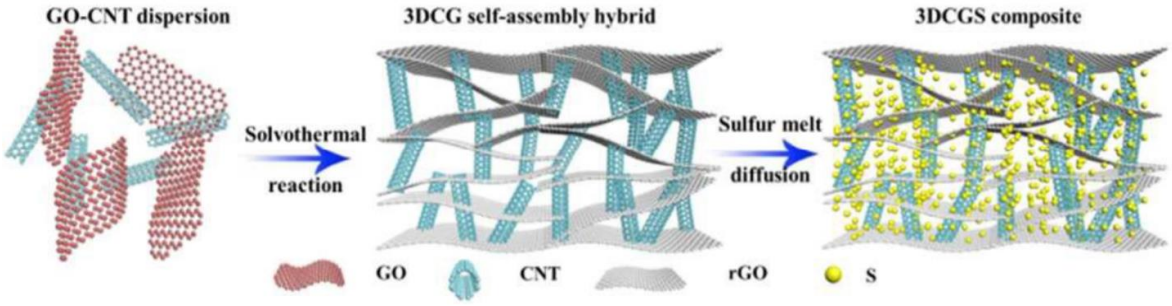

Figure 9[74]: Synthesis procedure of the 3DCGS composite.

This bi-structure allows to benefit from the presence of highly conductive 1D graphene oxide carbon nanotube (GO-CNT) and from the bimodal mesoporous structure, providing electrochemical reactors and facilitating the electrolyte diffusion into the cathode structure.

However, these high added values carbon structures seem unlikely candidates to be industrialized at large scale due to the high complexity and cost. Thus, always with the aim of searching for higher performance, the use of a 3D commercial "simple" carbon network, for instance the use of a current collector based on carbon fibers, seems to be a good solution in order to have sufficient capacity with a simple cathode preparation process. Indeed, Walus *et al.* [75,76], using a commercial non-woven carbon paper (NwC) (Figure 10), composed of micron sized carbon fibers, have shown that the use of this carbon support is a good solution to have highly loaded sulfur electrodes with good specific capacity.

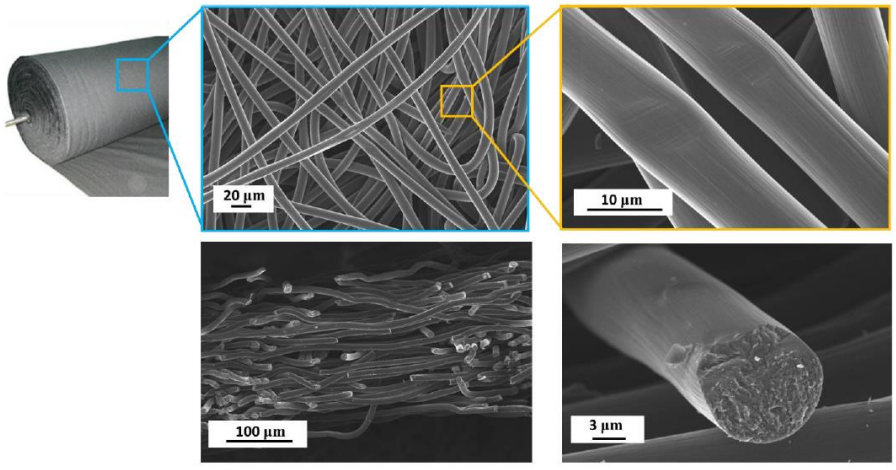

Figure 10[1] : SEM photos of GDL felt (non-woven carbon tissues, NwC), a commercial product of Freudenberg® (H2315).

Indeed, with a similar loading as used with an aluminum current collector, the obtained capacity with the NwC is larger (Figure 11) even considering the complete electrode mass (carbon felt is usually much heavier than aluminum foil). This is due to the conductive network formed by the 3D carbon matrix leading to stable ionic and electronic pathways. Moreover, this current collector is also used as an electrolyte reservoir, which improves the polysulfide solubility. This type of current collector was also used in this thesis and because it is relatively cheap while the cathode preparation process is quite simple.

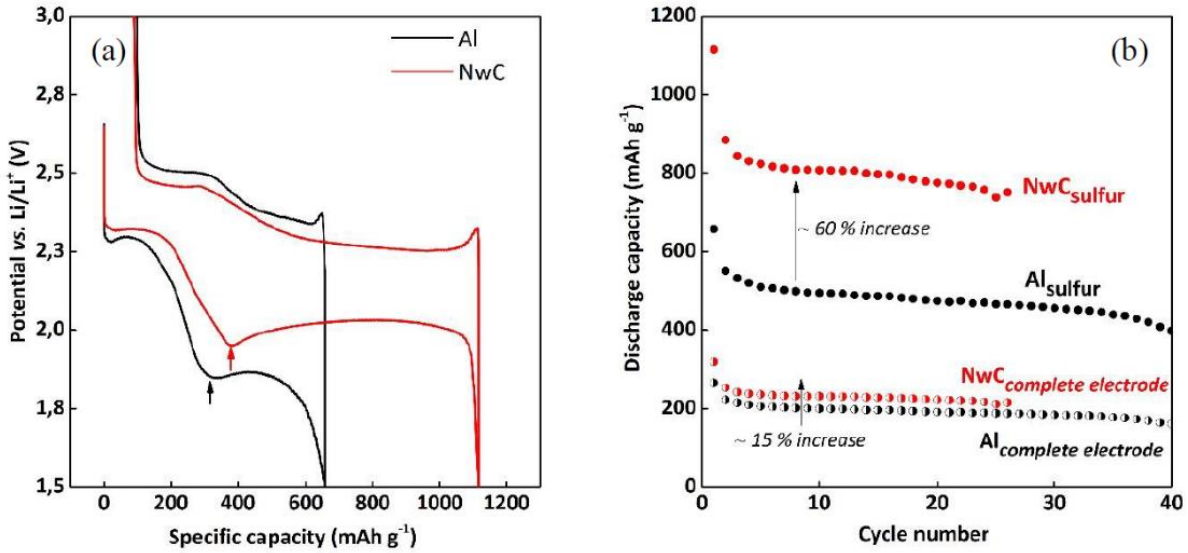

Figure 11[1]: (a) Galvanostatic curves from same sulfur electrode (i.e. same loading) with aluminum and NwC as current collector (b)Capacity retention with coulombic efficiency.

1.3.3. Negative electrode

As already mentioned, the negative electrode, used in the Li/S system, is composed of a lithium metal foil. Several issues have been identified using such an electrode, such as safety problems linked with possible dendrite formation while cycling, low cyclability[77], high reactivity with polysulfide and the formation of mossy foam[78] while charging the cell.

One of the main goals of many studies is to suppress, or more feasibly, reduces the nucleation and growth of dendrites. The use of polymer electrolytes, solid electrolytes or lithium electrode coating have been reported as possible solutions to limit the dendrite growth[79].

Another solution is to improve the mechanical pressure[39]. Indeed, the mechanical pressure could have an important impact of the lithium deposition morphology, the dendrites formation and the cyclability[80]. Gireaud *et al.*[81] have shown that increasing mechanical pressure on an

electrode stack could improve the lithium cycling efficiency (Figure 12) . Indeed, enhanced pressure leads to lower electrolyte consumption and better compactness of lithium deposition.

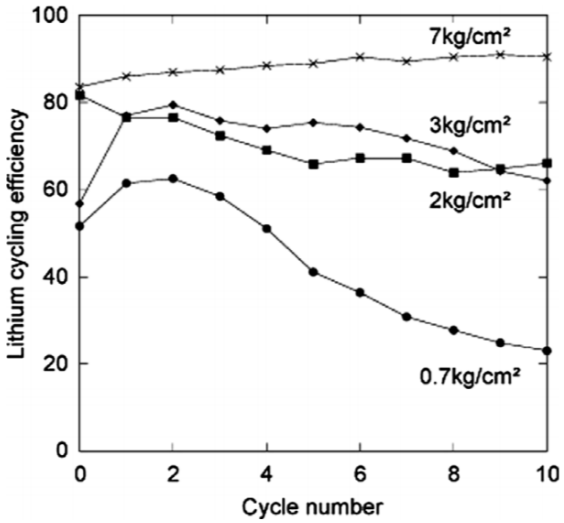

Figure 12[81] :Influence of internal pressure on lithium cycling efficiency in EC/DMC-LiPF$_6$.

Finally, tests have been done to control the lithium deposition in favorable places[82]. Indeed, with micro/nano-architectures such as Si wafers and ZnO nanowires, it is possible to control the preferential deposition of Li in the micro/nano patterns. As seen in this work, a copper foil with micro-sized cylindrical pits seems to be the most preferable current collector to control the lithium deposition. It was confirmed by Zhang *et al.*[83], who succeeded in depositing a uniform and stable lithium metal layer by producing a uniform lithium ion distribution at the electrode surface.

Another improvement is to protect the lithium layer by adding $LiNO_3$[84]. Indeed, $LiNO_3$ is reduced while cycling and forms, at the lithium surface electrode, a stable passivation layer (SEI). It could also limit notably the shuttle mechanism.

Several groups demonstrate that modifying the separator could also limit and suppress the shuttle mechanism[85–87].

All these solutions have more or less success in solving the lithium metal issues, but have generally not been implemented or tested in the Li/S system. In addition, few groups only have considered and characterized both the sulfur and the lithium electrode at the same time. Characterizing such a complex system requires powerful tools to probe the whole system under *operando* conditions. The next section deals with Li/S characterization.

1.4. Li/S batteries characterizations

1.4.1. From *ex-situ* to *operando* characterizations

Understanding the processes governing the functioning of the battery and the limitations is thus crucial to improve the viability and the system performances. As mentioned in the previous section, the Li/S system improvements require powerful characterization tools to understand the benefits of each development strategy. For that reason, numerous characterization techniques have been used in order to better understand the complex Li/S electrochemical system[88].

The active species in the system are of different natures and have different properties. In addition, the active materials exist as both solid and soluble forms, and thus require complementary and well adapted characterization tools to probe the whole system. There exist a large number of characterization techniques allowing to probe the system. Considering only a few of these techniques, it is possible to characterize the polysulfides by UV-Vis[58,89,90], Raman spectroscopy[91], X-ray absorption spectroscopy[24] or high-performance liquid chromatography[23] (HPLC). In addition, concerning the solid product, scanning electrode microscopy (SEM), X-ray diffraction (XRD)[20,25,92–96] or absorption tomography are useful techniques.

The investigation of morphological changes in Li/S cells is essential to understand the degradation phenomena occurring while cycling. However, most studies have been carried out *ex-situ* or non-*operando*. To better understand the functioning of the Li/S system, *operando* tools have been developed to probe it under working and environmental conditions[88,97] in the recent years. It is thus possible to follow the evolution of the cell components in their environment. These analyzes are generally performed at synchrotron radiation in order to have sufficient energy to pass through the sample, sufficient temporal resolution and a short acquisition time.

As mentioned above, multiscale *operando* tools allow a more complete characterization of the system. To that end, this thesis is focused on two complementary techniques (X-ray diffraction and absorption tomography) which have already been coupled to characterize materials at multiple length scales[98–100]. The next section details the state of the art for both techniques.

1.4.2. X-Ray diffraction (XRD)

The X-ray diffraction technique is a non-destructive tool that provides information about the crystallography, physical properties and chemical composition. The XRD allows to measure the average spacing between layers or rows of atoms; the orientation of a single crystal or grains; determination of unit cell dimensions; measurement of sample purity or find the crystal structure of unknown material or measure size, shape of crystalline regions. The pattern obtained consist on an intensity vs. angle diffraction. It is thus possible to deal with peaks position, width and intensity. The phase identification is one of the most important uses of XRD. After obtaining the XRD patterns, it is possible to calculate the integrated intensities and then compare to the known standards. It is then possible to identify an unknown material by comparing the XRD pattern with a standard one.

In addition, the use of synchrotron light source allows to have a XRD beam with higher brightness than those obtained from normal X-ray tube. In addition, it allows to provide image of the structure of the materials with wavelength tunable to have the right energy to probe the right materials. It is then possible to have fast data recording.

X-ray diffraction has been shown to be an excellent *in-situ* tool to probe the electrode structural characteristics as shown by Morcrette *et al.*[101] in the lithium desintercalation in $LiCoO_2$ electrodes.

1.4.2.1. Application to the Li/S system

X-ray diffraction has been applied in the Li/S system by many groups to probe the formation and consumption of crystalline species while cycling[20,92,93,101].

Following the different XRD studies, questions about the exact discharge mechanism have been raised. Indeed, *ex-situ* experimental results have led to the formation of various hypotheses and the literature is divided concerning different points such as the moment of appearance of different phases, such as the formation/disappearance of Li_2S or the possible formation of solid Li_2S_2. Most of these studies were done *ex-situ*. More recently, Cañas *et al.*[96] & Nelson *et al.*[95] applied *in-situ* and *operando* XRD studies to the Li/S system. However, the results obtained differ. Even if both found a complete disappearance followed by recrystallization of sulfur, it opinions differ about the Li_2S product. Nelson *et al.* found no evidence of crystalline Li_2S species whereas Cañas *et al.* reported Li_2S formation from 60%DOD and a total consumption during the next charge. In any cases, the electrochemical processes occurring are greatly

dependent on the cell composition, such as the electrode architecture[27], the electrolyte/sulfur ratio[102] and the electrolyte solvents[58].

More recently, Walus *et al.*[20] have proposed a complete mechanism of Li_2S formation and oxidation (Figure 13), with a two-step production and consumption of Li_2S and the involvement of Li_2S_2 discharge product[25].

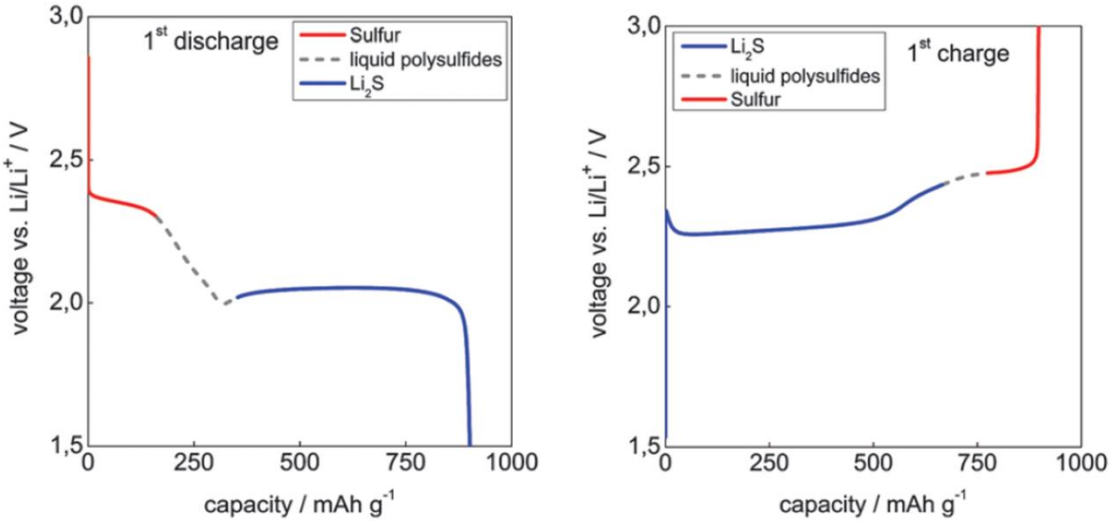

Figure 13[20]: Electrochemical discharge and charge profiles, with moments of appearance/disappearance of active materials while cycling.

Even if the time of appearance is often difficult to identify precisely[103], the recent experiments seem to converge [20,25,75,92,104] about the moments of sulfur and Li_2S appearances. Li_2S appears at the beginning of the second plateau and both Li_2S and Li_2S_2 are formed competitively with different proportions during the second plateau.

All these studies have demonstrated the high potential of using such a technique to understand the mechanism of formation of crystalline species in the system. However, as mentioned above, the development of new 3D electrode architectures, aimed at improving sulfur electrode performance, requires the use of 3D characterization techniques.

1.4.2.2. X-Ray Diffraction Computed Tomography (XRDCT)

The need for spatial resolution is thus compulsory to better understand the mechanism in the composite electrode. X-ray Diffraction Computed Tomography (XRDCT) is one of the techniques allowing 3D spatial resolution[105]. Bleuet *et al.* have showed a schematic representation of the 2D diffraction pattern obtained (see Figure 14[106]).

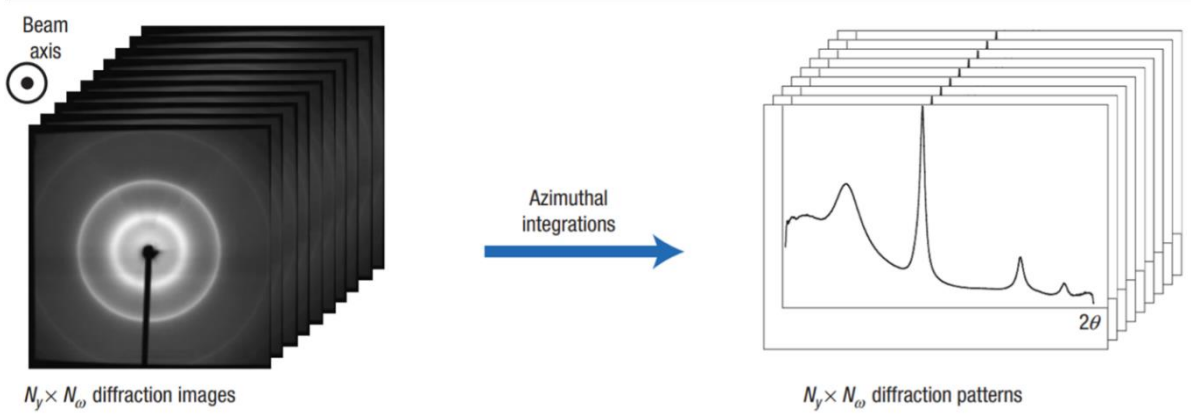

Figure 14: For every position (y, ω), the 2D scattering pattern is integrated over the azimuthal angle and produces the respective 1D scattering pattern.

This representation shows that each N_Y*N_w diffraction images could be integrated to have N_Y*N_w diffraction patterns. These projections can then be used to make, point by point, a tomographic reconstruction of the 3 dimensional object via filtered back projection, in the same manner as more classical absorption tomography discussed below. It is therefore possible to obtain XRD pattern from each voxel defined by the size beam.

The use of XRDCT has just begun to be applied in the battery field[107–109]. It was used by Jensen *et al.*[107] to monitor Li-ion batteries and Ni-MH batteries in order to have high structural and textural details and notably demonstrated the inhomogeneity while cycling. There is no previous work using XRDCT to study the Li/S system. Furthermore, as demonstrated by Bleuet *et al.*[106] & Pietsch *et al.*[110], the XRDCT technique can advantageously be coupled with absorption tomography techniques enabling a multimodal analysis to make a complete full 3D map of, for instance, an electrode.

1.5. Absorption tomography

1.5.1. Principle

This characterization technique, was first applied in 1971 in medical field[111]. Absorption tomography is not very frequently used in many industrial and research fields. This non-destructive technique enables to visualize the inside of the materials. Both dense and porous materials could be probed. It has been applied in many varied domains, notably in biology[98,112,113], medicine[114–116] or in building construction[117]. This analysis is based on the Beer-Lambert law, which states that an X-ray beam of intensity ("I_0") passing through a certain

matter thickness ("d") composed of materials with absorption coefficient ("μ") is reduced by a certain intensity:

$$I = I_0 e^{-\mu d}$$

This creates a contrast between the different materials in the path of the beam, resulting in a X-ray radiogram. A schematic representation of the experimental system is shown in Figure 15.

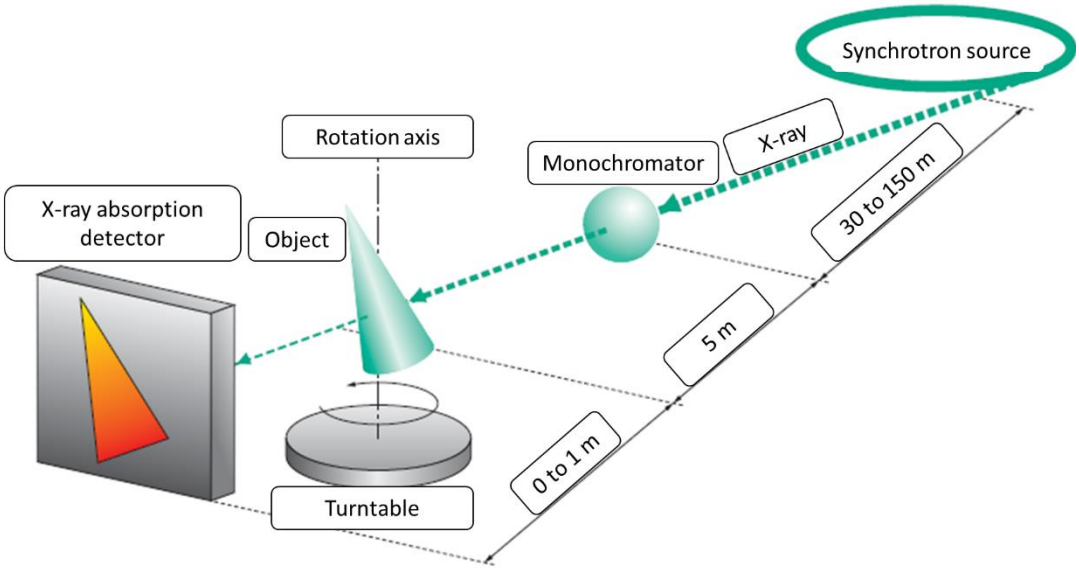

Figure 15[118]: Schematic representation of an experimental set-up of X-ray absorption tomography in a synchrotron .

It is thus possible to obtain qualitative and quantitative information of the materials used in a system and follow their evolution. From the 2D raw images (X-ray radiogram), a calculation method allows to reconstruct a volume, allowing to see the materials in the whole sample. Indeed, by using of an inverse-Radon transform, it is possible to transform the set of line integrals to reconstruct the distribution of local value of the absorption coefficient as function of the 3D space coordinates (x,y,z), in each point of the sample. The smallest volume analyzed is called a voxel, *i.e.* the extension of a pixel in 3D.

In order to obtain a sufficient legibility of the images, the intensity, measured by the detector, needs to be, at least, higher than 10% of the initial intensity. It raises a constraint about the thickness of material to be studied. For instance, concrete could be probed on several centimeters, whereas it is difficult to probe lead with this technique. Another constraint is the temporal resolution. Indeed, higher is the resolution chosen, longer will be the time to record

the data. It means that the temporal resolution must be suitable with phenomena occurring in the system and that spatial resolution must also be suitable with the "size" of materials probed.

This technique has been frequently applied in the battery field[110,119–125]. For instance, it is thus possible to know the state of charge (or discharge) of a cell in an electric vehicle by analyzing the structural parameter of the active materials[126].

In the Li/S system, weakly-absorbing materials are used such as lithium, carbon and sulfur. In pure X-ray absorption mode, it is difficult to separate the different phases due to their weak absorption and relatively similar attenuation coefficients. However, the use of X-ray phase contrast imaging allows tracking even weakly-absorbing or contrasting materials[127,128] and has been significantly developed in the last decades[129]. The use of the phase imaging has been developed thanks to improvement in synchrotron radiation sources, detectors and optical elements. The common use of the imaging contrast in synchrotron radiation is the propagation-based technique. A simple illustration of the phenomenon is seen in Figure 16.

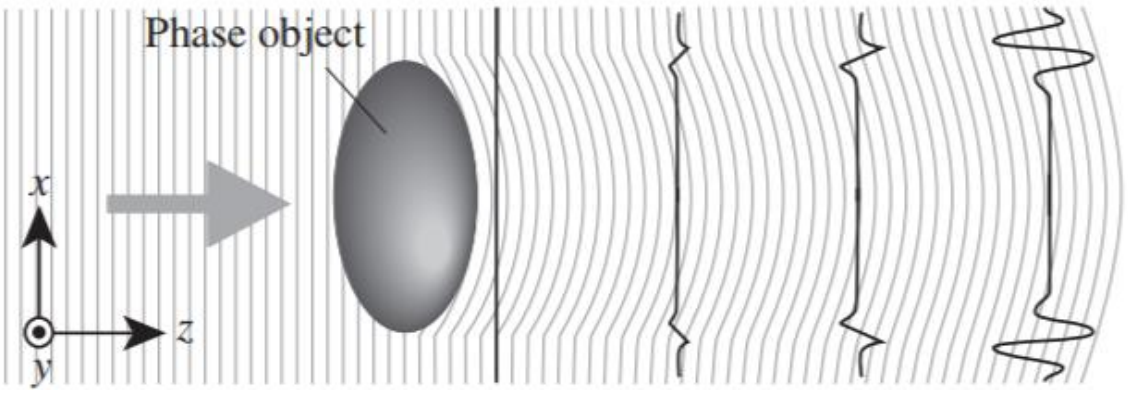

Figure 16: Explanation of the phase contrast imaging[130].

In this figure, an edge-contrast is observed at the border edge of the object. With the right distance between the object and the detector, this contrast is maximized and enables to have a supplementary contrast that the one obtained from pure X-ray absorption.

Fitzgerald *et al.*[131] show the difference between image taken from pure absorption and image taken from phase contrast (Figure 17).

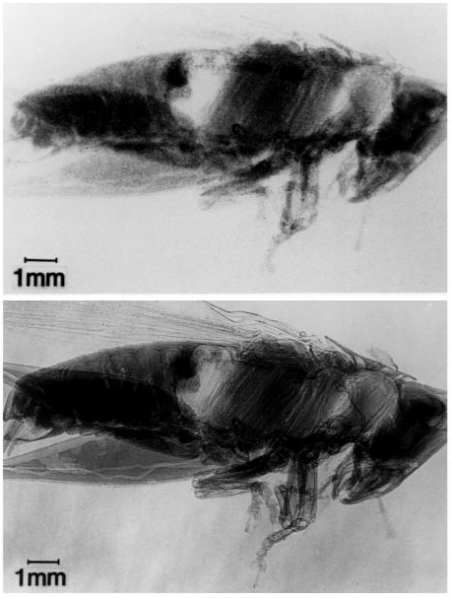

Figure 17: Pure absorption image (above) and phase contrast image (below) of a locust[131].

At the top, there is an image of a locust with a "conventional" radiograph and at the bottom, from the phase-contrast imaging using the information from the interference fringes. This allows an enhancement of the observed edges. This absorption and phase contrast techniques are nowadays frequently used in the synchrotron field and of particular interest for the Li/S battery system composed of similar and weakly absorbing materials.

1.5.2. Application to the Li/S system

With the structural and morphological changes occurring while cycling and the improvement of 3D positive electrode architectures, absorption tomography is more and more employed to probe the Li/S system. Zielke *et al.*[31] succeeded in analyzing the sulfur electrode and have reported the penetration depth of sulfur in the current collector thanks to *ex-situ* absorption tomography measurements. Indeed, they could differentiate the sulfur from the carbon binder domain (CBD) despite of the low absorption coefficient variation (Figure 18).

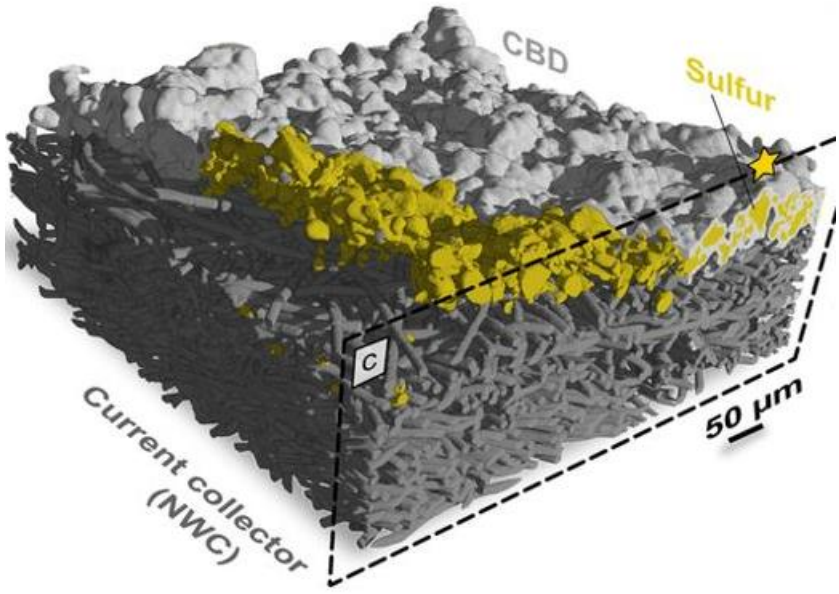

Figure 18[31]: 3D schematic representation of an uncycled sulfur electrode casted onto NwC current collector.

They also demonstrated large morphological changes in the first cycle in term of particles size, active material distribution and contact areas, in particular showing that sulfur redistributes inside the porous structure of the current collector upon cycling. The abrupt changes in the first cycle seems to converge to an equilibrium while cycling with respect to particle size, distributions, contact areas, discharge capacity and loading. It seemed pertinent to probe the first cycle with higher resolution in order to better understand the degradation phenomena. In addition, they stated that X-ray phase contrast tomography must be coupled with other characterization techniques in order to have a more complete understanding.

Risse *et al.*[99] have carried out *operando* radiography allowing them to follow the sulfur deposition onto a monolithic carbon support while cycling. They did not find evidence of Li_2S at the end of discharge but gained new insights into sulfur crystallization. Indeed, they reported the production of macroscopic sulfur crystals which quickly dissolve while discharging the cell.

Yermukhambetova *et al.*[132] proved that X-ray tomography is a powerful tool to probe the active materials while cycling and have shown that after the first cycle the sulfur mass loading seems to be reduced compared to initial state. This mass loading surprisingly increases while cycling, leading to the hypothesis of sulfur agglomeration. Indeed, there is a decrease of the average surface/volume ratio which is associated with an increase in sulfur particle agglomeration. However, this loss of surface area has a consequence on the connection between the carbon matrix and the sulfur, which finally decreases the active material utilization.

Understanding the mechanisms leading to lower electrochemical activity of active material is thus compulsory to improve capacity and cycle life. They suggested that nano-computed tomography would be very helpful to probe the system at the individual particle scale.

Yu *et al.*[92], investigated positive sulfur electrodes by both XRD and absorption tomography. They found complete agreement between the crystalline and morphological structures. In addition, they stated that the current density and the operation of the cell drive the size distribution of sulfur clusters. Indeed, higher current density would lead to a uniform distribution and growth of nuclei with smaller particle size.

For the lithium electrode:

Usually not characterized while probing the Li/S system, the lithium electrode attracts more and more attention with the development of high energy density and solid-state batteries. Tomography has already been used to probe the lithium layer. Indeed, the morphological change of the lithium electrode and the possible formation of dendrites have motivated researchers to characterize the electrode structure[133].

Similar to absorption tomography, Shi *et al.*[134] used FIB-SEM imaging to characterize in 3D a lithium metal foil and demonstrated the pitting phenomena occurring while cycling up to a certain critical value of current density. They also demonstrated that the grain boundaries could be the place of pitting initiation due to the fast atomic diffusion in this zone. In addition, they have stated that solvent molecules form most of the SEI in the grain boundaries and the SEI is the place where lithium ions diffuse quickly. They proposed a schematic representation of the lithium electrode under different stripping conditions in Figure 19.

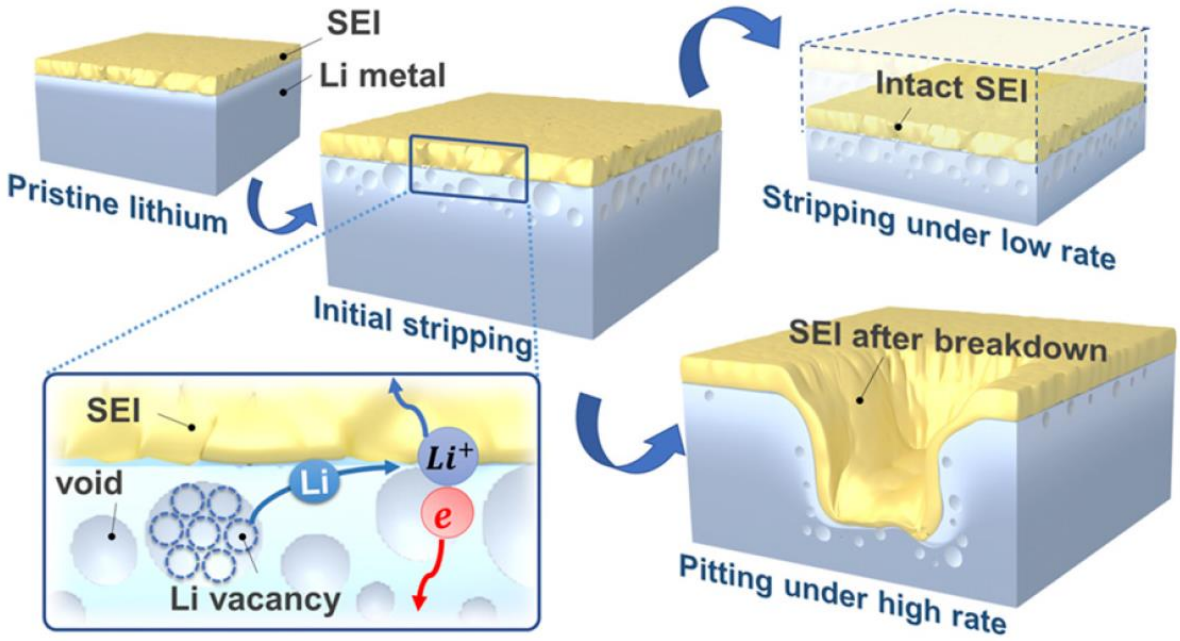

Figure 19 [134]: Lithium electrode evolution under different stripping conditions.

Thanks to tomography, Taiwo *et al.*[133] demonstrated the pit-like holes on the lithium surface while discharging the cell (Figure 20). They also demonstrated the formation of mossy lithium while plating, which leads to an increase of the lithium thickness with repeated cycling.

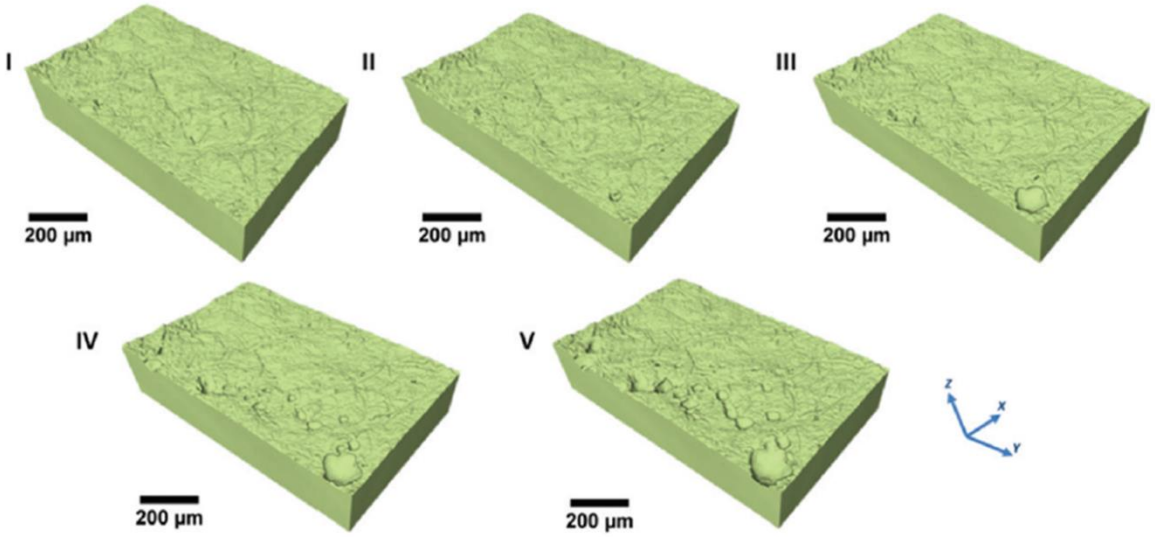

Figure 20[133]: 3D rendering of the lithium metal surface at different state of discharge.

Eastwood *et al.*[135], using phase contrast imaging, have demonstrated that the lithium is plated in a mossy metallic microstructure with a high surface area. The mossy structure is dependent on the current density applied.

1.6. Conclusion

To conclude, the large number of characterization techniques available provide a better understanding of the mechanisms involved in a Li/S cell while cycling and the degradation phenomena that occur. As demonstrated, many degradation phenomena occur in the first cycle, making mandatory to characterize this initial cycle in depth. In addition, improvement in *operando* tools allows nowadays to follow the system in the functioning environment and look at the morphological and structural evolutions. In particular, XRD allows probing the system *operando* and to better understand the evolution of crystalline species while cycling, especially the moment of appearance of different species and phases. Absorption tomography allows morphological changes of both electrodes to be followed. Coupling both techniques will allow the combined acquisition of both chemical and morphological information on the system[136].

Thanks to XRD and absorption tomography, the sulfur distribution, morphological change, loss of active surface area and loss of material utilization occurring in the positive electrode have been shown to have consequences on the electrochemical performance. In addition, dynamic processes have been partially characterized and a mechanism of crystalline species formation/disappearance has been proposed[25]. However, these analyses lack spatial and/or temporal resolution. It would be interesting to probe the composite positive electrode with 3D spatial and temporal resolutions to study its heterogeneities.

The lithium stripping/plating has also been characterized, and possible pitting during oxidation and mossy Li formation under certain cycling conditions have been reported. This behavior seems to be driven by the current density. It would be thus interesting to test different cell compositions and setting parameters, and see their influence on the lithium/electrolyte interface, especially in the Li/S system.

The objectives of this thesis follow the aforementioned observations. The purposes are thus to characterize both the sulfur and lithium electrodes under operating conditions in order to better understand the dynamic processes and degradation phenomena occurring while cycling, especially during the first cycle of a 3D positive electrode with a simple preparation process. Furthermore, probing the system in the *operando* mode allows the observation of the evolution

of the different species by both XRD and absorption tomography (chapter 2), to combine both chemical and morphological information on the system. Following the first experiment, thanks to preliminary results and improvement made on *operando* cell, X-ray Diffraction Computed Tomography (XRDCT), allowing 3D spatial resolution, has been coupled with absorption tomography, allowing the quantitative analysis of both the sulfur and the lithium electrodes (chapter 3). The dynamics of the sulfur species domains (α & β-S_8) while cycling have been followed through the depth of the electrode. At the lithium electrode side, the lithium/electrolyte interface has also been followed while cycling, to better understand the heterogeneities. Finally, with higher absorption tomography resolution and more accurate XRDCT (chapter 4), a complete analysis has been done concerning the positive electrode (from sulfur to Li_2S to sulfur). The lithium electrode has also been investigated by applying different cycling parameters (loading, C-rate and current density). All of the experimental details are described in the chapter 5, before concluding with the main results and perspectives of this work.

References

[1] S. Walus, Accumulateur Lithium/Soufre : Développement et Compréhension Des Mécanismes Électrochimiques, PhD Thesis, **2015**.

[2] "Lithium Ion Battery - an overview | ScienceDirect Topics," can be found under https://www.sciencedirect.com/topics/chemistry/lithium-ion-battery, **2012.**

[3] G. E. Blomgren, *J. Electrochem. Soc.* **2017**, *164*, A5019.

[4] J.-M. Tarascon, M. Armand, *Nature* **2001**, *414*, 359.

[5] M. S. Whittingham, *Chem. Rev.* **2004**, *104*, 4271.

[6] M. Yoshio, R. J. Brodd, A. Kozawa, Eds. , *Lithium-Ion Batteries: Science and Technologies*, Springer, New York, **2009**.

[7] M. Winter, J. O. Besenhard, M. E. Spahr, P. Novák, *Adv. Mater.* **1998**, *10*, 725.

[8] P. G. Bruce, S. A. Freunberger, L. J. Hardwick, J.-M. Tarascon, *Nat. Mater.* **2012**, *11*, 19.

[9] B. Scrosati, J. Hassoun, Y.-K. Sun, *Energy Environ. Sci.* **2011**, *4*, 3287.

[10] R. Fang, S. Zhao, Z. Sun, D.-W. Wang, H.-M. Cheng, F. Li, *Adv. Mater. Deerfield Beach Fla* **2017**, DOI 10.1002/adma.201606823.

[11] "Licerion® high energy density, lithium rechargeable battery," can be found under https://sionpower.com/

[12] "Oxis Energy - Next Generation Battery Technology," can be found under https://oxisenergy.com/

[13] X. Ji, L. F. Nazar, *J. Mater. Chem.* **2010**, *20*, 9821.

[14] H. Danuta, U. Juliusz, *Electric Dry Cells and Storage Batteries*, **1962**, US3043896A.

[15] *Stockage Éléectrochimique: Étude Stratégiques. Linksium*, **2017.**

[16] W. Xu, J. Wang, F. Ding, X. Chen, E. Nasybulin, Y. Zhang, J.-G. Zhang, *Energy Env. Sci* **2014**, *7*, 513.

[17] A. Manthiram, Y. Fu, S.-H. Chung, C. Zu, Y.-S. Su, *Chem. Rev.* **2014**, *114*, 11751.

[18] Z. Lin, C. Liang, *J. Mater. Chem. A* **2014**, *3*, 936.

[19] B. Meyer, *American Chemical Society*. **1975**.

[20] S. Waluś, C. Barchasz, J.-F. Colin, J.-F. Martin, E. Elkaïm, J.-C. Leprêtre, F. Alloin, *Chem. Commun. Camb. Engl.* **2013**, *49*, 7899.

[21] C. Villevieille, P. Novák, *J. Mater. Chem. A* **2013**, *1*, 13089.

[22] J. Conder, R. Bouchet, S. Trabesinger, C. Marino, L. Gubler, C. Villevieille, *Nat. Energy* **2017**, *244*, 61.

[23] C. Barchasz, F. Molton, C. Duboc, J.-C. Leprêtre, S. Patoux, F. Alloin, *Anal. Chem.* **2012**, *84*, 3973.

[24] M. Cuisinier, P.-E. Cabelguen, S. Evers, G. He, M. Kolbeck, A. Garsuch, T. Bolin, M. Balasubramanian, L. F. Nazar, *J. Phys. Chem. Lett.* **2013**, *4*, 3227.

[25] S. Waluś, C. Barchasz, R. Bouchet, J.-C. Leprêtre, J.-F. Colin, J.-F. Martin, E. Elkaïm, C. Baehtz, F. Alloin, *Adv. Energy Mater.* **2015**, *5*.

[26] Y.-J. Choi, Y.-D. Chung, C.-Y. Baek, K.-W. Kim, H.-J. Ahn, J.-H. Ahn, *J. Power Sources* **2008**, *184*, 548.

[27] Z. Li, L. Yuan, Z. Yi, Y. Sun, Y. Liu, Y. Jiang, Y. Shen, Y. Xin, Z. Zhang, Y. Huang, *Adv. Energy Mater.* **2014**, *4*, 1301473.

[28] J. Gao, M. A. Lowe, Y. Kiya, H. D. Abruña, *J.Physical Chemistry*. **2011**, *115*, 50.
[29] H. S. Ryu, H. J. Ahn, K. W. Kim, J. H. Ahn, K. K. Cho, T. H. Nam, *Electrochimica Acta* **2006**, *52*, 1563.
[30] H. Ryu, H. Ahn, K. Kim, J. Ahn, J. Lee, E. Cairns, *J. Power Sources* **2005**, *140*, 365.
[31] L. Zielke, C. Barchasz, S. Waluś, F. Alloin, J.-C. Leprêtre, A. Spettl, V. Schmidt, A. Hilger, I. Manke, J. Banhart, R. Zengerle, S. Thiele, *Sci. Rep.* **2015**, *5*, 10921.
[32] C. Barchasz, J.-C. Leprêtre, F. Alloin, S. Patoux, *J. Power Sources* **2012**, *199*, 322.
[33] G. Zheng, Y. Yang, J. J. Cha, S. S. Hong, Y. Cui, *Nano Lett.* **2011**, *11*, 4462.
[34] C. Liang, N. J. Dudney, J. Y. Howe, *Chem. Mater.* **2009**, *21*, 4724.
[35] R. Demir-Cakan, M. Morcrette, F. Nouar, C. Davoisne, T. Devic, D. Gonbeau, R. Dominko, C. Serre, G. Férey, J.-M. Tarascon, *J. Am. Chem. Soc.* **2011**, *133*, 16154.
[36] X. He, J. Ren, L. Wang, W. Pu, C. Jiang, C. Wan, *J. Power Sources* **2009**, *190*, 154.
[37] Y.-X. Yin, S. Xin, Y.-G. Guo, L.-J. Wan, *Angew. Chem. Int. Ed.* **2013**, *52*, 13186.
[38] Z.-Z. Yang, H.-Y. Wang, X.-B. Zhong, W. Qi, B.-Y. Wang, Q.-C. Jiang, *RSC Adv.* **2014**, *4*, 50964.
[39] Z. Li, J. Huang, B. Yann Liaw, V. Metzler, J. Zhang, *J. Power Sources* **2014**, *254*, 168.
[40] R. Cao, W. Xu, D. Lv, J. Xiao, J.-G. Zhang, *Adv. Energy Mater.* **2015**, *5*.
[41] H. J. Chang, N. M. Trease, A. J. Ilott, D. Zeng, L.-S. Du, A. Jerschow, C. P. Grey, *J. Phys. Chem. C* **2015**, *119*, 16443.
[42] M. Rosso, C. Brissot, A. Teyssot, M. Dollé, L. Sannier, J.-M. Tarascon, R. Bouchet, S. Lascaud, *Electrochimica Acta* **2006**, *51*, 5334.
[43] F. Orsini, A. Du Pasquier, B. Beaudoin, J. M. Tarascon, M. Trentin, N. Langenhuizen, E. De Beer, P. Notten, *J. Power Sources* **1998**, *76*, 19.
[44] D. Zheng, X.-Q. Yang, D. Qu, *ChemSusChem* **2016**, *9*, 2348.
[45] R. Bouchet, *Nat. Nanotechnol.* **2014**, *9*, 572.
[46] M. Winter, W. K. Appel, B. Evers, T. Hodal, K.-C. Möller, I. Schneider, M. Wachtler, M. R. Wagner, G. H. Wrodnigg, J. O. Besenhard, *Monatshefte Für Chem. Chem. Mon.* **2016**, *132*, 473.
[47] K. Edström, T. Gustafsson, J. O. Thomas, *Electrochimica Acta* **2004**, *50*, 397.
[48] F. Sun, R. Moroni, K. Dong, H. Markötter, D. Zhou, A. Hilger, L. Zielke, R. Zengerle, S. Thiele, J. Banhart, I. Manke, *ACS Energy Lett.* **2017**, *2*, 94.
[49] M. S. Park, S. B. Ma, D. J. Lee, D. Im, S.-G. Doo, O. Yamamoto, *Sci. Rep.* **2014**, *4*, 3335.
[50] C. Barchasz, J.-C. Leprêtre, S. Patoux, F. Alloin, *Electrochimica Acta* **2013**, *89*, 737.
[51] C. Barchasz, Development of Lithium-Sulfur Batteries, Theses, Université de Grenoble, **2011**.
[52] G. Li, Z. Li, B. Zhang, Z. Lin, in *Front Energy Res*, **2015**.
[53] S. S. Zhang, *J. Power Sources* **2013**, *231*, 153.
[54] K. Xu, *Chem. Rev.* **2004**, *104*, 4303.
[55] J.-W. Choi, J.-K. Kim, G. Cheruvally, J.-H. Ahn, H.-J. Ahn, K.-W. Kim, *Electrochimica Acta* **2007**, *52*, 2075.
[56] H.-S. Ryu, H.-J. Ahn, K.-W. Kim, J.-H. Ahn, K.-K. Cho, T.-H. Nam, J.-U. Kim, G.-B. Cho, *J. Power Sources* **2006**, *163*, 201.

[57] M. I. Nandasiri, L. E. Camacho-Forero, A. M. Schwarz, V. Shutthanandan, S. Thevuthasan, P. B. Balbuena, K. T. Mueller, V. Murugesan, *Chem. Mater.* **2017**, *29*, 4728.
[58] Q. Zou, Y.-C. Lu, *J. Phys. Chem. Lett.* **2016**, *7*, 1518.
[59] R. Dominko, R. Demir-Cakan, M. Morcrette, J.-M. Tarascon, *Electrochem. Commun.* **2011**, *13*, 117.
[60] H. Yamin, *J. Electrochem. Soc.* **1988**, *135*, 1045.
[61] F. Gaillard, E. Levillain, J. P. Lelieur, *J. Electroanal. Chem.* **1997**, *432*, 129.
[62] M. Barghamadi, A. S. Best, A. I. Bhatt, A. F. Hollenkamp, M. Musameh, R. J. Rees, T. Rüther, *Energy Env. Sci* **2014**, *7*, 3902.
[63] D. Aurbach, E. Pollak, R. Elazari, G. Salitra, C. S. Kelley, J. Affinito, *J. Electrochem. Soc.* **2009**, *156*, A694.
[64] X. Liang, Z. Wen, Y. Liu, M. Wu, J. Jin, H. Zhang, X. Wu, *J. Power Sources* **2011**, *196*, 9839.
[65] Z. W. Seh, Y. Sun, Q. Zhang, Y. Cui, *Chem. Soc. Rev.* **2016**, *45*, 5605.
[66] X. Ji, K. T. Lee, L. F. Nazar, *Nat. Mater.* **2009**, *8*, 500.
[67] B. Zhang, X. Qin, G. R. Li, X. P. Gao, *Energy Environ. Sci.* **2010**, *3*, 1531.
[68] Z. Li, Y. Jiang, L. Yuan, Z. Yi, C. Wu, Y. Liu, P. Strasser, Y. Huang, *ACS Nano* **2014**, *8*, 9295.
[69] K. H. Kim, Y.-S. Jun, J. A. Gerbec, K. A. See, G. D. Stucky, H.-T. Jung, *Carbon* **2014**, *69*, 543.
[70] K. Xi, B. Chen, H. Li, R. Xie, C. Gao, C. Zhang, R. V. Kumar, J. Robertson, *Nano Energy* **2015**, *12*, 538.
[71] S. Dörfler, M. Hagen, H. Althues, J. Tübke, S. Kaskel, M. J. Hoffmann, *Chem. Commun.* **2012**, *48*, 4097.
[72] S. Liatard, K. Benhamouda, A. Fournier, R. Ramos, C. Barchasz, J. Dijon, *Chem. Commun. Camb. Engl.* **2015**, *51*, 7749.
[73] G. Zhou, S. Pei, L. Li, D.-W. Wang, S. Wang, K. Huang, L.-C. Yin, F. Li, H.-M. Cheng, *Adv. Mater.* **2014**, *26*, 625.
[74] J. He, Y. Chen, P. Li, F. Fu, Z. Wang, W. Zhang, *J. Mater. Chem. A* **2015**, *3*, 18605.
[75] S. Waluś, C. Barchasz, R. Bouchet, J.-F. Martin, J.-C. Leprêtre, F. Alloin, *Electrochimica Acta* **2016**, *211*, 697.
[76] S. Waluś, C. Barchasz, R. Bouchet, J.-F. Martin, J.-C. Leprêtre, F. Alloin, *Electrochimica Acta* **2015**, *180*, 178.
[77] D. Aurbach, E. Zinigrad, H. Teller, P. Dan, *J. Electrochem. Soc.* **2000**, *147*, 1274.
[78] C. Brissot, *J. Electrochem. Soc.* **1999**, *146*, 4393.
[79] X. Chen, T.-Z. Hou, B. Li, C. Yan, L. Zhu, C. Guan, X.-B. Cheng, H.-J. Peng, J.-Q. Huang, Q. Zhang, *Energy Storage Mater.* **2017**.
[80] D. P. Wilkinson, H. Blom, K. Brandt, D. Wainwright, *J. Power Sources* **1991**, *36*, 517.
[81] L. Gireaud, S. Grugeon, S. Laruelle, B. Yrieix, J.-M. Tarascon, *Electrochem. Commun.* **2006**, *8*, 1639.
[82] Y. Li, J. Jiao, J. Bi, X. Wang, Z. Wang, L. Chen, *Nano Energy* **2017**, *32*, 241.
[83] C. Zhang, W. Lv, G. Zhou, Z. Huang, Y. Zhang, R. Lyu, H. Wu, Q. Yun, F. Kang, Q.-H. Yang, *Adv. Energy Mater.* **2018**, *8*, 1703404.

[84] X.-B. Cheng, J.-Q. Huang, Q. Zhang, *J. Electrochem. Soc.* **2018**, *165*, A6058.
[85] D. Aurbach, A. Rosenman, E. Markevich, G. Salitra, F. F. Chesneau, *Meet. Abstr.* **2015**, *MA2015-02*, 36.
[86] I. Bauer, S. Thieme, J. Brückner, H. Althues, S. Kaskel, *J. Power Sources* **2014**, *251*, 417.
[87] J. Conder, A. Forner-Cuenca, E. M. Gubler, L. Gubler, P. Novák, S. Trabesinger, *ACS Appl. Mater. Interfaces* **2016**, *8*, 18822.
[88] R. Xu, J. Lu, K. Amine, *Adv. Energy Mater.* **2015**, *5*, n/a.
[89] M. U. M. Patel, R. Demir-Cakan, M. Morcrette, J.-M. Tarascon, M. Gaberscek, R. Dominko, *ChemSusChem* **2013**, *6*, 1177.
[90] M. U. M. Patel, R. Dominko, *ChemSusChem* **2014**, *7*, 2167.
[91] M. Hagen, P. Schiffels, M. Hammer, S. Dörfler, J. Tübke, M. J. Hoffmann, H. Althues, S. Kaskel, *J. Electrochem. Soc.* **2013**, *160*, A1205.
[92] S.-H. Yu, X. Huang, K. Schwarz, R. Huang, T. A. Arias, J. D. Brock, H. D. Abruña, *Energy Environ. Sci.* **2018**, *11*, 202.
[93] Y. Cui, A. Abouimrane, J. Lu, T. Bolin, Y. Ren, W. Weng, C. Sun, V. A. Maroni, S. M. Heald, K. Amine, *J. Am. Chem. Soc.* **2013**, *135*, 8047.
[94] H. S. Ryu, Z. Guo, H. J. Ahn, G. B. Cho, H. Liu, *J. Power Sources* **2009**, *189*, 1179.
[95] J. Nelson, S. Misra, Y. Yang, A. Jackson, Y. Liu, H. Wang, H. Dai, J. C. Andrews, Y. Cui, M. F. Toney, *J. Am. Chem. Soc.* **2012**, *134*, 6337.
[96] N. A. Cañas, S. Wolf, N. Wagner, K. A. Friedrich, *J. Power Sources* **2013**, *226*, 313.
[97] J. Conder, C. Villevieille, *Curr. Opin. Electrochem.* **2018**, *9*, 33.
[98] A. Cedola, G. Campi, D. Pelliccia, I. Bukreeva, M. Fratini, Manfred Burghammer, L. Rigon, F. Arfelli, R. C. Chen, D. Dreossi, N. Sodini, Sara Mohammadi, G. Tromba, R. Cancedda, M. Mastrogiacomo, *Phys. Med. Biol.* **2014**, *59*, 189.
[99] S. Risse, C. J. Jafta, Y. Yang, N. Kardjilov, A. Hilger, I. Manke, M. Ballauff, *Phys. Chem. Chem. Phys.* **2016**, *18*, 10630.
[100] S. R. Chae, J. Moon, S. Yoon, S. Bae, P. Levitz, R. Winarski, P. J. M. Monteiro, *Int. J. Concr. Struct. Mater.* **2013**, *7*, 95.
[101] M. Morcrette, Y. Chabre, G. Vaughan, G. Amatucci, J.-B. Leriche, S. Patoux, C. Masquelier, J.-M. Tarascon, *Electrochimica Acta* **2002**, *47*, 3137.
[102] M. Hagen, P. Fanz, J. Tübke, *J. Power Sources* **2014**, *264*, 30.
[103] J. Kulisch, H. Sommer, T. Brezesinski, J. Janek, *Phys. Chem. Chem. Phys.* **2014**, *16*, 18765.
[104] M. A. Lowe, J. Gao, H. D. Abruña, *RSC Adv.* **2014**, *4*, 18347.
[105] U. Kleuker, in (Ed.: U. Bonse), San Diego, CA, **1997**, pp. 245–256.
[106] P. Bleuet, E. Welcomme, E. Dooryhée, J. Susini, J.-L. Hodeau, P. Walter, *Nat. Mater.* **2008**, *7*, 468.
[107] K. M. Ø. Jensen, X. Yang, J. V. Laveda, W. G. Zeier, K. A. See, M. D. Michiel, B. C. Melot, S. A. Corr, S. J. L. Billinge, *J. Electrochem. Soc.* **2015**, *162*, A1310.
[108] J. Sottmann, M. Di Michiel, H. Fjellvåg, L. Malavasi, S. Margadonna, P. Vajeeston, G. Vaughan, D. S. Wragg, *ArXiv170304337 Cond-Mat* **2017**.
[109] J. Sottmann, M. Di Michiel, H. Fjellvåg, L. Malavasi, S. Margadonna, P. Vajeeston, G. B. M. Vaughan, D. S. Wragg, *Angew. Chem. Int. Ed Engl.* **2017**, *56*, 11385.

[110] P. Pietsch, M. Hess, W. Ludwig, J. Eller, V. Wood, *Sci. Rep.* **2016**, *6*, DOI 10.1038/srep27994.
[111] C. Rincón-Guio, A. María Gomez Aroca, J. Charry, *Imaging Med.* **2017**, *9*.
[112] A. Liang, Y. Zhang, X. Zhang, X. Yang, N. McLaughlin, X. Chen, Y. Guo, S. Jia, S. Zhang, L. Wang, J. Tang, *Soil Tillage Res.* **2019**, *185*, 94.
[113] A. Corral, M. Balcerzyk, M. Gallardo, C. A. Amorim, Á. Parrado-Gallego, R. Risco, *Theriogenology* **2018**, *119*, 183.
[114] M. Atlan, G. Nuti, H. Wang, S. Decker, T. Perry, *J. Mech. Behav. Biomed. Mater.* **2018**, *88*, 377.
[115] W. Vågberg, J. Persson, L. Szekely, H. M. Hertz, *Sci. Rep.* **2018**, *8*, 11014.
[116] R. R. Patel, A. Noshchenko, R. Dana Carpenter, T. Baldini, C. P. Frick, V. V. Patel, C. M. Yakacki, *J. Biomech. Eng.* **2018**, *140*, 101011.
[117] A. Blazejczyk, A. Blazejczyk, *Materials* **2018**, *11*, 1717.
[118] E. Maire, L. SALVO, P. CLOETENS, M. Di Michiel, *Tomographie à Rayons X Appliquée à l'étude Des Matériaux*, **2013.**
[119] M. Ebner, F. Geldmacher, F. Marone, M. Stampanoni, V. Wood, *Adv. Energy Mater.* **2013**, *3*, 845.
[120] L. A. Jiao, X. Li, L. L. Ren, L. Y. Kong, Y. L. Hong, Z. W. Li, X. B. Huang, X. F. Tao, *Powder Technol.* **2015**, *281*, 1.
[121] P. R. Shearing, L. E. Howard, P. S. Jørgensen, N. P. Brandon, S. J. Harris, *Electrochem. Commun.* **2010**, *12*, 374.
[122] D. P. Finegan, M. Scheel, J. B. Robinson, B. Tjaden, I. Hunt, T. J. Mason, J. Millichamp, M. Di Michiel, G. J. Offer, G. Hinds, D. J. L. Brett, P. R. Shearing, *Nat. Commun.* **2015**, *6*, 6924.
[123] A. Etiemble, A. Tranchot, T. Douillard, H. Idrissi, E. Maire, L. Roué, *J. Electrochem. Soc.* **2016**, *163*, A1550.
[124] L. Zielke, T. Hutzenlaub, D. R. Wheeler, I. Manke, T. Arlt, N. Paust, R. Zengerle, S. Thiele, *Adv. Energy Mater.* **2014**, *4*.
[125] V. Wood, *Nat. Rev. Mater.* **2018**, *3*, 293.
[126] L. Li, J. Hou, *RSC Adv.* **2018**, *8*, 25325.
[127] T. J. Davis, D. Gao, T. E. Gureyev, A. W. Stevenson, S. W. Wilkins, *Nature* **1995**, *373*, 595.
[128] A. Groso, M. Stampanoni, R. Abela, P. Schneider, S. Linga, R. Müller, *Appl. Phys. Lett.* **2006**, *88*, 214104.
[129] A. Momose, T. Takeda, Y. Itai, K. Hirano, *Nat. Med.* **1996**, *2*, 473.
[130] J. E. Montgomery, M. J. Wesolowski, B. Wolkowski, R. Chibbar, E. C. R. Snead, J. Singh, M. Pettitt, P. S. Malhi, T. Barboza, G. Adams, *J. Med. Imaging* **2016**, *3*, 015504.
[131] R. Fitzgerald, *Phys. Today* **2000**, *53*, 23.
[132] A. Yermukhambetova, C. Tan, S. R. Daemi, Z. Bakenov, J. A. Darr, D. J. L. Brett, P. R. Shearing, *Sci. Rep.* **2016**, *6*, 35291.
[133] O. O. Taiwo, D. P. Finegan, J. M. Paz-Garcia, D. S. Eastwood, A. J. Bodey, C. Rau, S. A. Hall, D. J. L. Brett, P. D. Lee, P. R. Shearing, *Phys. Chem. Chem. Phys.* **2017**, *19*, 22111.

[134] F. Shi, A. Pei, D. T. Boyle, J. Xie, X. Yu, X. Zhang, Y. Cui, *Proc. Natl. Acad. Sci.* **2018**, *115*, 8529.
[135] D. S. Eastwood, P. M. Bayley, H. J. Chang, O. O. Taiwo, J. Vila-Comamala, D. J. L. Brett, C. Rau, P. J. Withers, P. R. Shearing, C. P. Grey, P. D. Lee, *Chem. Commun.* **2014**, *51*, 266.
[136] E. Zhao, K. Nie, X. Yu, Y.-S. Hu, F. Wang, J. Xiao, H. Li, X. Huang, *Adv. Funct. Mater.* **2018**, *28*, 1707543.

Table of figures

Chapter 2: Coupling X-ray diffraction and X-ray absorption tomography to probe a Li/S battery

2.1.Motivation of the work

The literature data review (see paragraph 1.2 in chapter 1) introduces the potential and the drawbacks of the Li/S technology. The lack of detailed understanding of the functioning of the system leads to practical limitations on its widespread. Understanding the mechanisms within the cell and the behavior of both electrodes is thus crucial for improving the performance of cell components and thus the economic viability of the system[1].

This chapter deals with *operando* X-ray absorption tomography coupled with *operando* and spatially resolved XRD diffraction study applied to the Li/S cell. The aim was to obtain semi-quantitative information on the chemical and morphological states of the battery while cycling, from the microscopic to the macroscopic length scale and for the different compounds within the Li/S cell. The consumption and deposition processes of metallic lithium, lithium sulfide and sulfur have been characterized during two charge/discharge cycles.

2.2.Experimental section

2.2.1. Cell configuration

The cell design used for the electrochemical cycling and *operando* characterizations of the Li/S battery is shown schematically in Figure 1 (see chapter 5 for more details).

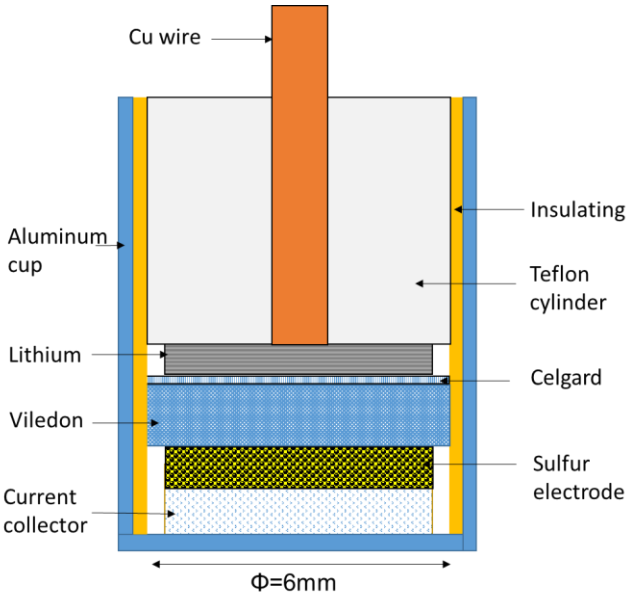

Figure 1: Schematic representation of the operando cell.

The design has been adapted from a typical coin cell, in order to have the necessary small cross-section required for high-resolution tomography measurements (1.2 µm/pixel), and rotational symmetry useful for the XRD characterization. The cell design for the experiment was chosen to be as close as possible to a real Li/S cell, while being small enough to make X-ray diffraction and tomography feasible at reasonable incident beam energies. The cell was sequentially studied by absorption tomography and spatially resolved diffraction with a recording frequency for one full measurement (diffraction and tomography) of approximately 20 min. During the measurements the cell was cycled at the theoretical rate of C/20 (charge and discharge in 20 hours), and the second cycle was performed at C/40. A typical voltage profile obtained with this cell at constant current is shown in Figure 2.a, each point corresponding to a tomographic measurement.

2.2.2. Electrochemical results

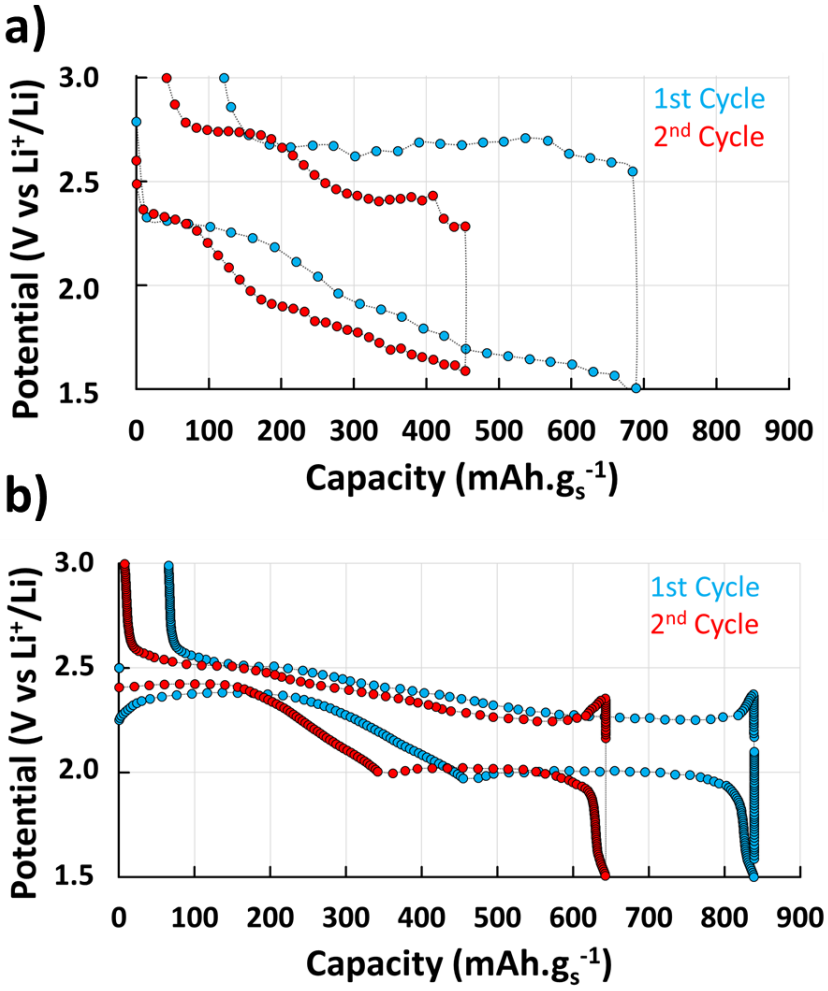

Figure 2: a) Voltage profile of operando Li/S cell. b) Typical voltage profile in CR2032 Li/S coin cell.

The profiles are compared favorably to the expected profiles in coin cells, as shown in Figure 2.b, although larger polarization and some noise are observed with the *operando* cell due to poor electrical contact while rotating the cell during tomography measurements. The expected plateaus are observed with capacity values in the same range of magnitude as obtained in coin cells. During recharging, a quasi-reversible process occurs, which allowed to validate the operando cell design.

2.3. Analysis of the initial state

Tomography gives information about the X-ray attenuation coefficient of the sample, but is insensitive to crystallinity and to the particular combination of chemical species and macroscopic density leading to a given absorption. Details of sub-micron particles are not visible due to the resolution of the system used for the tomography measurement. XRD, on the other hand, is sensitive to the different crystalline phases present in the sample. Coupling the two techniques therefore can give a complete picture of a sample over a large length scale, from atomic to macroscopic.

A tomographic slice of the cell in the initial state is shown in Figure 3, which shows the interest of combining these methods to characterize the state of the electrochemical cell. Less absorbing regions are represented by dark color whereas brighter regions correspond to high absorption.

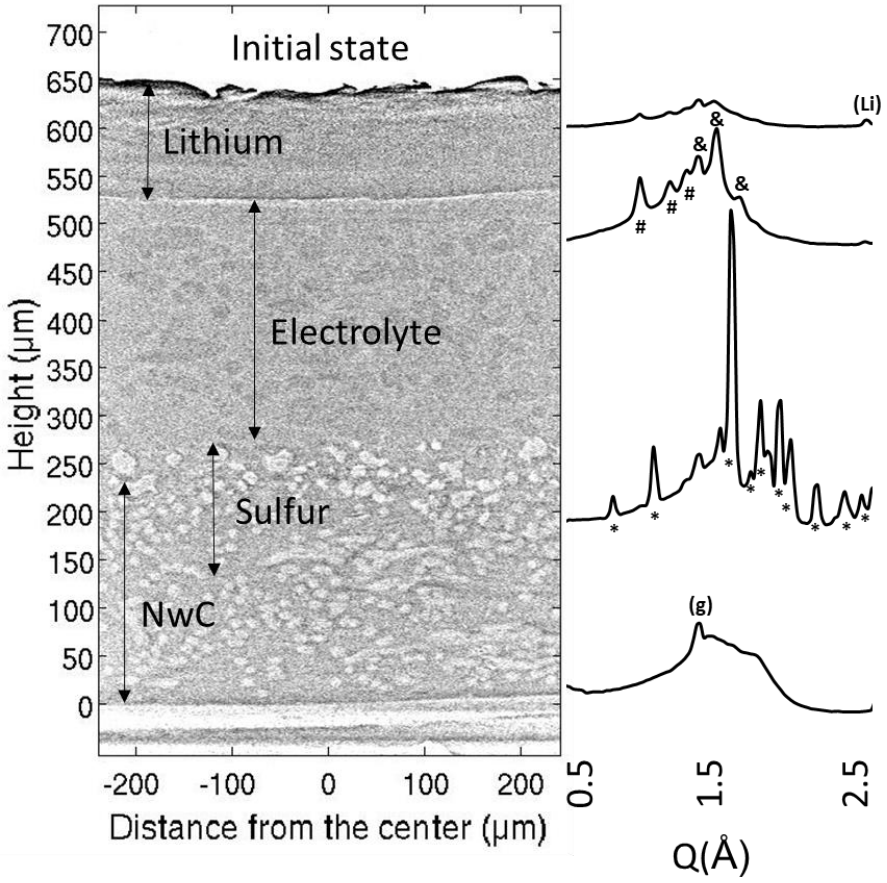

*Figure 3: Vertical slice of the tomographic cell at initial state with the associated X-Ray Diffraction (XRD) patterns ((g): graphite (NwC) // *: sulfur // #: celgard ® // &: viledon ® // (Li): lithium).*

The lithium layer is easily distinguished. In the initial state, this layer is homogeneous in density and relatively flat. The lithium thickness measures 126 µm on average, which is in good agreement with the supplier specifications (135 µm). Sulfur is initially deposited on top of the NwC, due to the coating process, forming a crust on the top of the current collector called carbon binder domain (CBD)[2]. The particle diameters are on the order of tens of micrometers. Thus the relevant features in the cell can be distinguished in spite of the low absorption of the constituent species and the high energy of the incident radiation.

XRD patterns taken all along the height of the cell in the initial state are shown in Figure 3. At the bottom of the cell (20 µm height), a peak due to graphitic carbon at 1.39Å (marked by (g)) is detectable only, and attributed to the NwC current collector. Higher in the cell (220 µm), the characteristic pattern of orthorhombic α-sulfur (labeled with *) can be seen. Above, the sulfur peaks vanish while the peaks from the components of the electrolyte layer (500 µm height), both Viledon® (#) and Celgard® (&) appear and persist until one observes the lithium layer marked by the peak (Li) at 2.54Å.

By comparing the 3-D tomographic reconstruction and XRD patterns in the initial state, it is thus possible to associate all of observed morphological objects with the corresponding chemical species. The cell was then cycled, and X-ray diffraction patterns and absorption data were measured *operando* as described above.

2.4. Analysis at different states of charge

Two vertical slices of the 3-D tomographic reconstructions at different states of charge are presented in Figure 4.a / Figure 4.b.

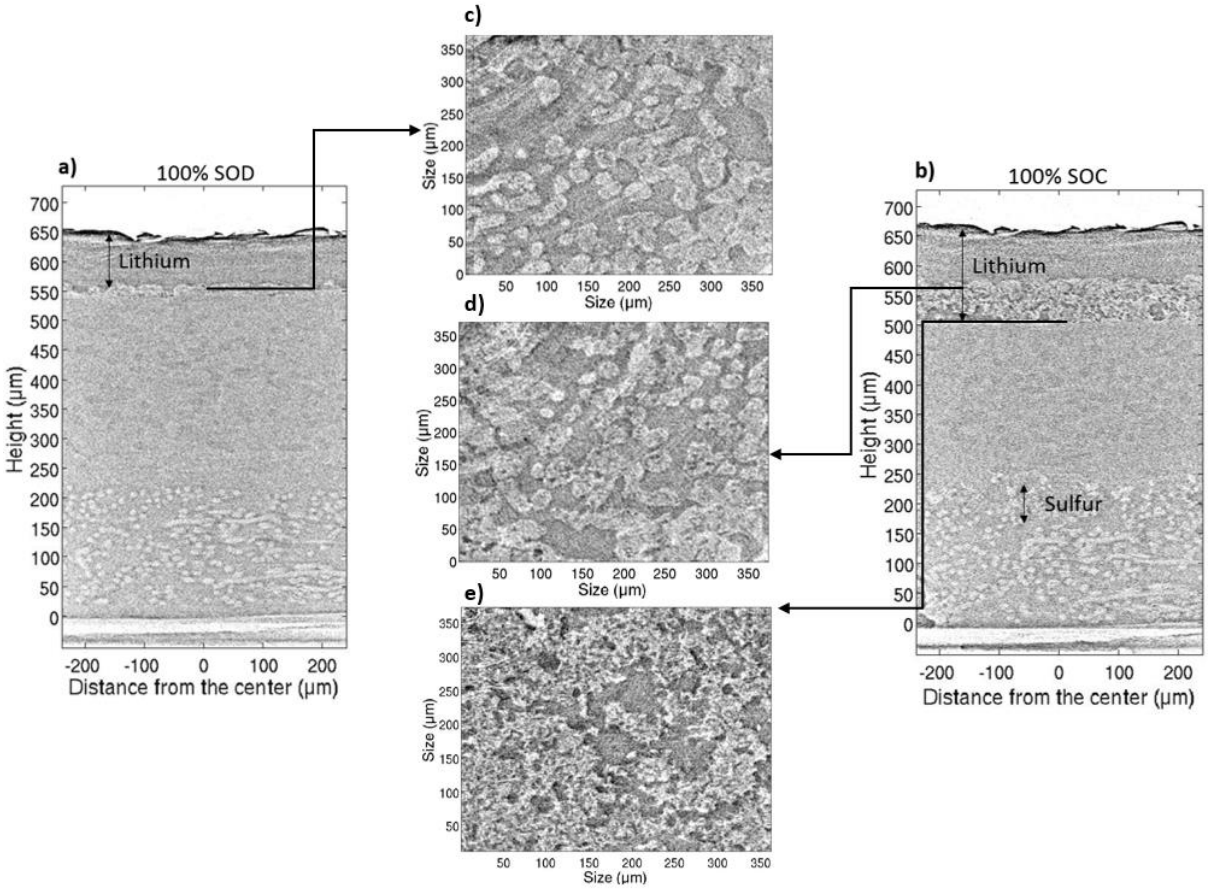

Figure 4: a) Vertical slice of the cell at the end of the first discharge (100%SOD). b) Vertical slice of the cell at the end of the first charge (100% SOC). c) Horizontal slice of the cell at 100% SOD at 560 µm height. d) Horizontal slice of the cell at 100% SOC at 570 µm height. e) Horizontal slice of the cell at 100% SOC at 505 µm height.

The most obvious difference in the morphology of the cell components between the first discharge and the first charge is in the size and homogeneity of the lithium electrode (Figure 4.a / Figure 4.b). At the end of the first discharge, *i.e.* 100% state of discharge (100% SOD), due to lithium stripping, the interface between the lithium and the electrolyte is heterogeneous and not flat. However, the lithium layer is homogeneous in term of density. Figure 4.c shows that the oxidation of the lithium is localized and not uniform, which creates craters (light grey) and lithium pads (dark grey) corresponding to the non-oxidized lithium. As a consequence, the interface becomes heterogeneous and, as already demonstrated[3], such interface likely favors

nucleation and growth of dendrites during the subsequent recharges. Compared to the initial state (Figure 3), the average thickness of lithium has diminished from 126 to 106 µm (20 ± 3 µm have been consumed), while a stripping of a 14 µm thick lithium layer should be expected, according to the coulometry (2.7 $mAh.cm^{-2}$) and assuming a uniform oxidation process. This slight difference is consistent with a non-uniform oxidation of lithium layer. At the end of charge (100% SOC, Figure 4.b), the electrodeposited lithium forms a porous region, and a moss of lithium is observed at the interface between the dense native lithium and the electrolyte (Figure 4.e). Interestingly, the dense lithium is always 106 µm thick, which means that electrodeposited lithium is found almost entirely in the porous layer (Figure 4.d). At 100% SOC, the lithium layer measures approximately 164 µm, giving an average density of the deposited layer during first charge of 17% only. This value is very low and can easily explain the poor cycling behavior of the lithium anode in such a liquid-based electrolyte. The average density of the redeposited layer during the second cycle is approximately 21%, similar to the first cycle and indicating that the initial lithium morphology is never recovered upon cycling. These morphological changes in the lithium electrode have important consequences for the functioning of Li/S batteries. As deposited lithium is very porous, a strong impact on the reliability and safety[4] may be expected. Furthermore, the faradic efficiency of a mossy lithium electrode is very poor due to the formation of fresh SEI, which consumes electrolyte on the surface of the moss. As a consequence, rapid lithium electrode fading and poor cyclability may be expected as well, due to the presence of "dead" mossy lithium and expected electrolyte depletion[5].

2.5. Analysis in the *operando* mode

2.5.1. Amount of apparent lithium

In order to correlate the tomographic and diffraction data for the lithium layer, a comparison of the amount of apparent lithium in the electrode as measured by the two techniques was carried out, with the lithium volume determined by imaging compared to the quantity of lithium present as measured by the (100) peak area in XRD (Figure 5).

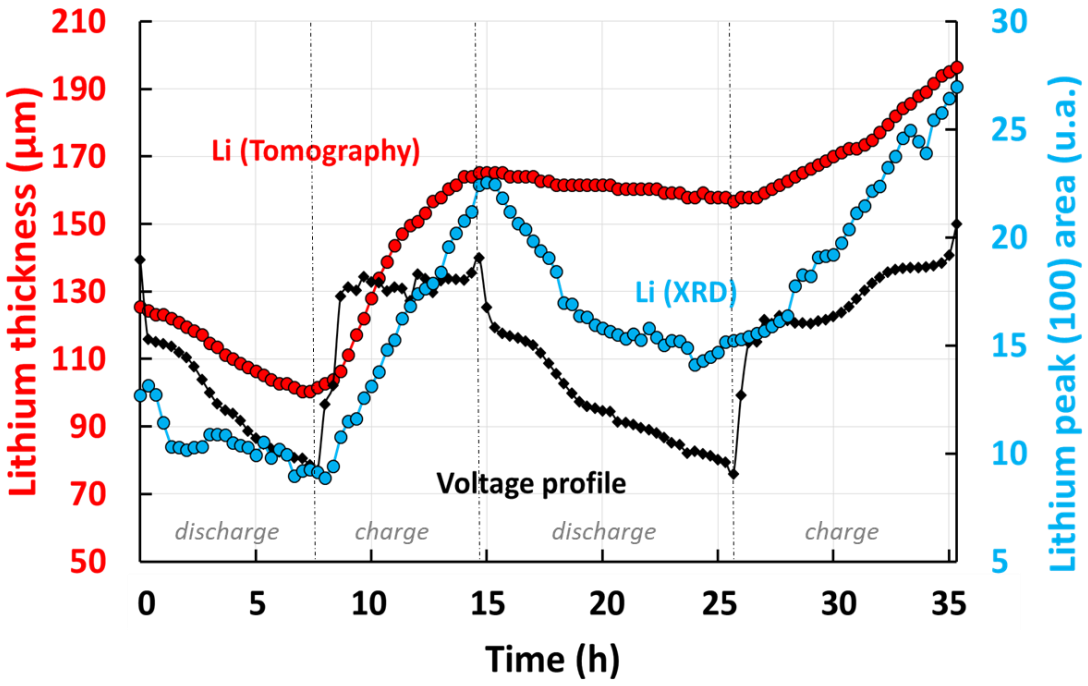

Figure 5: Comparison between tomography and XRD lithium analysis with the associated voltage profile.

As expected, the lithium thickness and total quantity as determined by XRD evolve qualitatively in accordance with the voltage profile during the first cycle. For the 2nd cycle, according to tomography data, the lithium thickness diminishes by 8 ± 3 µm during the 2nd discharge, in agreement with what would be expected from the coulometry (i.e. 8.8 µm). This confirms that solely the dense lithium was oxidized electrochemically while the mossy lithium does not participate to the electrochemical reactions. On the other hand, the quantity of lithium in the electrode is determined by XRD with possible measurements errors due to the lithium peak resolution. However, the overall tendency shows that the lithium seems to be significantly reduced. Even if, the lithium quantity calculation with possible measurements errors due to the lithium peak resolution. It seems like both the dense and mossy lithium may be oxidized during the discharge. Indeed, without participating to electrochemical reactions, the mossy lithium, with a well-developed surface, reacts strongly with the electrolyte and forms fresh SEI. This chemical oxidation consumes lithium without involving electrons in the external electric circuit.

2.5.2. Global evolution

In order to perform a similar density analysis over the entire cell and characterize its global evolution while cycling, density averages were taken over regions of 2400 µm² in the x-y plane (parallel to cylinder radius). A schematic representation is shown Figure 6.

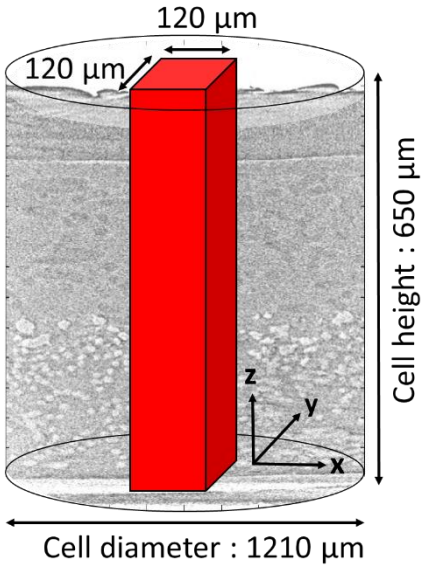

Figure 6: Schematic representation of volume integration.

This can be done without major loss of information, as the battery is to first approximation a 1D object with cylindrical symmetry (Figure 6). A median filter was applied with a radius of 5 pixels so as to reduce the noise in the reconstruction. By plotting the density of the layers over time, the composition of battery components and their positions within the cell could be followed during the two cycles (Figure 7.a to 7.d). As only local tomography was carried out, the values of the absorption are only relative, but are adequate to understand the evolution of the material present.

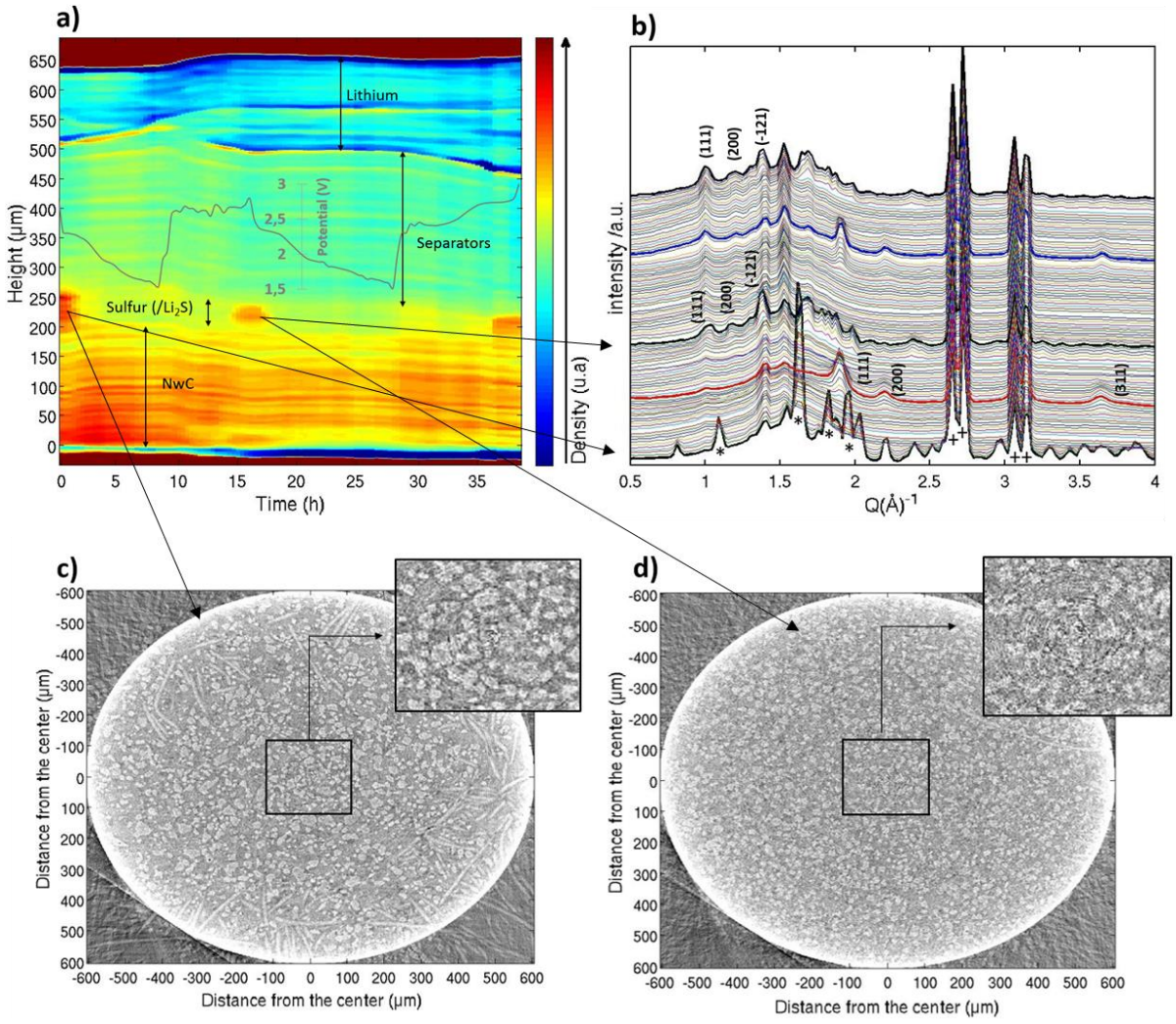

Figure 7: a) Integration over a plane of the 3D tomographic reconstruction showing median pixel values within each vertical layer during the two first cycles. b) Corresponding time evolution of the XRD pattern of the slice at 200 µm, corresponding to the top of the NwC. c) Horizontal slice in the carbon binder – sulfur domain, in the initial state and zoom of the 400 µm² indicated. d) Horizontal slice in the carbon binder – sulfur domain, at the end of first charge and zoom of the 400 µm² square indicated.

Lithium electrode

This representation allows following the lithium consumption and deposition processes during cycling and illustrates the negative electrode interface heterogeneity, as previously discussed. In Figure 7.a, the lithium layer clearly displays a strong variation of density at the interface between subsequent layer depositions. This effect is probably accentuated by the fact that no control of the pressure was applied to the cell and thus that the lithium interface was relatively free to evolve without constraints. As already mentioned before, these morphological changes

in the lithium electrode have important consequence for the cyclability and reliability of Li/S batteries.

Between the two electrodes, the electrolyte can be divided into two regions: one with a 24 µm thick Celgard® separator, found between the two yellow parts (501 to 525 µm in the initial state), and one with the additional Viledon® separator which measures 220 µm. The electrolyte is homogeneous while cycling, even if there is a slight decrease in density which could be interpreted by the electrolyte depletion, probably due to wetting of the lithium layer's porosity.

Sulfur electrode:

In positive electrode, the sulfur is associated with zones of higher density. Semi-quantitative analysis allows the determination of the penetration depth in the NwC. In the initial state, the sulfur is concentrated on the top of the NwC and penetrates to a depth of approximately 120 µm, a result of the initial coating process[6]. At the end of the first discharge, Li_2S is distributed over a depth of approximately 180 µm through the NwC. Sulfur grows at the end of the charge[7], and is also distributed over the same 180 µm depth. However, as the specific surface of carbon material is mainly brought by the initial coating on the top of the electrode, sulfur particles remain always more concentrated on the top of the NwC.

An analysis of the phase fractions of sulfur species as determined from the XRD is shown in Figure 8.

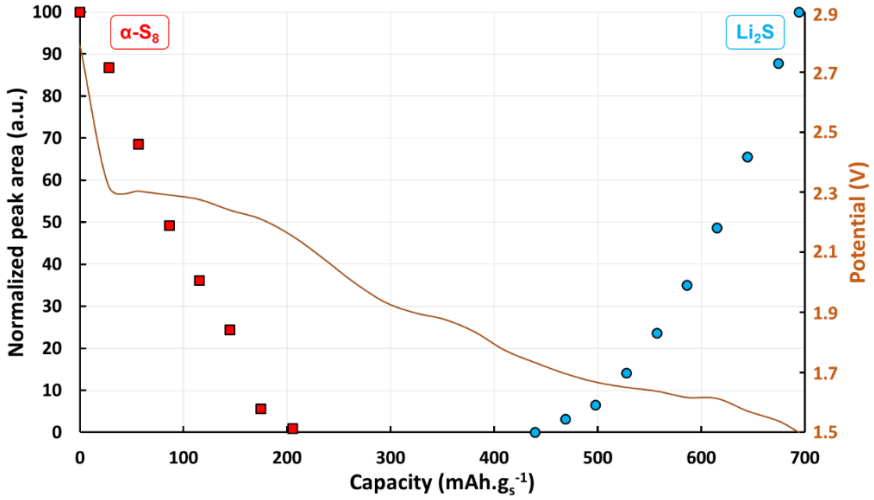

Figure 8: Phase fraction of sulfur species in the sulfur positive electrode as a function of the capacity of the cell.

It allows a more detailed analysis of the evolution of this region. In the initial state, the diffraction pattern at the electrode contains only orthorhombic α-sulfur peaks (four main peaks: " * ") and the peaks from the aluminum casing (+). During discharge, these peaks decrease linearly with time until their total disappearance at 205 $mAh.g_s^{-1}$, indicating complete reduction of sulfur, in good agreement with the theoretical capacity of this first region and with the literature data[8]. At this point, all sulfur species exist as soluble lithium polysulfides only[8]. Subsequently, the appearance of Li_2S is observed, and the quantity of Li_2S reaches a maximum at the end of discharge (blue pattern) before vanishing during charging. Ultimately, only 300 $mAh.g_s^{-1}$ is obtained during the second discharge plateau, which represents a quarter of the expected capacity on this plateau. This shows that the electrode discharge capacity is limited by the uncompleted deposition of insulating Li_2S product[9]. Looking at the XRD patterns collected along the cell, it is clear that Li_2S is also concentrated on the top of the NwC, while no crystalline Li_2S deposition on the top of to the lithium electrode can be detected in the present experiment. The growth of the Li_2S is reproducible during the second cycle. When sulfur reappears upon subsequent charging, and in all further cycles, it crystallizes as monoclinic β-S_8. Moreover, tomographic slices (Figure 7.c and Figure 7.d) show that sulfur particles grow back with a different global morphology. The electrochemical nucleation and growth of the β-S_8 leads to smaller particles with a narrower size distribution compared to the initial sulfur particles[2], and presumably the increased surface to volume ratio is the driving force for stabilizing the nominally metastable β-S_8.

2.6. Conclusion

To conclude, we have presented a *operando* characterization study of a Li/S cell, by combining electrochemistry with X-ray diffraction and absorption tomography. This unique combination of techniques enables the correlation of the structural and morphological state of the components with electrochemical behavior, allowing the identification of key phenomena in the battery. With X-ray diffraction, the temporal and spatial distribution of lithium, sulfur and Li_2S can be followed within the cell, while with tomography, the evolving morphology of the cell components is observed. An important observation explaining the functional behavior of these cells concerns "breathing" of the lithium plating/striping. The highly heterogeneous behavior of the lithium plating explains the poorly reversible consumption and deposition on the negative electrode while cycling, and is key to understand the whole system cyclability in these technologies. In this experiment, redeposited lithium was porous and the interface

between lithium and electrolyte was found to be quite heterogeneous, which may be related to the lack of pressure applied to the cell. In any case, these results point out the poor lithium metal reversibility in liquid-based electrolyte, and the need to address this issue. In this context, the characterization tools which have been described here seem to be highly relevant.

In the positive electrode, the quantity of sulfur decreases linearly with time until 25% SOD, then regrows in the β-form. This β-sulfur grows in smaller particles more sparsely distributed in the NwC with respect to the initial sulfur, as well as preferentially being deposited on the surface of the NwC electrode. As a next step of this work, sulfur active material and counterparts has been monitored into the electrode depth during cycling, which would allow for designing improved cathode structures. This is addressed in the next two chapters.

Finally, the combination of electrochemistry, absorption tomography and XRD gives a clear and detailed view of electrochemical cell components, allowing the correlation of macroscopic and microscopic phenomena in whole batteries under true *operando* conditions. By combining these tools, we can map the complex state of active materials in the entire cell, and correlate the physical state with electrochemical behavior. In particular, this allows us to demonstrate notably that the negative lithium electrode remains one of the main challenges of such technology.

Nevertheless, some improvements in the experimental procedure could be envisioned after this first experiment:

- Improvement of the cell design in order to control the pressure inside the cell, and increase the practical electrochemical response
- Improvement of spatial resolution in particular by performing XRD and absorption tomography at the same point

These two important points are addressed in the next chapter.

References

[1] J. Nelson, S. Misra, Y. Yang, A. Jackson, Y. Liu, H. Wang, H. Dai, J. C. Andrews, Y. Cui, M. F. Toney, *J. Am. Chem. Soc.* **2012**, *134*, 6337.

[2] L. Zielke, C. Barchasz, S. Waluś, F. Alloin, J.-C. Leprêtre, A. Spettl, V. Schmidt, A. Hilger, I. Manke, J. Banhart, R. Zengerle, S. Thiele, *Sci. Rep.* **2015**, *5*, 10921.

[3] Q. Chen, K. Geng, K. Sieradzki, *J. Electrochem. Soc.* **2015**, *162*, A2004.

[4] M. S. Park, S. B. Ma, D. J. Lee, D. Im, S.-G. Doo, O. Yamamoto, *Sci. Rep.* **2014**, *4*, DOI 10.1038/srep03815.

[5] L. Sannier, R. Bouchet, M. Rosso, J.-M. Tarascon, *J. Power Sources* **2006**, *158*, 564.

[6] S. Walus, Accumulateur Lithium/Soufre : Développement et Compréhension Des Mécanismes Électrochimiques, PhD Thesis, **2015**.

[7] S. Waluś, C. Barchasz, J.-F. Colin, J.-F. Martin, E. Elkaïm, J.-C. Leprêtre, F. Alloin, *Chem. Commun. Camb. Engl.* **2013**, *49*, 7899.

[8] S. Waluś, C. Barchasz, R. Bouchet, J.-C. Leprêtre, J.-F. Colin, J.-F. Martin, E. Elkaïm, C. Baehtz, F. Alloin, *Adv. Energy Mater.* **2015**, *5*, n/a.

[9] S. Risse, C. J. Jafta, Y. Yang, N. Kardjilov, A. Hilger, I. Manke, M. Ballauff, *Phys. Chem. Chem. Phys.* **2016**, *18*, 10630.

Table of figures

Chapter 3: Study of the Li/S dynamic processes by X-ray absorption and X-ray diffraction computed tomography

3.1. Motivation of the work

This chapter follows on from the previous chapter, taking into account the limitations noticed with the previous cell configuration and experimental set up, in order to go deeper into the mechanism and the limitations of Li/S cells. For that objective, another cell design has been developed to be as close as possible to a coin cell design, chosen as a reference. In particular, the pressure applied on the electrodes stack has been controlled on this new cell configuration. The electrode dimensions and the packaging have been chosen to optimize the resolution and the signal-to-noise ratio. In addition, for the purpose of spatially characterizing in the depth of the electrode when performing XRD, the beam has to be perfectly aligned with the cell which is practically not feasible. That is why, the new developed techniques X-ray diffraction computed tomography (XRDCT) has been applied in this second experiment. Indeed, it has been shown to be a powerful tool to produce time resolved 3-dimensional maps of the chemical state of working systems such as batteries[1,2], and the time and spatial resolutions available with this technique make it ideal for the study of a cycling Li/S cell. The technique gives structural information of chemical phase distribution in 3D. In addition, this technique separates the XRD signal of the casing and the electrodes and allows the acquisition of high quality and spatially resolved XRD data otherwise impossible to obtain. XRDCT can be coupled with higher spatial resolution X-ray absorption tomography in order to produce 3D-time-resolved maps from both techniques to obtain complementary and nearly simultaneous chemical and morphological information on the system under study.

In this chapter, the combination of XRDCT and absorption tomography was applied to characterize both the 3D sulfur electrode based on NwC current collector, as in the previous chapter, and the lithium anode in a pressure controlled specifically developed Li/S cell, during cell assembly. The use of 3D characterization techniques is particularly adapted for understanding the dynamic processes in such architecture positive electrode. The aim is to locally probe the system to understand the role of microscopic phenomena in battery operation, giving complementary information to the electrochemical performance, which provides only the global response of the system. By characterizing the system with high 3D spatial and time resolution, the dynamic processes occurring at both sulfur and lithium electrodes during cycling could be investigated with high accuracy.

3.2.Pressure-controlled *operando* cell

3.2.1. Cell design

Operando characterization requires the development of cells optimized for synchrotron data acquisition in both diffraction and absorption modes, while keeping electrochemical performance representative of classical systems such as coin cells. A new cell design has been developed for these *operando* characterizations, as shown in Figure 1.

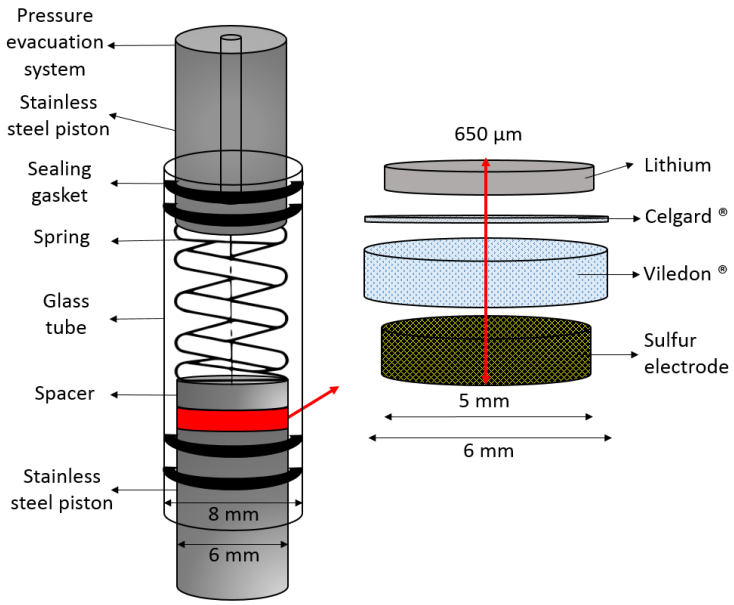

Figure 1: Schematic of the pressure-controlled operando cell.

This new type of cell allowed a better spatial and temporal resolution by reducing the electrode dimensions and by choosing appropriate materials. Indeed, as previously demonstrated[3,4], the pressure applied to the cell is a crucial parameter for optimizing electrochemical behavior. In particular, Yin *et al.*[4] showed that controlling the pressure enables the control of lithium metal growth and reversibility during stripping/plating cycles. They suggested that increasing the pressure could be an effective approach to mitigate dendrites growth. In this experiment, the pressure was fixed to 1.2 bar (similar to the pressure applied in a coin cell). The development of this cell is described in the chapter 5.

3.2.2. Electrochemical characterization

Two cells were characterized and cycled at C/20 (~0.4 mA.cm^{-2} / ~5 mg.cm^{-2}). The first cell ('Operando Cell (Half cycle)', blue in Figure 2) was cycled on the first quasi-plateau of sulfur

reduction only, which corresponds to the electrochemical reaction between sulfur and high-order polysulfides (PS). The second cell ('Operando Cell' black in Figure 2) was fully discharged and charged (from S_8 to Li_2S back to S_8). Cell performance was characterized with respect to standard coin cells. The electrochemical curves are shown in Figure 2 and compared with a reference coin cell (in red).

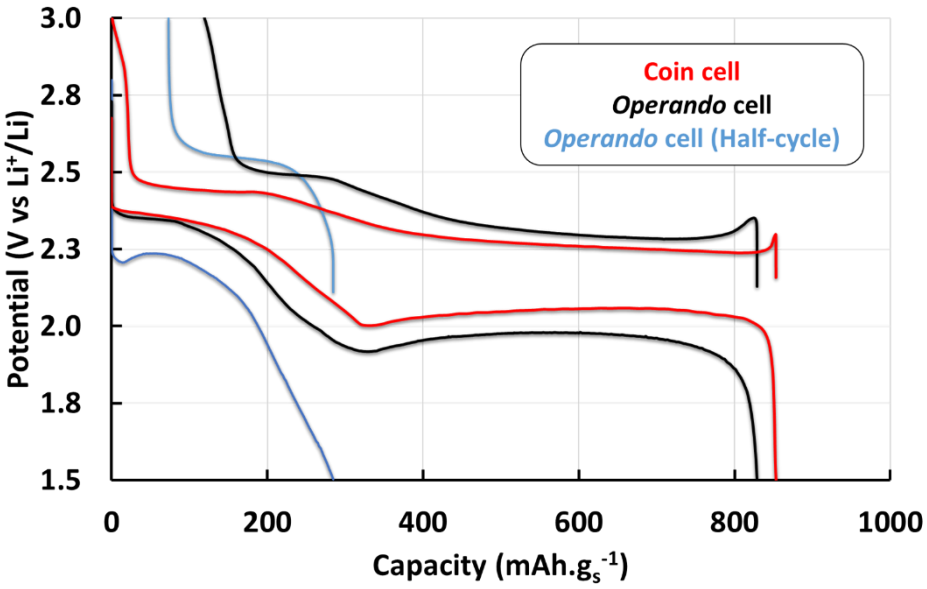

Figure 2: Galvanostatic electrochemical curves of reference coin cell and operando cells.

For the half-cycled cell, a typical cell voltage upon the first plateau was obtained but with a larger polarization than that observed in a coin cell. This polarization was possibly due to the rotating contacts and the high rotation speed of the cell needed for the acquisition of XRDCT data. However, the first quasi-plateau was observable and compared favorably to the expected specific capacity[5]. The charge was also representative of a Li/S system, with a pseudo-plateau attributed to sulfur formation[3]. For the second cell, only absorption tomography, was recorded in order to suppress the high rotation speed required for XRDCT and avoid issues of electrical contact. The galvanostatic performance was similar to a coin cell, taken as a reference.

3.3.Dynamic processes at the positive electrode

3.3.1. Initial state characterization

The half-cycled cell was characterized by phase contrast tomography, which allows better segmentation of similarly absorbing objects compared to pure absorption contrast tomography.

It was thus possible to better isolate the sulfur particles from the other cell components. A schematic representation of the electrode analyzed by absorption tomography is shown in Figure 3.

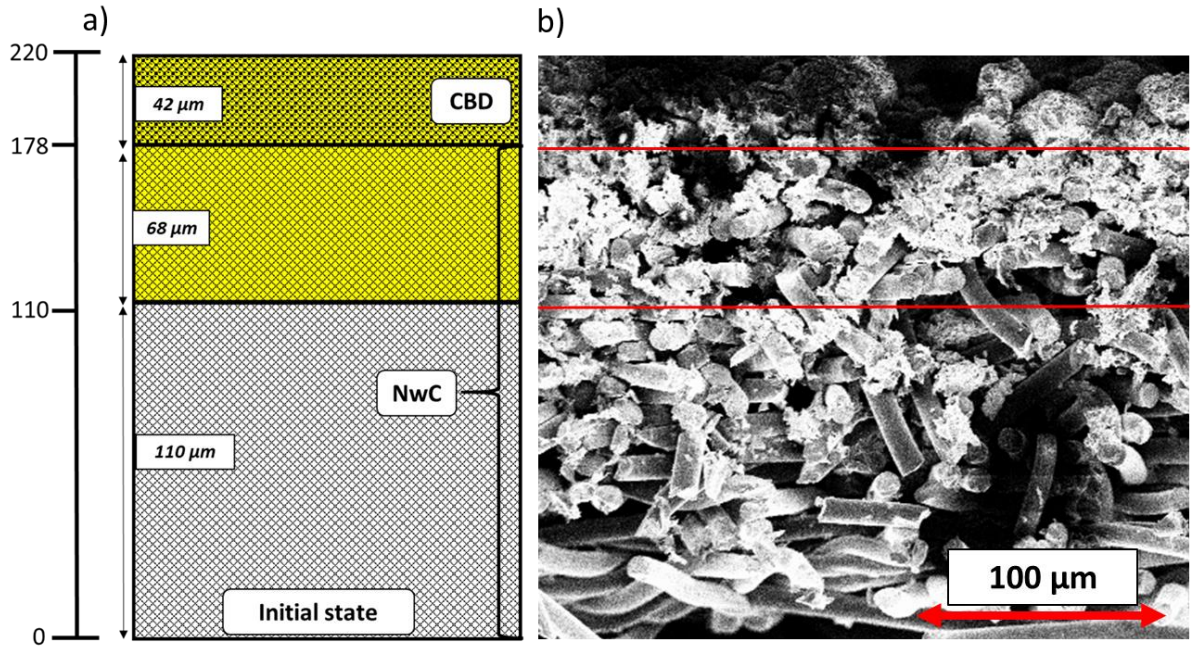

Figure 3: Schematic representation a) of the initial sulfur electrode b) and SEM cross-section of the NwC-supported sulfur electrode.

The upper zone, at the top of the electrode from 178 to 220 µm, is composed of the carbon black/binder/sulfur particles domain coated on the current collector. Throughout the rest of the manuscript, this zone is called as carbon binder domain (CBD) in extend of the commonly use of the term to describe this zone in the literature[6]. In the following, the zero of the z axis is defined as the bottom of the positive electrode. This CBD represents the ink coating on the top of the 3D current collector, where there is no evidence of carbon fibers. The ink also penetrates into the current collector (68 µm from the top; 110 to 178 µm height). One slice of the absorption tomogram, taken in the CBD, is shown in Figure 4.a.

In this horizontal cross-section of Figure 4.a, the red outer shape indicates the glass tube with an inner diameter of 6 mm. In the electrode, the higher absorption (red) corresponds to sulfur particles, which are distributed randomly in the electrode (with a less dense region on the right side probably due to electrode damage during cell assembly). It is also possible to see the Viledon® fibers in blue (at the top left), which are in contact with the CBD surface. In Figure 4.b, the sulfur particles were segmented using ImageJ computer software. This image shows

only sulfur particles (white) and the carbon binder domain (black). The sulfur particles are distributed randomly with a size of tens of micrometers, as expected for bare (non-cycled micron-sized) elemental sulfur particles[3].

The XRDCT technique allows the reconstruction of XRD patterns for each voxel (size: 300×300×20 μm^3). The reconstructed diffraction signal of a voxel, taken at the same depth as the tomographic slice at the center of the cell, prior to cycling, is shown in Figure 4.c. This shows the characteristic pattern of orthorhombic α-sulfur (labelled with *). Sulfur phase peaks were identified and integrated by subtracting a local linear background. The distribution of this phase (Figure 4.d) was obtained by integrating the (222) peak area of the orthorhombic α-sulfur phase in each voxel of the same CBD slice as shown in Figure 4.a. and Figure 4.b.

Figure 4 demonstrates that XRDCT and absorption tomography give completely consistent results, and confirms that sulfur particles are randomly distributed in the CBD, with the same less dense region visible in the two representations in the right part of the electrode.

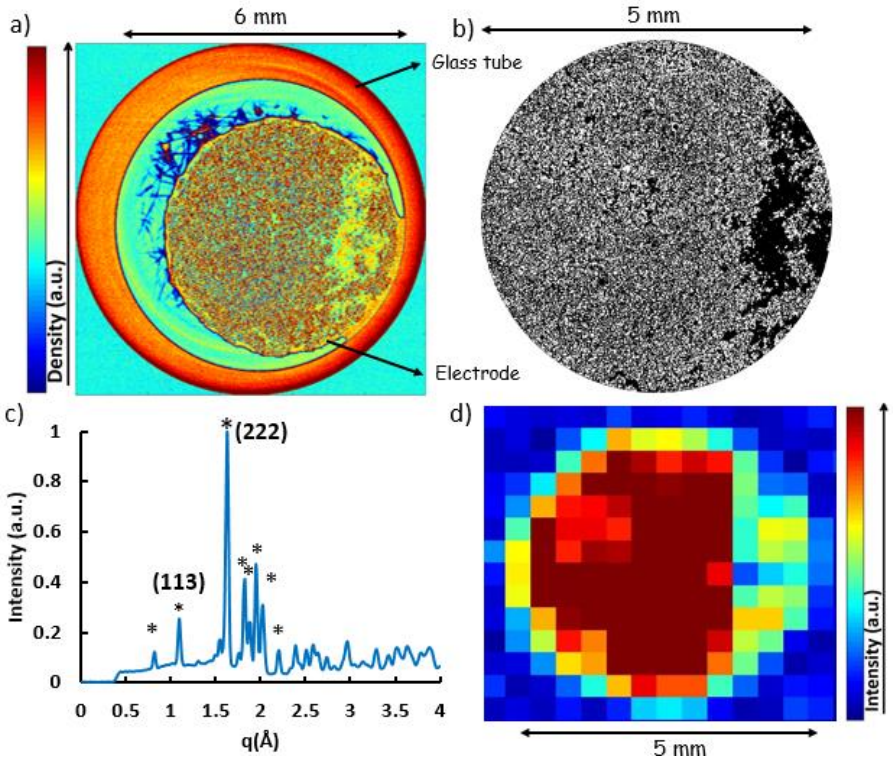

Figure 4. (a) Horizontal cross-section of the sulfur electrode top (CBD) for the cell in the initial state. (b) The same slice after segmentation of sulfur particles, zoom on the 5 mm diameter electrode region. (c) Reconstructed XRD pattern of one voxel in the center of the CBD slice (: sulfur peaks). (d) Variation of the (222) sulfur peak area in the same slice in the initial state.*

3.3.2. Global view of sulfur consumption

These two techniques allow tracking of the elemental sulfur distribution in the electrode while cycling, one by morphology contrast and one by crystallography. XRDCT also gives an unambiguous identification of the composition of regions in the case where the absorption of different materials is very similar. Solely the CBD part could be analyzed quantitatively by absorption tomography, as the segmentation between sulfur particles and carbon fibers was not possible in the NwC current collector region. Nonetheless, the entire electrode could be characterized, albeit at lower spatial resolution, from the XRDCT data.

The volume analyzed by absorption tomography was a cylinder of 5 mm in diameter and 42 µm in height. The sulfur particles were segmented for each tomogram in the CBD, and all pixels in this volume were integrated (black circles in Figure 5). The total amount of sulfur was normalized in relation to the initial amount of sulfur.

Phase evolution during cycling could be followed from the XRDCT data *via* the integration of the two most intense diffraction peaks over the full electrode thickness, including the CBD and the NwC. The normalized intensity averaged over the entire electrode is plotted as a function of the state of charge (SOC) in red diamonds in Figure 5. A dashed line is also drawn in order to see the theoretical evolution of sulfur quantity taking into account a linear decrease of sulfur to 209 $mAh.g_s^{-1}$ [7] associated with the reaction $S_8 + 2e^- \rightarrow S_8^{2-}$.

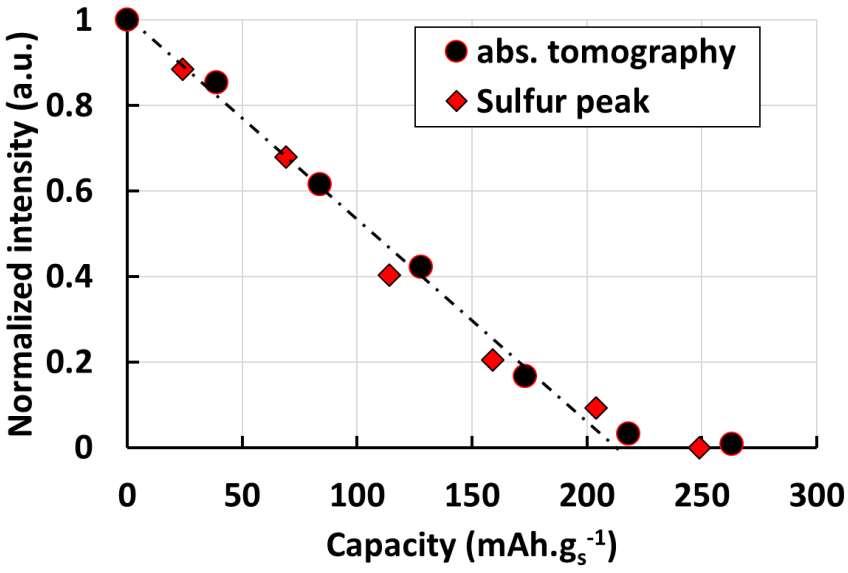

Figure 5: Evolution of sulfur quantity during 1st half discharge, in the electrode CBD from absorption tomography (black dots) and in the entire electrode thickness from XRDCT (red diamonds). The dashed line shows the derived linear decrease in sulfur quantity based on expected S_8 reduction to form S_8^{2-}.

The excellent agreement between the absorption tomography data taken from the CBD and the diffraction data taken over the entire electrode demonstrates that the average evolution of sulfur is homogeneous over the electrode thickness. It can be seen that the total volume of sulfur decreases linearly with time until approximately 210 $mAh.g_s^{-1}$ with a quasi-total reduction of sulfur. This is in good agreement with the theoretical capacity of the reaction $S_8 + 2e^- \rightarrow S_8^{2-}$ and with an unique conversion reaction during the first discharge plateau, as proposed by Walus *et al.*[8].

3.3.3. Local evolution of sulfur reduction

Mapping the 3D evolution of the distribution of sulfur particles within the electrode allows the local dynamics of sulfur consumption to be probed. This allows the dissolution mechanism to be understood with sufficient spatial resolution to understand the effect of electrode texture and thickness, in particular between the NwC (a sparse conductive network, far from the Li electrode) and CBD (in contact with the bulk electrolyte, dense conductive network).

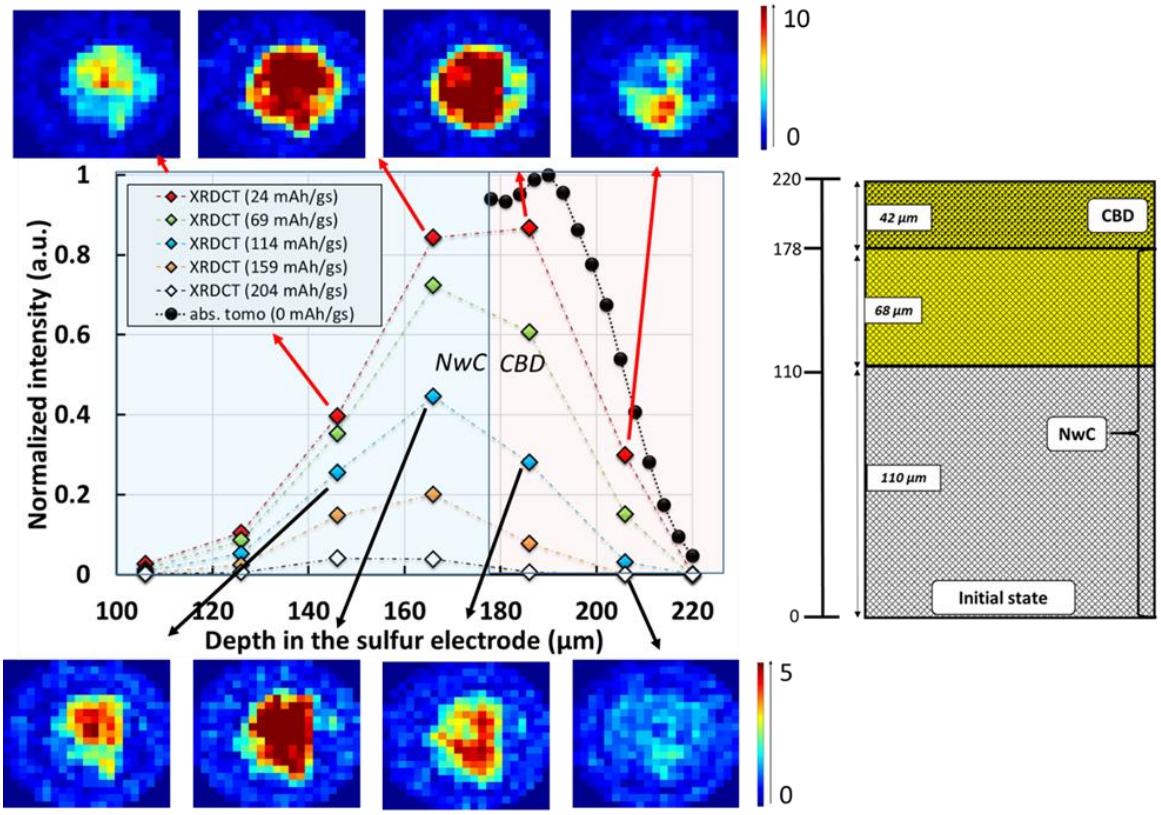

Figure 6: Evolution of sulfur quantity as determined by the sulfur (222) peak area through the depth of the electrode during 1st half discharge at different states of charge (SOC), based on XRDCT data. The graph shows the integrated intensity of 20 µm (the vertical resolution) slices; inset images show the distribution in the plane, with 300 µm resolution.

The distribution of sulfur at the beginning of the discharge (red diamonds in Figure 6) is an approximately bell-shaped curve; a result of both the particles size and the electrode fabrication process. When using doctor blade coating, the sulfur particles partially penetrate into the 3D current collector as previously discussed, but the sulfur loading remains maximum in the CBD (from 178 to 220 µm). The sulfur content diminishes in the NwC, probably due to the presence of carbon fibers. In addition, the viscosity of the ink and the sulfur particle size could limit the ink impregnation into the NwC while coating the electrode. Indeed, the loading is reduced by more than half compared to the maximum loading in the CBD. The sulfur is present initially over a depth of approximately 110 µm.

As shown in the RGB images in Figure 6, the sulfur is well distributed in the (x,y) plane with a similar distribution in the CBD and in the top of NwC. However, the evolution of sulfur content versus the state of charge is not homogeneous over the electrode thickness (Figure 7).

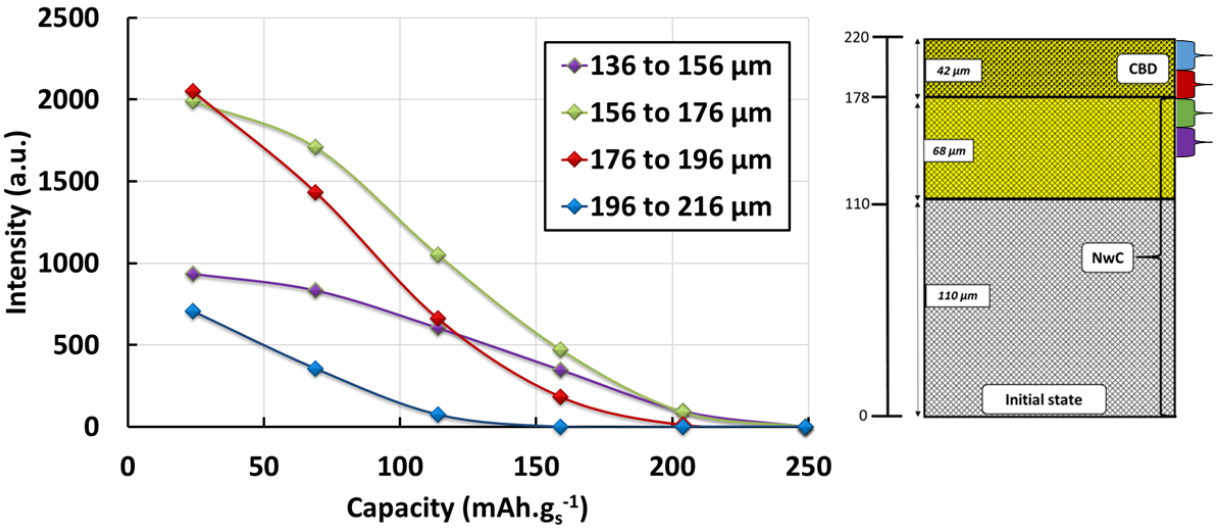

Figure 7: Evolution of sulfur quantity as a function of state of charge in the depth of the electrode based on XRDCT data.

In the CBD (blue and red curves in Figure 7), the kinetics of sulfur reduction are faster at the beginning of the discharge, and start to slow down after 100 mAh.g$_S^{-1}$. On the contrary, deeper in the electrode (green and purple, 136 to 176 µm), the evolution of sulfur quantity between the first two points curves (24 to 69 mAh.g$_S^{-1}$) is slow. This is due to the fact that the sulfur particles in the top layers of the electrode are easily accessible to lithium ions. Particles in these surface layers are reduced faster than the particles deeper in the electrode due to diffusion limitation. In addition, this explains why, in these top layers, sulfur vanishes before the theoretical value of 209 mAh.g$_S^{-1}$. This result is in perfect agreement with theoretical approaches explaining the limitations observed with thick electrode[9]. No limitations associated with electronic conductivity can be noticed in the 3D electrode thanks to its high electronic conductivity and morphology stability. The limitation is associated with ionic specie transport.

Thanks to the correlation established between the two data sets, the 3D analysis could be extended to higher spatial resolution. With the higher resolution tomography data, and the unambiguous identification of the sulfur from the XRDCT data, it was thus possible to follow the sulfur reduction in the whole CBD with a spatial resolution of 3 µm (Figure 8).

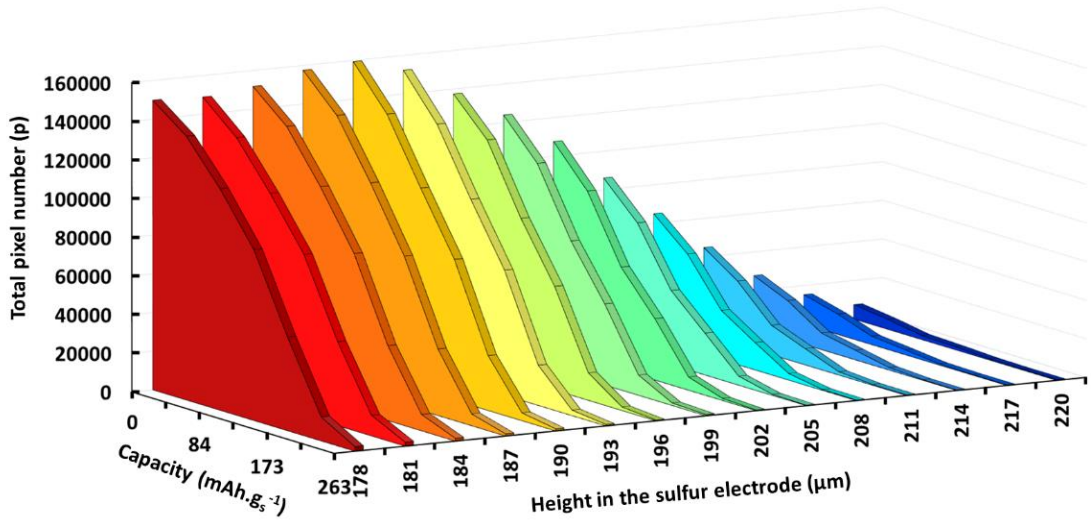

Figure 8: Evolution of sulfur quantity (total area of segmented sulfur particles in one slice) in the CBD during 1st half discharge and as a function of CBD depth, based on absorption tomography data.

In the initial state, the distribution of sulfur increases in the thickness of the electrode until it reaches a plateau. At the top of the CBD (214, 217, 220 µm in the electrode height), the reduction of sulfur is faster, as there is no more evidence of sulfur at 128-173 mAh.g_s^{-1}. Deeper, the sulfur distribution is homogenous from 178 to 193 µm in the initial state and upon discharge. Two tomogram images of the tomographic reconstruction of the CBD, one at 217 µm depth (black and white top images) and one at 181 µm depth (black and white bottom images) are compared in Figure 9. Each picture gives information about the sulfur particle cross-section in the tomogram images as a function of the state of charge. Each sulfur particle was segmented and mapped in color corresponding to the state of charge (initial state in red, 42 mAh.g_s^{-1}, in green, 84 mAh.g_s^{-1} in blue, 173 mAh.g_s^{-1} in cyan and 218 mAh.g_s^{-1} in pink).

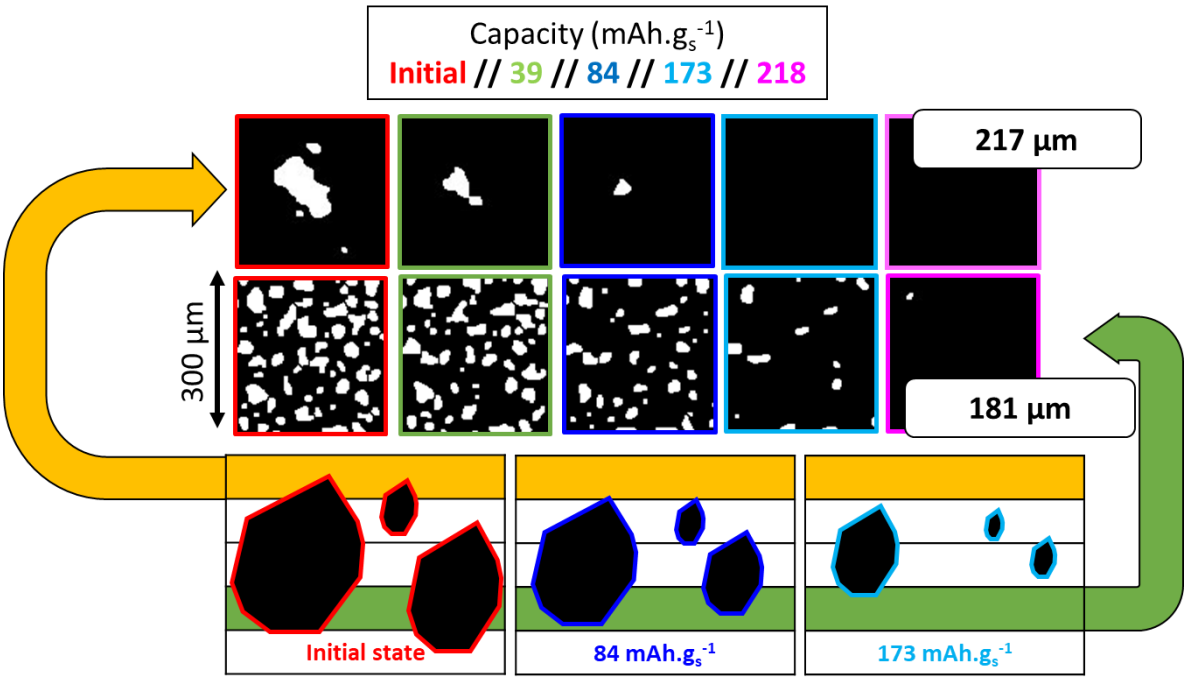

Figure 9: Evolution of sulfur particles in two CBD slices of the sulfur positive electrode versus time.

In Figure 9, at 217 µm height, only the tips of sulfur particles are visible in accordance to the observed particle size distribution, explaining why the amount of sulfur in the section is lower. In addition, at 173 mAh.g$_s^{-1}$ there is no more evidence of sulfur particles at 217 µm. This observation may be partially due to the fact that the reduction of the sulfur particles induces the decrease of the particle size and therefore the disappearance of sulfur on the top of the electrode, in addition to the more accessible particles at the surface of the electrode being preferentially reduced, as discussed previously.

Deeper in the electrode, at 181 µm height, the distribution of sulfur particles is homogeneous and the cross-sections observed come from all parts of the particles. Visually, there is a decrease in size and in number of projections over the discharge, which is coherent with the evolution of total sulfur quantity in the CBD (Figure 5).

In order to gain a schematic understanding of the kinetics, a semi-quantitative analysis was carried out by counting the surface projection in each slice. If assuming a simplified but broadly representative model with spherical particles, the volume of sulfur decreases with the surface projection in the power of three-halves (Figure 10).

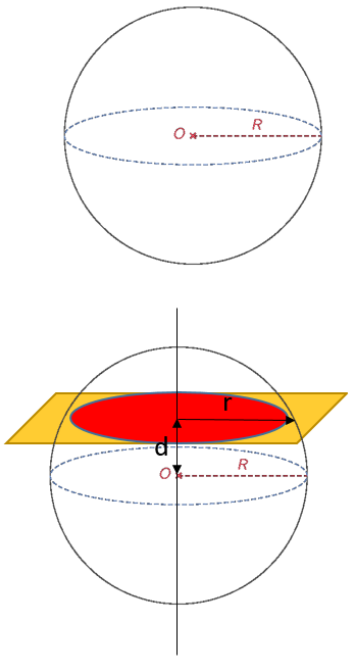

In first approximation, the sulfur particles could be likened to a sphere with a R radius.

The volume is given by : $V = \frac{4}{3}\Pi R^3$

The variation of volume is : $dV = \frac{4}{3}\Pi dR^3$

The evolution of the surface radius (r) is linked to the volume radius by:

$$R = (r^2 + d^2)^{1/2}$$

So the evolution of the radius is:

$$dR^3 = d(r^2 + d^2)^{3/2}$$

meaning an evolution of the projected surface proportional to a power of 3/2.

Figure 10: Explanation of projected surface evolution.

The kinetics of sulfur reduction in the CBD, *i.e.* its volume evolution (Figure 11), as measured by this approach, confirmed XRDCT data observations, but with a higher spatial resolution.

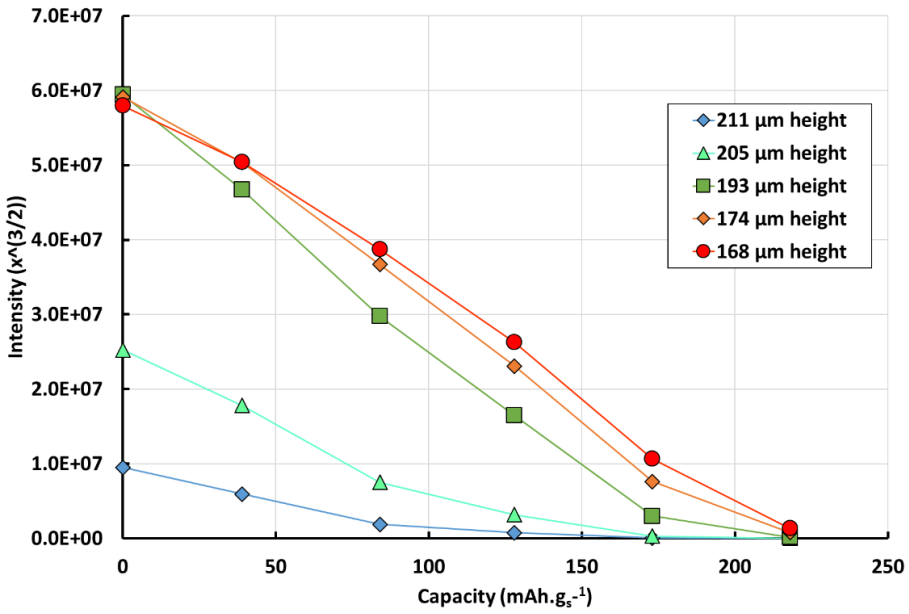

Figure 11: Evolution of sulfur quantity per slice based on absorption data.

There is rapid consumption of sulfur (concave curves) at the top of the CBD, with the sulfur there vanishing before the expected 209 $mAh.g_s^{-1}$. Deeper, the curve becomes more and more convex, proving that under these experimental conditions (C/20, TEGDME-DIOX, 1M LiTFSI based electrolyte, 5.1 $mg.cm^{-2}$), lithium ions diffusion drives the electrochemical kinetics in the electrode even in the CBD part with the sulfur consumption kinetic which decreases from 20 µm in depth of the electrode.

3.3.4. Sulfur characterization during charging process

3.3.4.1. Sulfur electrode morphology

The same analysis was carried out from the data recorded during charging. However, due to the resolution of absorption tomographic measurements, the smaller recrystallized sulfur particles could be distinguished but not meaningfully segmented. Thus, the morphological evolution could only be qualitatively described. Nevertheless, the breathing of the positive electrode could be analyzed during this half cycle.

In order to see the breathing of the positive electrode, density averages were taken over regions of 6.5 mm² (corresponding to 2.5 mm diameter in the center of the electrode) in the x-y plane (see chapter 2) and plotted *versus* capacity (Figure 12). The interface between the sulfur positive electrode and the electrolyte/separator was also plotted in dash line.

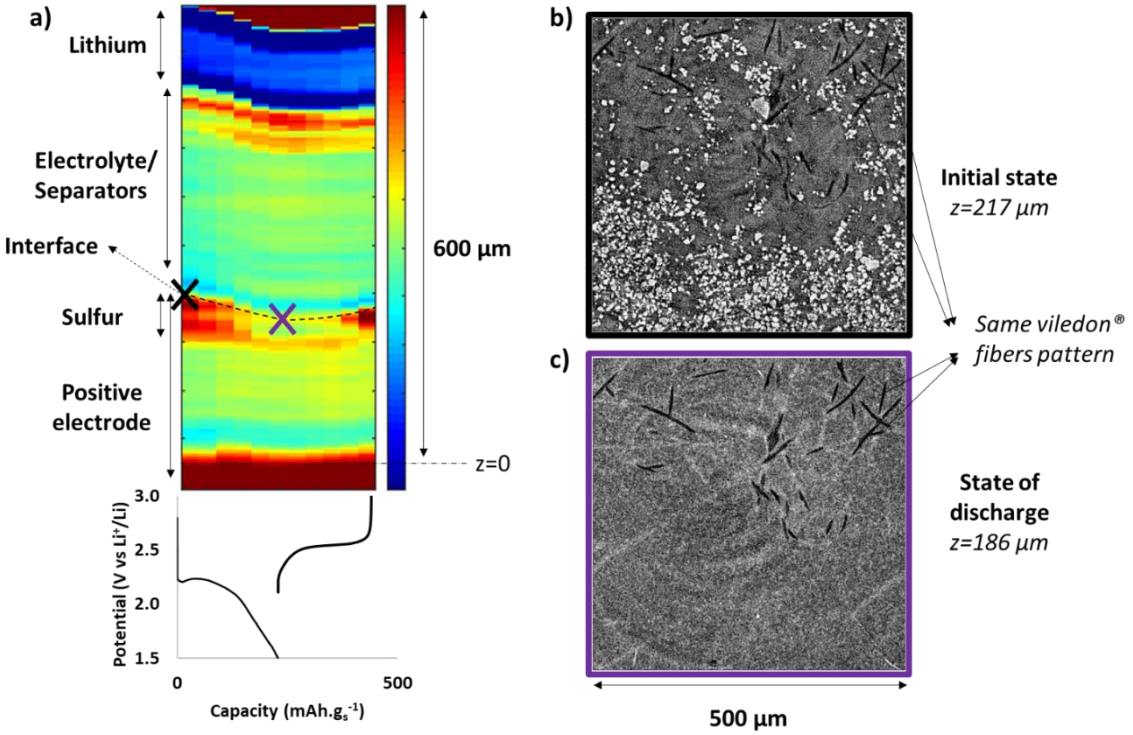

Figure 12: a) Integration over a (x,y) plane of the 3D tomographic reconstruction showing median pixel values within each vertical layer. b) Characteristic pattern of the viledon® fibers at initial state (z=217 µm). c) Same characteristic pattern of the viledon® fibers at the end of discharge (z=186 µm).

As seen in Figure 12.a, the interface between the positive electrode and the separator goes down in "z" position while discharging the cell. Consequently, the interface between metallic lithium and the electrolyte also goes down. In order to make a quantitative analysis of this evolution, a characteristic pattern, not evolving while cycling, has been found: Viledon® fibers, in black, have been identified at the initial state at a height of z=217 µm in Figure 12.b (black cross, in Figure 12.a, at the bottom of the NwC), and was taken as a reference to follow the interface evolution. The same characteristic pattern, also in black, has be found at the end of the first discharge in Figure 12.c at a height of 186 ± 1.2 µm (purple cross), meaning that this "reference" pattern goes down from 217 ± 1.2 µm to 186 ± 1.2 µm depth. It proves that there is a decrease of the positive electrode thickness of 31 ± 2.4 µm while discharging the cell. Indeed, after the sulfur consumption (only the first quasi-plateau was studied here), the CBD collapses. As sulfur, representing 80% of the dry part of the CBD, is being reduced to soluble PS, the porosity of the CBD greatly increases as it is filled by the electrolyte. Subsequently, the pressure applied on the system crushes the CBD, which has lost its mechanical strength. The CBD thickness

significantly decreases during the discharge, with a decrease of almost 70 to 80% (42 ± 1.2 to 9 ± 1.2 µm – reducing of 31 ± 2.4 µm), which is in good accordance with the porosity created by reduction and dissolution of sulfur. Indeed, the porosity of the electrode is 40% (in the CBD) and the sulfur represent 79% of the electrode volume (taking into account the density of each material). Thus 47% (79% of 60%) of the electrode volume, excluding the electrode porosity, is composed of sulfur. While discharging the cell, the porosity increases therefore to 87%, which is approximately the CBD thickness reduction obtained. The separator is therefore directly in contact with the fibers of the NwC. The NwC thickness remains almost the same and proves that this rigid carbon matrix does not evolve while cycling in this pressure range.

3.3.4.2. Distribution of sulfur in the depth of the electrode

After the first cycle, sulfur recrystallizes in the beta phase[3]. The distribution of sulfur based on peaks refinements of this phase is shown in Figure 13. This figure illustrates the sulfur redistribution during charge.

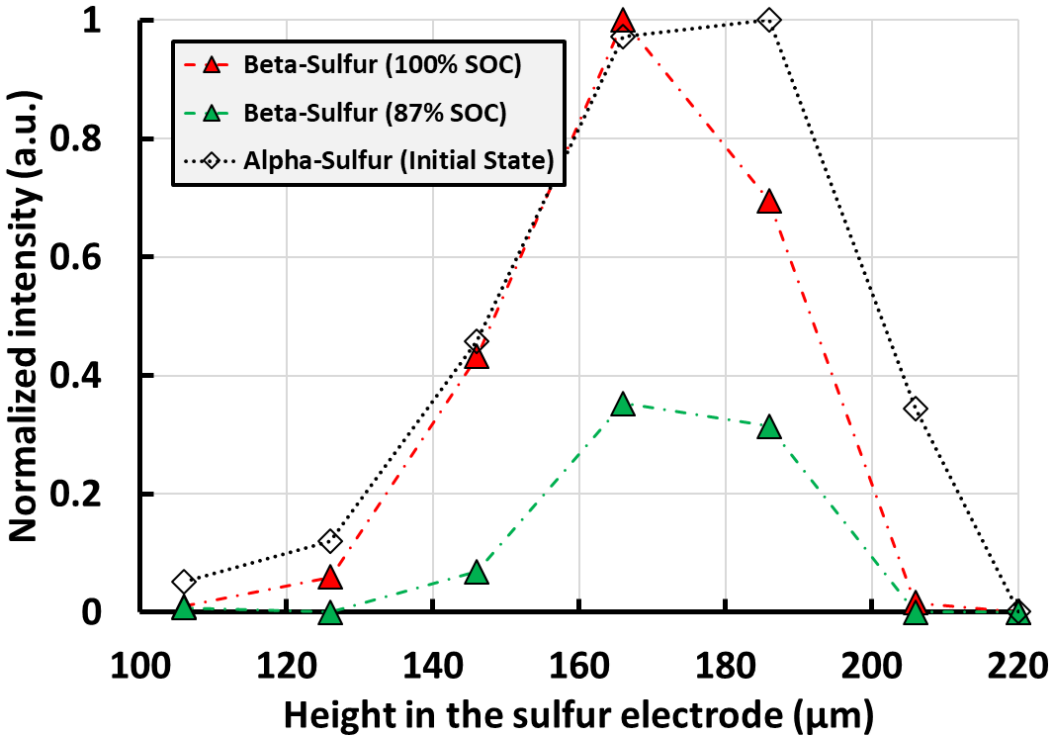

Figure 13: Evolution of sulfur quantity (integration of beta-sulfur (112) peak area in each slice) with the state of charge during 1st half charge, based on XRDCT data.

The green and red triangles correspond to the beta-sulfur quantity in the electrode depth at respectively 87 and 100% SOC. The white diamonds correspond to the distribution of alpha-sulfur in the initial state. The greatest quantity of sulfur particles is still observed in the remaining CBD layer and in the top of the NwC, where the quantity of carbon particles with high conductive surface area is maximum (between 145 µm and 185 µm height in the sulfur electrode). Below 160 µm, the amount of sulfur decreases until disappearing at 110 µm height. The distribution of sulfur within the electrode thus becomes narrower during cycling.

To conclude, this study demonstrated that the sulfur reduction is limited through the electrode thickness by the lithium ions diffusion inside the electrode from 20 µm deep, in the current experimental condition. In addition, the microstructural CBD evolution (collapse) has an impact on the distribution of sulfur while recharging the cell and could explain partially the capacity fading[10].

3.4.Dynamic processes at the negative electrode

3.4.1. Morphological evolution

The morphological evolution of the lithium metal negative electrode has also been characterized over a full discharge (‘Operando Cell’ in Figure 2/ 0.41 $mA.cm^{-2}$). It was possible to follow lithium oxidation while fully discharging a Li/S cell (black curve in Figure 2). Tomographic slices of three vertical cross-sections of the Li/S cell are shown in Figure 14.a. to Figure 14.c, illustrating the evolution of the lithium metal electrode morphology at different SOC. The lithium layer is initially homogenous in density and relatively flat. The thickness is about 120 µm in average, in good accordance with the supplier specification (135 µm). The separator soaked with liquid electrolyte is visible from 120 µm to 370 µm, while deposited sulfur on the top of the NwC is observed around 400 µm depth.

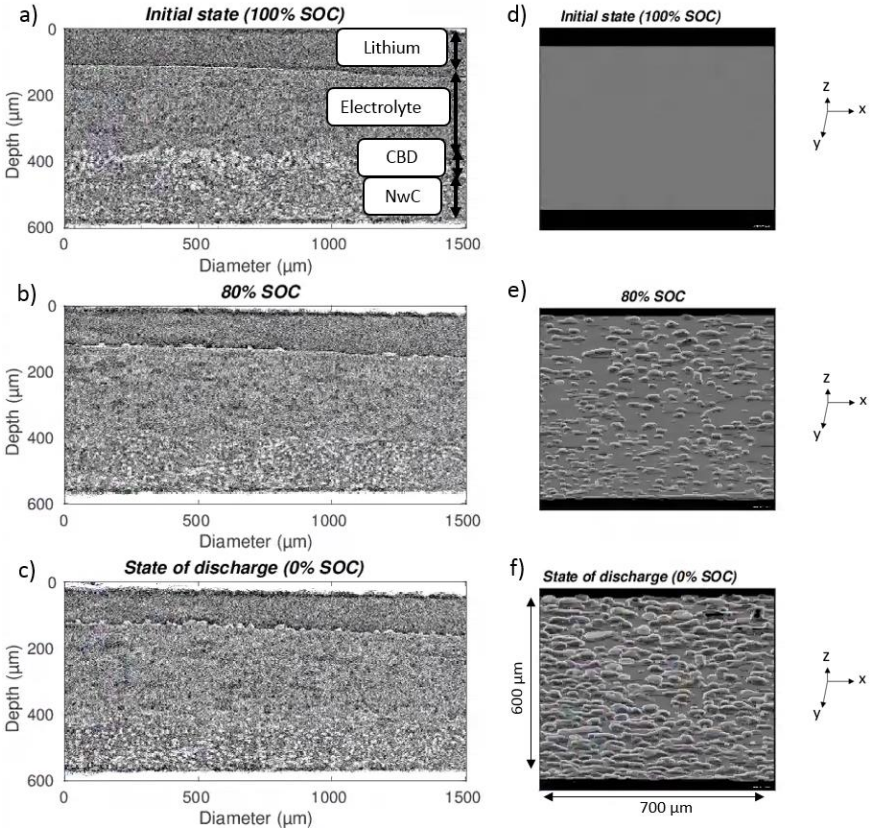

Figure 14: (a) *Vertical cross-section of Li/S cell in the initial state. (b) Vertical cross-section of Li/S cell at 80% SOC. (c) Vertical cross-section of Li/S cell at the end of the first discharge. (d-e-f) Volume representation of the pits formed along the metallic lithium surface at the initial state (d), at 80% SOC (e), and at 0% SOC (end of discharge) (f).*

A slight tilt is already present in the smooth and flat initial lithium/electrode interface at 100 SOC. At 80% SOC (~160 $mAh.g_s^{-1}$), it is possible to see the formation of pits (white regions in Figure 14.b) due to the non-uniform oxidation of the lithium, a phenomenon that has already been observed in the Li half-cell[3,11] and in other systems[12]. While further discharging the cell, two phenomena are observed: the formation of new pits and the growth of exiting pits.

In order to better understand and quantify these phenomena, the lithium/electrolyte interface was segmented slice by slice. These slices can be stacked in order to produce 3D representation (Figure 14.d to Figure 14.f). The brighter regions correspond to pits formed in the lithium layer. While the interface is smooth and flat in the initial state, several pits are created along the interface at 80% of SOC, and the heterogeneity of the electrolyte/lithium interface continues increasing while cycling and is high at the end of discharge.

3.4.2. Quantitative analysis

Roughness can be quantified (Figure 15.a), *i.e.* by calculating the arithmetical mean deviation (Ra), which represents the deviation from the absolute mean line profile. Thus, the higher the value is, the greater the average pit depth is too, independently of the total number of pits.

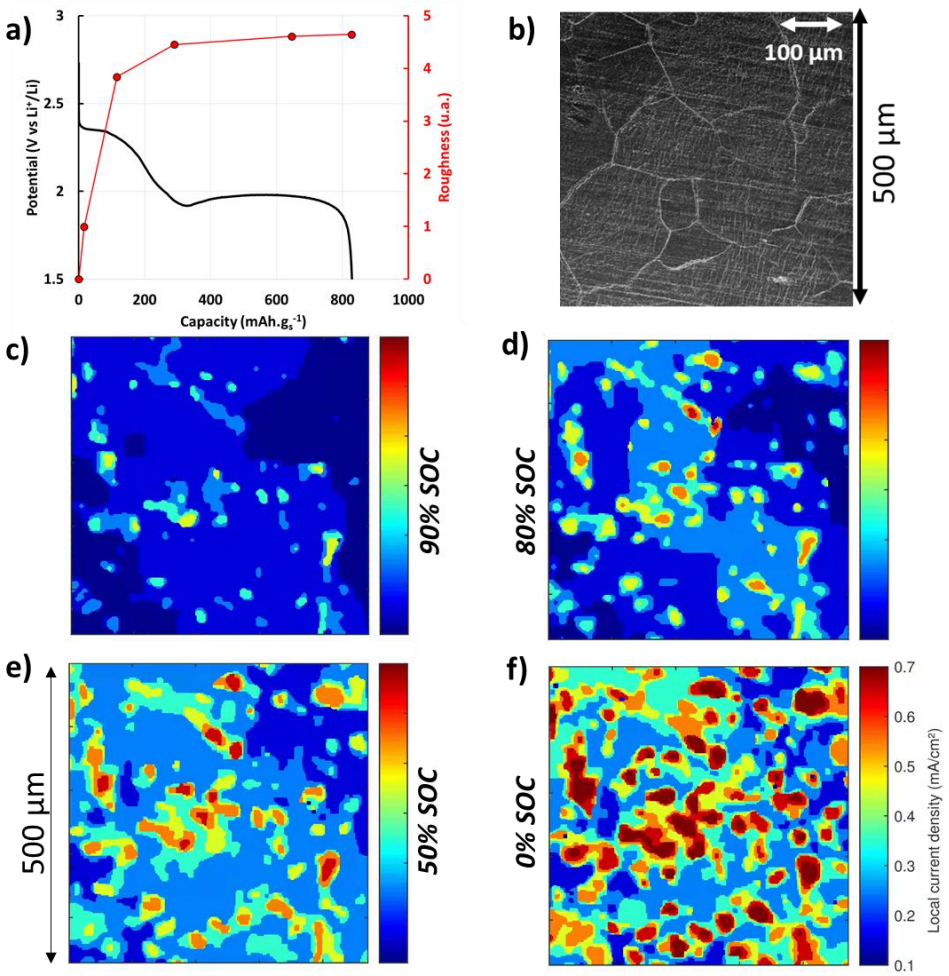

Figure 15: Evolution of roughness (red) of the lithium/electrolyte interface vs capacity. (b) SEM observation of the lithium foil microstructure. (c) Estimated local current density distribution at (c) 90% SOC. (d) 80% SOC. (e) 50%SOC. (f) 0%SOC.

There is a rapid increase of the surface roughness at the beginning of discharge, demonstrating that the oxidation of lithium is largely heterogeneous, especially at the beginning of cycling. After one-third discharge (the end of the first plateau), the increase in roughness slows down, meaning that pit depths reach a plateau, with subsequent lithium consumption proceeding through pit broadening and formation of new pits. At the end of discharge, the average thickness of the lithium electrode has decreased by about 16 µm, while a stripping of a 19 µm thick

lithium layer would be expected according to the coulometry (4.0 $mAh.cm^{-2}$) and presuming a uniform oxidation process. However, the maximum depth of the pits reaches a value of more than 30 µm, which is approximately one quarter of the initial thickness of the lithium foil. Thus, even if the average lithium layer thickness seems to evolve according to the coulometry, the lithium oxidation is highly non-uniform. To understand the origin of these heterogeneities, a map of the current density distribution can be estimated at 90%, 80% and 50% SOC and calculated at 0% SOC by considering that pit depths are proportional to the local current density in the cell, with an average oxidation thickness (19 µm) corresponding to the mean current density of 0.41 $mA.cm^{-2}$ (the current density applied to the cell). Estimations of local current densities at 90%, 80% and 50% are shown respectively from Figure 15.c to 15.e. The distribution of the local current density at 0 % SOC is shown Figure 15.f.

This map shows a very broad current density distribution with values varying from 25% to 170% of the imposed value. Interestingly, by comparing the areas of higher oxidization and higher sulfur content, it can be seen that this distribution is not linked to the initial sulfur distribution, and therefore does not seem to come from cross-talk between the two electrodes. Furthermore, the SEM image of the lithium foil microstructure (Figure 15.b) proves that the oxidization is likely to take place at the grain boundaries. Indeed, the distribution and the size of the pits at the beginning of the discharge (80% SOC) fit these boundaries. Subsequently, the pits already formed grow in diameter and new ones are created even within lithium grains.

Concerning the lithium plating, it was difficult to make quantitative analysis during the charging process due to the resolution used. However, contrary to the results obtained in the previous experiment, no large increase of lithium thickness was observed with mossy lithium plating. It proves thus that controlling the pressure enables to have a more homogeneous lithium plating while charging the cell.

Anyway, these results demonstrate a strong heterogeneity of the lithium surface reactivity, from the beginning of the stripping, independent of the sulfur electrode, probably reflecting the heterogeneity of the solid electrolyte interphase (SEI). The observation of these large variations in local current density confirms that controlling the evolution of the lithium electrode surface remains the major hurdle to be overcome in the Li/S systems.

3.5. Conclusions

To conclude, while the electrochemical profile is an average response of electrode global evolution, absorption/phase contrast and diffraction computed tomography enable to follow the evolution of electrode heterogeneities (both in terms of composition and morphology) at a local scale. The existence of a gradient of kinetics for the sulfur reduction along the electrode thickness was demonstrated, which is driven by the lithium ions diffusion. In addition, while sulfur is reduced in soluble polysulfides, a large modification of the electrode morphology was observed, with a noteworthy reduction of the CBD thickness that collapses after the first discharge plateau. This induces a redistribution of the sulfur deposits during the following charge and partially explains the loss of capacity. Even with this change, the 3D current collector is stable by keeping a rigid structure in functioning, ensuring a good conductive network and allowing better capacity while cycling than classical cells with current collector in aluminum[13]. However, controlling the architecture of the electrode to reduce the tortuosity with a mechanically stable electronic network, and optimizing the electrolyte composition, are mandatory to overcome these diffusion limitations and prevent the lack of electrochemically active surface.

As seen in the present study, despite the use of a pressure-controlled Li/S cell, the lithium behavior was still heterogeneous at the beginning of cell life already. For the first time, the local current density distribution at the lithium electrode was imaged, which has shown heterogeneous pitting of the lithium surface from the very beginning of the discharge. Clearly, these large heterogeneities favor dendrites or moss formation[14] along cycling, which is strongly detrimental for the cycle life of the cell. These heterogeneities could probably come from the non-uniformity of the native SEI in particular in the grain boundaries.

As a perspective, higher pressure, additional strategies like electrolyte additives ($LiNO_3$, sulfides)[15,16], lithium surface treatment[16] or first charge/discharge protocol would be needed to address the issue of lithium metal heterogeneous plating/striping. The cell design and characterization methodology described herein would provide an efficient tool to evaluate the newly developed solutions.

In addition, using higher resolution as well as optimizing the phase contrast could be efficient requirements to draw full 3D maps of sulfur particles throughout the electrode depth during full discharge and charge processes, in order to track both the sulfur and Li_2S consumption/formation. These points are developed in the next chapter.

References

[1] A. Senyshyn, M. J. Mühlbauer, O. Dolotko, M. Hofmann, H. Ehrenberg, *Sci. Rep.* **2015**, *5*, 18380.

[2] J. Sottmann, M. Di Michiel, H. Fjellvåg, L. Malavasi, S. Margadonna, P. Vajeeston, G. B. M. Vaughan, D. S. Wragg, *Angew. Chem. Int. Ed Engl.* **2017**, *56*, 11385.

[3] G. Tonin, G. Vaughan, R. Bouchet, F. Alloin, M. D. Michiel, L. Boutafa, J.-F. Colin, C. Barchasz, *Sci. Rep.* **2017**, *7*, 2755.

[4] X. Yin, W. Tang, I. D. Jung, K. C. Phua, S. Adams, S. W. Lee, G. W. Zheng, *Nano Energy* **2018**, *50*, 659.

[5] S. Waluś, C. Barchasz, R. Bouchet, J.-F. Martin, J.-C. Leprêtre, F. Alloin, *Electrochimica Acta* **2015**, *180*, 178.

[6] L. Zielke, T. Hutzenlaub, D. R. Wheeler, I. Manke, T. Arlt, N. Paust, R. Zengerle, S. Thiele, *Adv. Energy Mater.* **2014**, *4*, n/a.

[7] S. Waluś, C. Barchasz, R. Bouchet, J.-C. Leprêtre, J.-F. Colin, J.-F. Martin, E. Elkaïm, C. Baehtz, F. Alloin, *Adv. Energy Mater.* **2015**, *5*, n/a.

[8] S. Waluś, C. Barchasz, J.-F. Colin, J.-F. Martin, E. Elkaïm, J.-C. Leprêtre, F. Alloin, *Chem. Commun. Camb. Engl.* **2013**, *49*, 7899.

[9] "Electrochemical Systems - John Newman, Karen E. Thomas-Alyea - Google Livres,"

[10] L. Zielke, C. Barchasz, S. Waluś, F. Alloin, J.-C. Leprêtre, A. Spettl, V. Schmidt, A. Hilger, I. Manke, J. Banhart, R. Zengerle, S. Thiele, *Sci. Rep.* **2015**, *5*, 10921.

[11] O. O. Taiwo, D. P. Finegan, J. M. Paz-Garcia, D. S. Eastwood, A. J. Bodey, C. Rau, S. A. Hall, D. J. L. Brett, P. D. Lee, P. R. Shearing, *Phys. Chem. Chem. Phys.* **2017**, *19*, 22111.

[12] F. Sun, L. Zielke, H. Markötter, A. Hilger, D. Zhou, R. Moroni, R. Zengerle, S. Thiele, J. Banhart, I. Manke, *ACS Nano* **2016**, *10*, 7990.

[13] S. Walus, Accumulateur Lithium/Soufre : Développement et Compréhension Des Mécanismes Électrochimiques, PhD Thesis, **2015**.

[14] C. Brissot, *J. Electrochem. Soc.* **1999**, *146*, 4393.

[15] X.-B. Cheng, J.-Q. Huang, Q. Zhang, *J. Electrochem. Soc.* **2018**, *165*, A6058.

[16] X. Chen, T.-Z. Hou, B. Li, C. Yan, L. Zhu, C. Guan, X.-B. Cheng, H.-J. Peng, J.-Q. Huang, Q. Zhang, *Energy Storage Mater.* **2017**, DOI 10.1016/j.ensm.2017.01.003.

Table of figures

Chapter 4: *Operando* investigation of the mechanisms at the positive electrode and at the lithium/electrolyte interface analyzed with high resolution absorption tomography and XRDCT

4.1. Motivation of the work

As profound structural and morphological changes occur during the first cycle, which has been already shown in the previous chapter, but limited to only half-cycle, it is thus interesting to perform deeper characterization over a complete cycle. Indeed, the capacity of a cell is limited by the formation/consumption of Li_2S due to the incomplete utilization of active materials. Characterizing deeply the evolution of this species is thus relevant, on the whole electrode but also in the depth of the electrode, in which limiting processes have already been demonstrated for sulfur reduction.

Thanks to previous results (chapters 2 and 3), dedicated on the quantitative analysis of both sulfur and lithium electrodes, the motivation of the present work was to characterize by X-Ray Diffraction Computed Tomography (XRDCT), the Li/S system over complete cycle (from α-sulfur to Li_2S and then to β-sulfur). One of the objectives is to characterize the positive electrode at different length scales from the particle to the volumetric electrode. Indeed, thanks to the 3D spatial resolution available with this technic, the characterization of the volumetric electrode in term of morphology, possible heterogeneity and electrochemical process kinetics through the depth of the electrode is thus possible. The aim was to follow *operando* the heterogeneities of the composite electrode and to better understand the limiting factors. In addition, high resolution tomography has been performed to probe the sulfur particles individually in order to follow their evolution while cycling. The lithium metal electrode has also been characterized by absorption tomography with higher resolution than that achieved previously, allowing better insight into its evolution. The purpose was to test the impact of the current density on the lithium stripping/plating during the two first cycles.

4.2. *Operando* cell

4.2.1. Cell design

The *operando* cell design was the one developed during the previous chapter. However, a new experimental set-up has enabled to do a complete cycle thanks to the better electrical contacts (see chapter 5). As well, the use of a graphite spacer instead of stainless steel allowed to better quality of XRDCT data to be recorded. More information is available in the chapter 5. However, a short recall is given below to remember the most relevant parameters for the present chapter.

A photo of the experimental set-up and the schematic representation of the *operando* cell is shown in Figure 1.

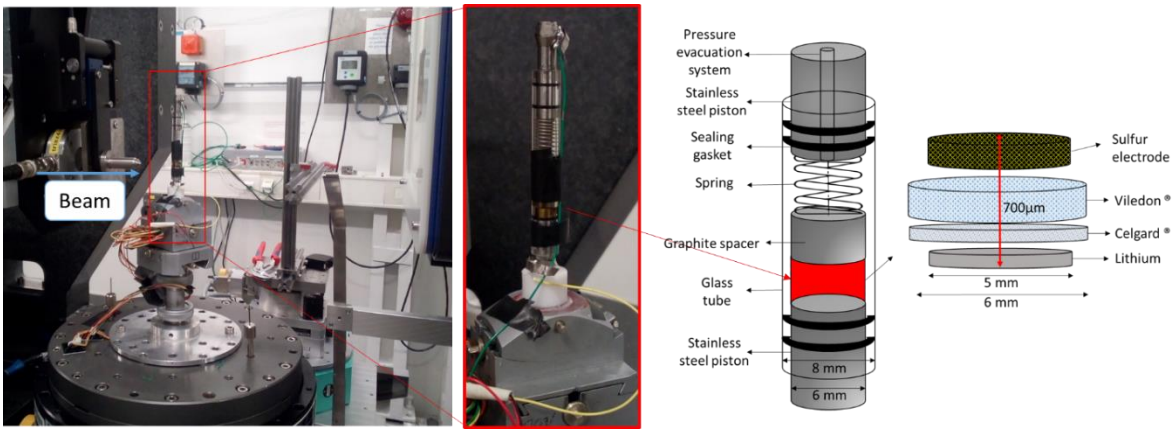

Figure 1: Photo of the experimental set-up at the ID15a (ESRF) with the associated schematic representation of the operando cell.

4.2.2. Electrochemical characterization

Two cells were characterized, with the same cell configuration, loading and electrolyte quantity. As one of the aim was to see the impact of current density on the lithium metal electrode, a similar sulfur loading, i.e. similar capacity was chosen inducing a constant lithium thickness oxidation for the different cells. The first cell was cycled at a C-rate of C/27 and the second cell at C/10 for the first cycle and C/5 for the second cycle, leading to a similar charge exchange and to more than double the current density applied for the second cell.

The use of XRDCT requires a fast rotation of the cell (60 rpm approximately) and a high and concentrated beam exposure compared to absorption tomography which has been performed with much larger beam. That is why, solely the first cycle was characterized by both XRDCT and absorption tomography. The second cell was only characterized by absorption tomography but the acquisition time was doubled for the purpose of having better statistic and so better quality tomography data. The experimental set-up is summed-up in Table 1.

	C-rate		XRDCT	Abs. Tomography		Loading (mg/cm²)	Current density (mA/cm²)	
	1st cycle	2nd cycle					1st cycle	2nd cycle
Cell 1	C/27		Yes	Yes		3.7	0.23	
Cell 2	C/10	C/5	No	Yes	Higher statistic	3.29	0.55	1.1

Table 1: Sum-up of the experimental set-up for the two characterized cells.

Cells were characterized in galvanostatic mode and the curves are shown in Figure 2.

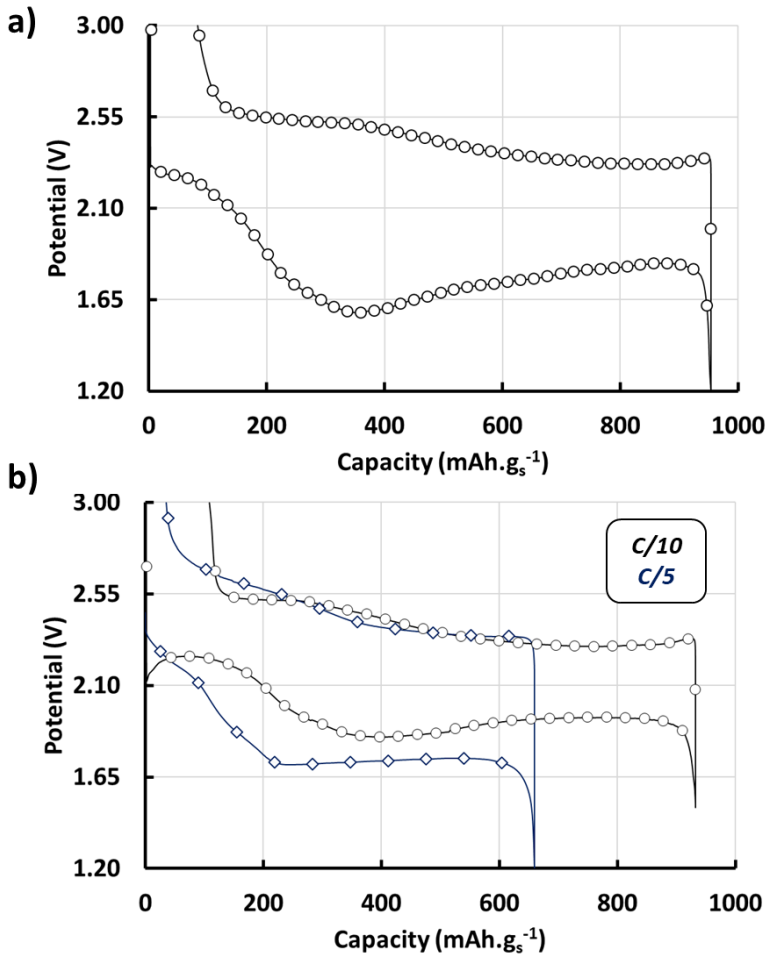

Figure 2: Galvanostatic electrochemical curves of a). the first operando cell (C/27) b). the second operando cell (C/10 then C/5).

For both cells, expected voltage profiles and capacity were obtained. For the first cell, the low voltage cut-off was fixed at 1.2V due to the polarization observed and with the intention of

having a complete cycle. High polarization was observed and could be potentially associated with the high speed rotation needed for XRDCT, as observed for previous experiment (see chapter 3). The second cell which was only characterized by tomography, exhibits a lower polarization at a given current. The low voltage cut-off for the second cycle was fixed at 1.2 V due to the larger expected polarization associated with the higher current imposed.

4.3.Mechanisms in the positive electrode

The first cell was characterized by XRDCT. To obtain a global picture, the intensity of the major peaks of sulfur species (α-S_8, Li_2S & β-S_8) were first followed by summing contributions over the whole thickness of the electrode. The intensity was normalized at 100% for the maximum of each species. The results are shown in Figure 3.

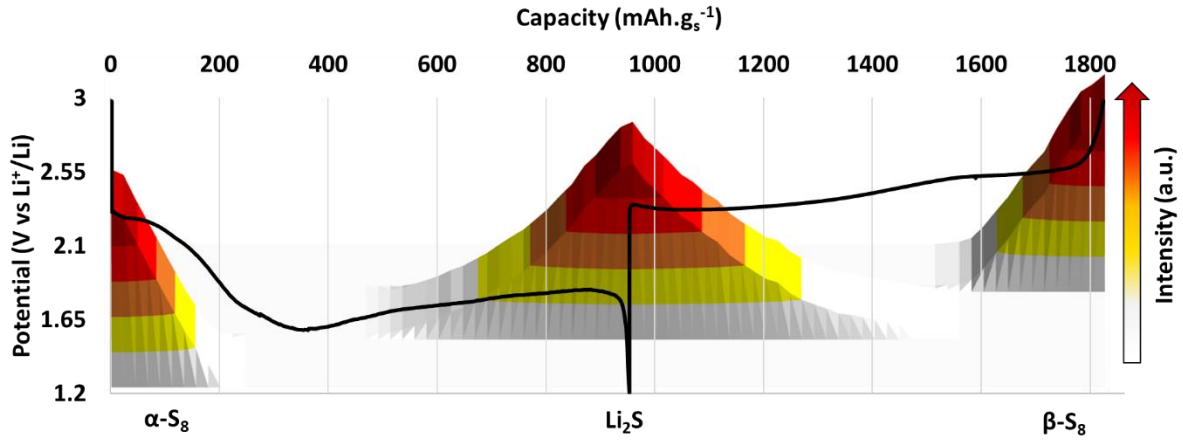

Figure 3: Evolution of the intensity of each major peaks of active species in the positive electrode normalized at 100%.

As seen before, the α-S_8 active material vanishes totally at approximately 200 mAh.g_S^{-1}, then a soluble domain is observed before the nucleation and growth of Li_2S which reaches a maximum at the end of the discharge. During the charge, the Li_2S vanishes totally before the subsequent formation of the β-S_8. There is no overlap between the Li_2S and β-S_8 existences, with a small soluble domain in between. As an expected profile and materials evolution was obtained with this electrode in this electrolyte[1], the sulfur positive electrode was then more characterized in the next section.

4.3.1. Alpha-sulfur evolution

In the same manner as the previous experiment (see methodology in chapter 3), the distribution of the sulfur phase was obtained by integrating the (222) peak area of the α-sulfur phase in each voxel of the electrode for cell 1 (Table 1). The limit between the carbon-binder domain (CBD: crust on the top of the current collector due to doctor blading process) and the top of the NwC is defined with a dash line. A representation is shown Figure 4.

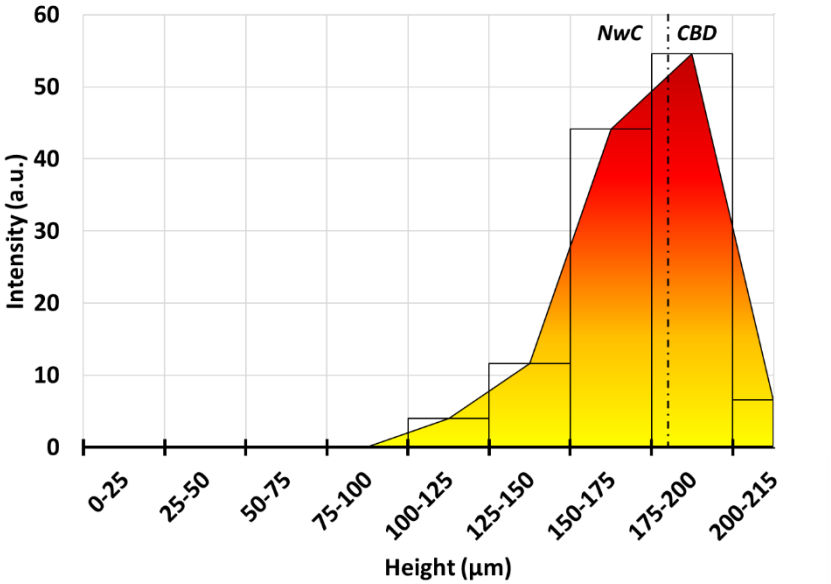

Figure 4: Initial sulfur distribution within NwC and CBD with rectangles corresponding to XRDCT resolution and color gradient used for better visualization (cell 1).

Each rectangle corresponds to the exact area probed by XRDCT within the positive electrode, with the 25 µm depth resolution, defined by the beam size. Each point in the middle of this area corresponds to the global intensity of the (222) peak. The Yellow-Red color gradient is a representation of the data and is drawn to better visualize the sulfur distribution. The "zero" is taken at the interface between the graphite spacer (Figure 1) and the bottom of the non-woven carbon (NwC) current collector.

The observed distribution is a typical bell-shaped curve due to the preparation process where most of sulfur is contained in the CBD, at the top of the current collector. More than 75% of sulfur is contained between 150 and 200 µm, at the top of the current collector. The absorption tomography, thanks to higher resolution (0.717 µm/pixels) shows a sulfur distribution over 119 µm and a penetration of exactly 87 µm into the NwC, by looking at tomograms taken at

different depths in the electrode. This is slightly higher than in the previous experiment (110 µm in total and 68 µm depth into the NwC). This is probably due to the lower ink viscosity, leading to higher sulfur penetration and thinner CBD layer when preparing the electrodes with a lower loading (3.7 compared to 5.1 $mg.cm^{-2}$, in the previous study).

The (222) peak was integrated from each voxel in the central parts of the cell (cell 1) defined by a rectangle of 10x10 voxels (3 mm x 3 mm) along the entire electrode thickness, and was followed while cycling (Figure 5). The points after 200 $mAh.g_S^{-1}$ have been extrapolated and represented by a black dash lines. Indeed, when the sulfur quantity is very low, the errors made on the peak area calculation is not negligeable, so that the quantity of sulfur present cannot relaibly be determined by this method.

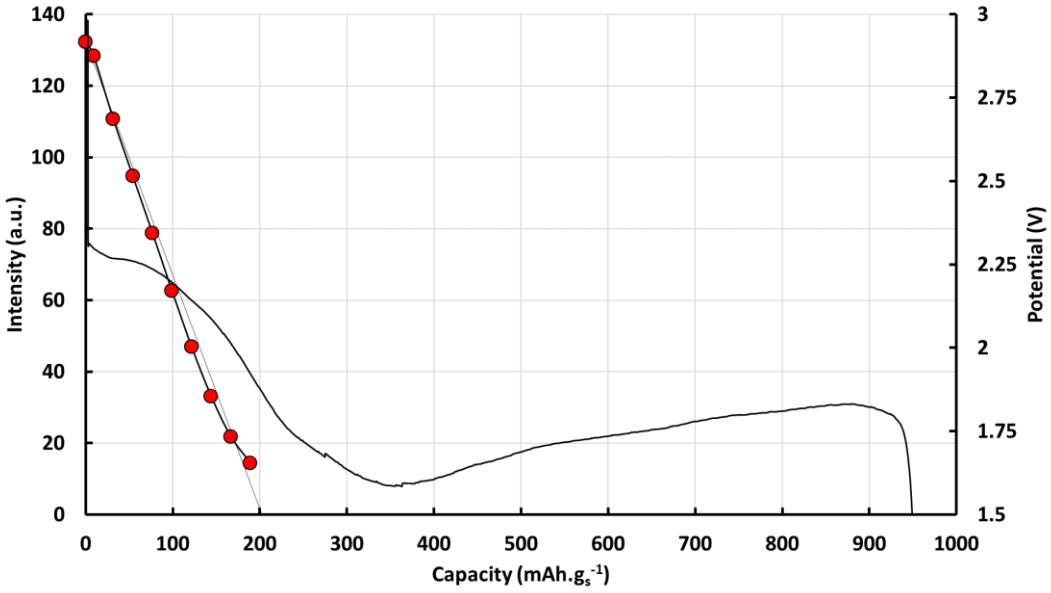

Figure 5: Evolution of sulfur quantity in the entire electrode thickness from XRDCT data (cell 1). (222) S_8 peak area on a 2 mm x 2 mm electrode region.

As already demonstrated, a linear decrease of sulfur while cycling (see chapters 2 and 3) with a complete disapearance of the sulfur at 200-205 $mAh.g_S^{-1}$ is observed and can be associated with the unique reaction $S_8 + 2e^- \rightarrow S_8^{2-}$ [2–4].

In order to be more precise in the sulfur distibution, the high resolution, high statistic absorption tomography on cell 2 (Table 1) allowed the extraction of all the voxels related to sulfur particles in the whole thickness of the electrode (from the CBD to the NwC), not feasible in the experiments described in the previous chapter (chapter 3). An automatic segmentation between the carbon fibers (from the NwC) and the sulfur particles is nevertheless still difficult to

perform, even with these improvments. However, thanks to the application of both automatic and manual filters, the segmentation of sulfur particles through the whole electrode thickness at the initial state could be accomplished and the distribution is shown Figure 6.

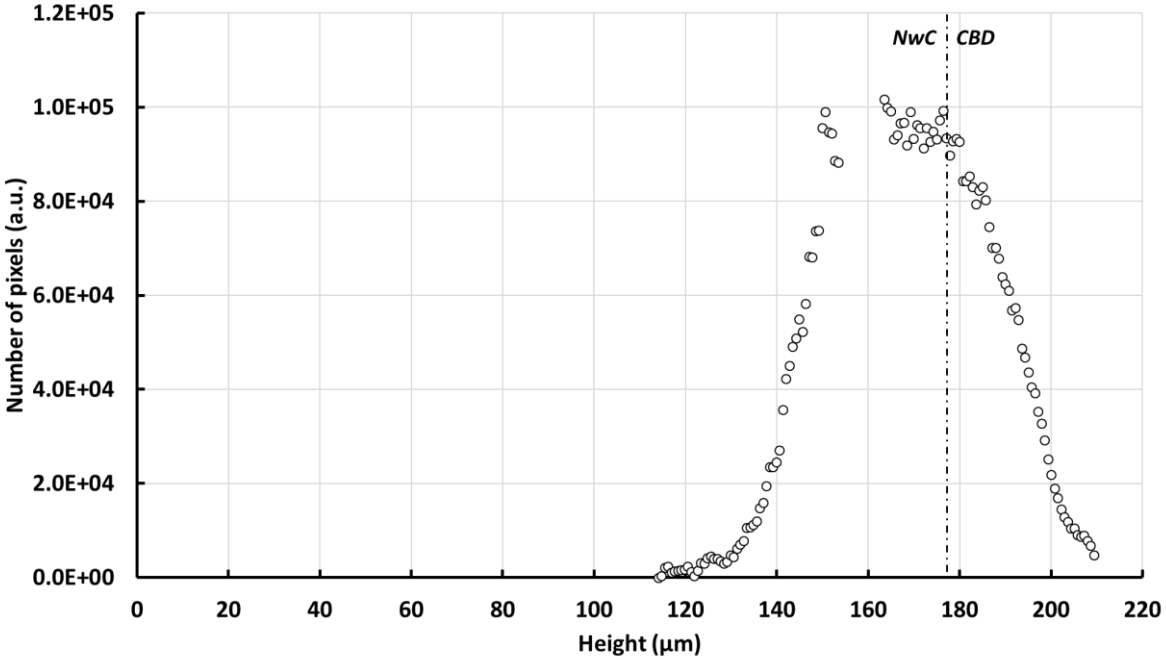

Figure 6: Sulfur distribution obtained from absorption tomography data (from cell 2).

Sulfur distribution is similar to the one obtained in cell 1 thanks to XRDCT. A large amount of sulfur is contained in the coating on the top of the current collector. The sulfur penetrates about 60 µm into the NwC and forms a CBD of 30 µm with a total thickness approximately equal to 215 µm. However, a constant number of pixel is observed from 160 to 180 µm, in which the sulfur content is maximum. This zone is composed with both the CBD and the top of the NwC where most of the coating is present. Indeed, the NwC plays the role of filter paper for the ink with a porosity of about ten micrometers, limiting the sulfur particle penetration into the depth of the NwC which explains the sulfur concentration at the top of the NwC. Concerning the CBD crust, the large size of the sulfur particles (as discussed in the previous chapter) limits the quantity of sulfur on the first micrometers of the electrode (use of a doctor blade). A same image process has been tried at different states of discharge but without success. Indeed, the filters used are not as relevant, when the amount of sulfur is low, as for the initial state. That is why, solely the distribution at the initial state has been shown thanks to absorption tomography. However, due to the high resolution and the high statistics used while recording the absorption tomography of the second cell, it was possible to extend the analysis to characterize particle by

particle the sulfur electrode. Sulfur particles were identified, within different sub-volumes and their evolution was followed during cycling. A schematic representation of the segmented sulfur particles in a 200x140x240 µm^3 box at different states of charge is shown in Figure 7.

.

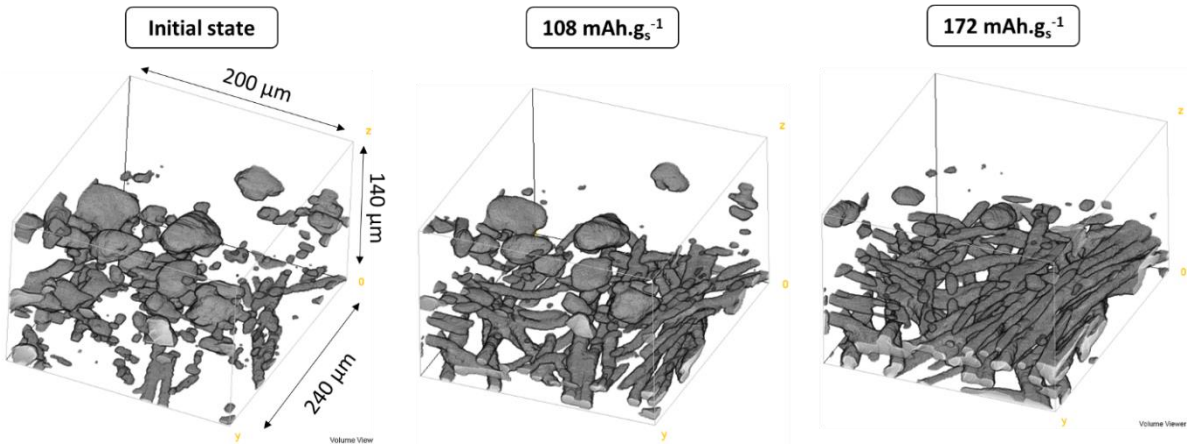

Figure 7: Boxes representing the segmented sulfur particles and NwC fibers at different states of charge (from the cell 2).

In the initial state, different particle sizes are visible, with large (40 µm in diameter) and relative smaller (less than 10 µm in diameter) objects. As discussed previously, most of the large particles are contained in the CBD. At 108 mAh.g$_S^{-1}$, the smallest particles have disappeared and only the biggest remain. At 172 mAh.g$_S^{-1}$, only a small number of the largest initial particles remains. This can be explained by the fact that, in terms of coulometry, the smallest particles size requires less charge to be fully oxidized with respect to the bigger ones. The NwC fibers become gradually more visible within the fixed volumes while discharging the cell. This is due to the CBD collapsing but also to the lithium layer thickness diminishing during its oxidation, inducing a global downward movement of the positive electrode.

In order to make a quantitative analysis of particle sizes, it is necessary to segment individual particles sharing no voxel with other but it was thus difficult to identify a perfectly isolated particle. Nonetheless, some particles have been identified to be totally isolated and characterized in terms of volume, *i.e.* the number of voxels within the particle *vs* the discharge capacity. This has been carried out on three particles, of more than 35 µm in diameter, taken at different heights in the positive electrode (from the CBD in red, at the top of the NwC in black and in the bulk of the NwC in blue). The volume variation while cycling and a schematic

representation of the particle positions in the electrode are shown in Figure 8, with the same color panel used for both figures.

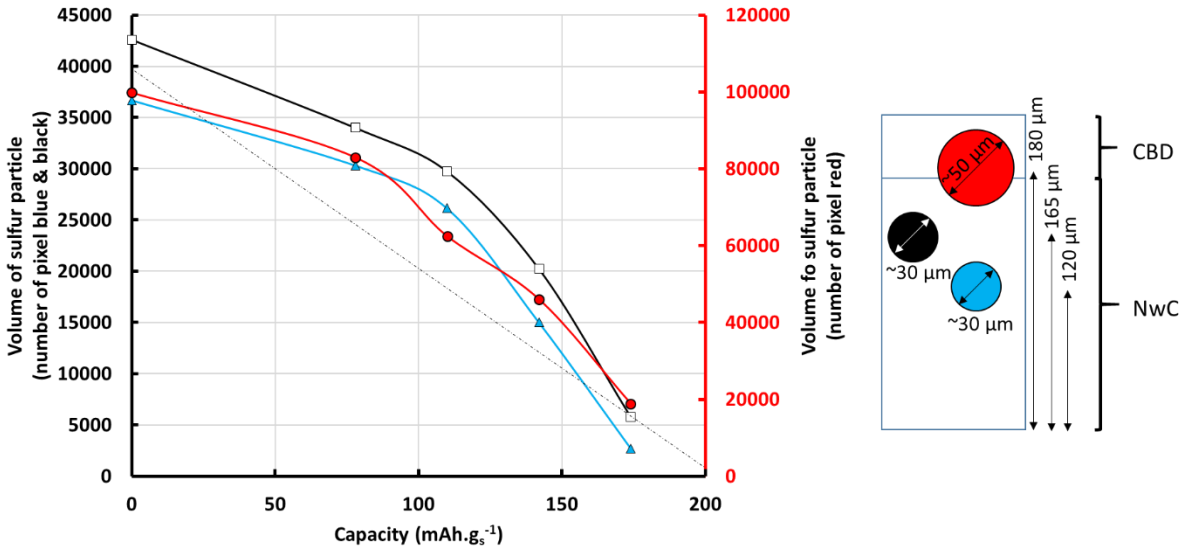

Figure 8: Evolution of particle volume versus capacity and schematic representation of the depth of each particle in the electrode. Two y axis are used for better visualization. The red curve is associated with the red axis.

The evolution of volume, *i.e.* voxels contained in one particle, seems to be similar for particles at different depths in the electrode. However, the loading of this electrode is lower and there is no polarization on this cell which could explain that the lithium ion diffusion less impacts the electrochemistry.

However, the analysis has been done on solely a small number of large particles, not necessarily characteristic of the whole distribution, although it can be assumed that by considering particles of similar volumes, the effect of volume/surface ratio is constant. The sulfur consumption kinetic of these large particles increases near 100 mAh.g$_s^{-1}$. Indeed, as the quantity of sulfur being reduced is linearly proportional to the number of electrons exchanged in the cell in accordance with only one electrochemical reaction, when the smallest sulfur particles have totally disappeared, as seen in Figure 8, the speed of larger particles consumption may be increased while applying the same current.

Furthermore, when the particles are isolated, it is possible to draw a box around the particle in order to see their dimensions in a rectangle box (X,Y,Z) and follow the evolution while cycling. In that sense, the mass center of the particle (XM,YM,ZM) could also be followed while cycling (Figure 9).

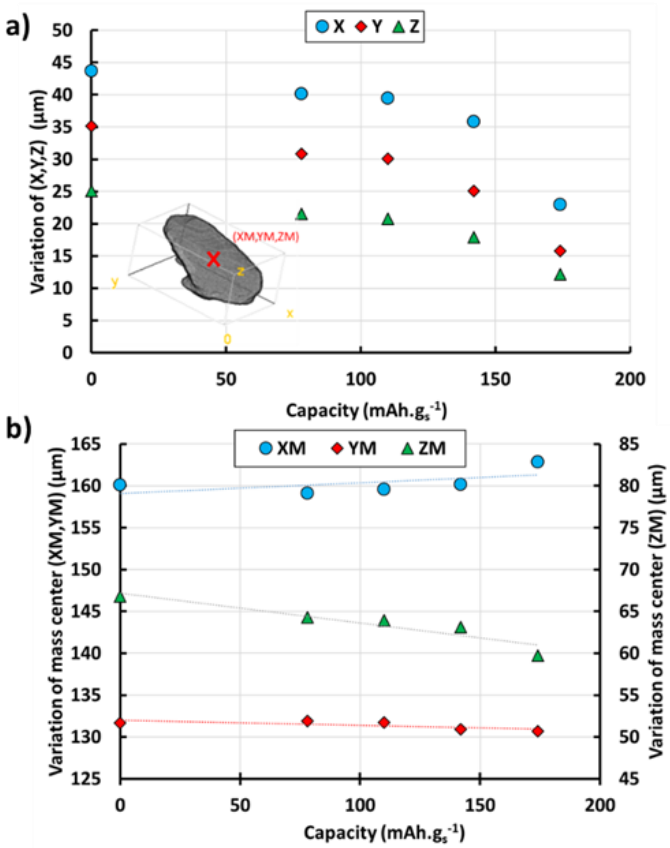

Figure 9: a) Evolution of the dimensions (X,Y,Z) of one particle and b)evolution of the mass center (XM,YM,ZM) while cycling with a schematic representation of the particle box.

The evolution with time of the (X,Y,Z) is similar from the 3 dimensions of space. It means that the particle volume is reduced homogenously from each side. The mass center does not evolve at all in the (x,y) plane with a relative small variation of XM and YM (respectively blue and red in Figure 9.a). However, the particle moves downward, as shown with the decrease of the ZM value (green in Figure 9.b). This is due to the reduction of the lithium thickness which finally makes the positive electrode going down while cycling and also due to the CBD collapsing.

4.3.2. Li_2S evolution

Similar to the analysis of sulfur peaks, the most intense (111) reflection of Li_2S was integrated through the electrode thickness and in the same center of the cell defined by a 10x10 voxels rectangle (2 mm x 2 mm). The distribution of the peak area at the end of the first discharge is shown in Figure 10.

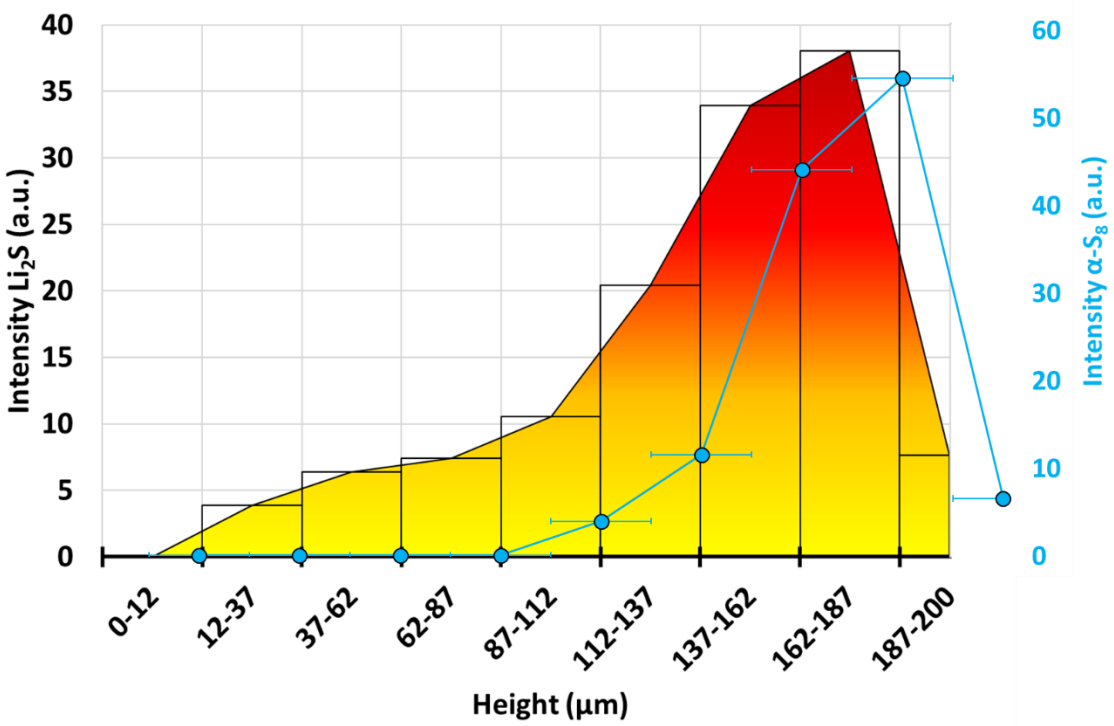

Figure 10: Li_2S distribution at the end of discharge from XRDCT data (from cell 1) with the α-S_8 distribution in blue.

At the discharge state, the total height of the electrode is 200 µm thanks to XRDCT measurement based on the detection of Li_2S, which is 15 µm less than the initial thickness of the positive electrode. However, the CBD thickness reduction is measured by looking at different tomograms in the depth of the electrode (CBD is the part of the electrode without viledon® and NwC fibers) as in the previous experiment and is equal to 25 µm (78% of the thickness loss compared to 32 µm initial), which is in good accordance with the total electrode porosity taking into account the porosity created by the reduction of sulfur (87%, see chapter 3). However, the active Li_2S species have precipitated in the new intermingled electrode & Viledon® region, leading finally to an electrode thickness reduction of only 15 µm. This is a consequence of the CBD collapsing, as already discussed in the previous chapter. Li_2S can be observed in all the thickness of the electrode, whereas the higher concentration of Li_2S is observed, as for sulfur, in the top of the electrode where the carbon surface area is the highest (from 137 to 200 µm) due to the presence of carbon black. However, Li_2S precipitates deeper in the electrode compared to the initial sulfur distribution (Figure 10).

Different reasons could be given to explain this phenomenon.

- The lithium ions transport through the electrolyte is relatively low[5], meaning that there is a lithium ions concentration gradient along the separator and the 3-D current collector.
- Upon discharge, the lithium ions are less concentrated in the positive electrode due to their consumption with the formation of reduced polysulfide species[5].
- The anionic species S_4^{2-} & S_2^{2-}, produced electrochemically in the cathode, migrate under the electric field. Indeed, during the discharge, the anionic PS migration flux is orientated from the positive to the negative electrode. However, the PS diffusion process should homogenize their concentration in the volume of the electrode and thus expand the distribution of PS and therefore the distribution of Li_2S.
- The insulating Li_2S specie forms a nanometric layer that passivates the carbon surface, a large surface area is thus needed to complete the reaction.

To go deeper in the Li_2S formation mechanism, the Li_2S dynamic processes during formation and consumption have been characterized. First, the global evolution has been followed by summing all the Li_2S contribution from the (111) peaks at each state of charge. This evolution is shown in Figure 11.

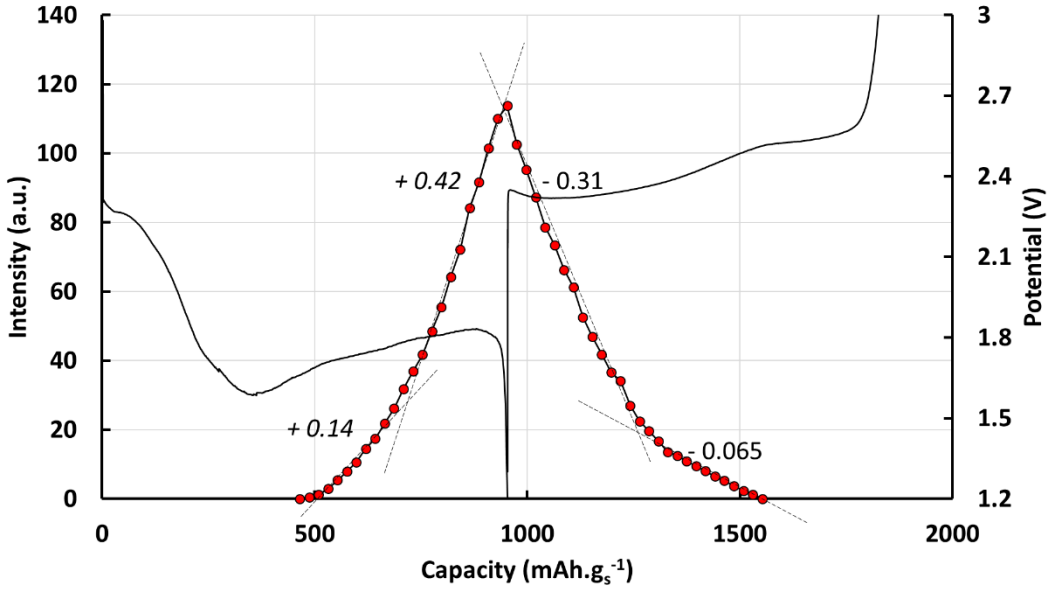

Figure 11: Evolution of Li_2S quantity during the first cycle, in the electrode from XRDCT data of (111) peaks (from cell 1).

The evolution of Li_2S formation/consumption is different than that obtained by *Walus et al.*[3]. They proposed two steps mechanism for Li_2S formation, with a first one forming only Li_2S, and a second forming both Li_2S and Li_2S_2 phases simultaneously. Here, two regimes seem to be observed for Li_2S formation, but in an opposite behavior, the lowest slope is obtained at the beginning of the second plateau, between 460 and 750 $mAh.g_s^{-1}$. Most of the Li_2S formation, (after 750 $mAh.g_s^{-1}$), is obtained with an intermediate slope compared to Walus *et al.* work[1,3], indicating the simultaneous formation of both Li_2S and Li_2S_2 phases during all the processes. It could be coherent with the high polarization observed on the second plateau and the long tail obtained near 500 $mAh.g_s^{-1}$ associated with the germination and nucleation of Li_2S proposed in literature[6,7]. Some calculations and further details of the proposed mechanism are discussed at the end of this paragraph. The charge is coherent with the previous results obtained by Walus *et al.*[3], with a two-step disappearance of Li_2S with a favorable oxidation process during the first two third of charge. The second step is probably associated with the oxidation of S_4^{2-} in long-chain polysulfides in parallel of the oxidation of both Li_2S and Li_2S_2 phases, but with faster kinetic reaction.

XRDCT data allowed to have both temporal and spatial resolutions in the 3 dimensions of space. It has been used to analyze the Li_2S evolution through the electrode, with a resolution defined by the beam size (25 µm) in order to see the possible heterogeneities within the composite positive electrode while cycling. Figure 12 shows the evolution of 4 “layers” from 87 to 187 µm and representing the layers containing most of the Li_2S discharge product. The layers from 87 to 137 µm are in the bulk (in the NwC) of the electrode, whereas the area from 137 to 187 µm corresponds to the top of the current collector (see Li_2S distribution in Figure 10).

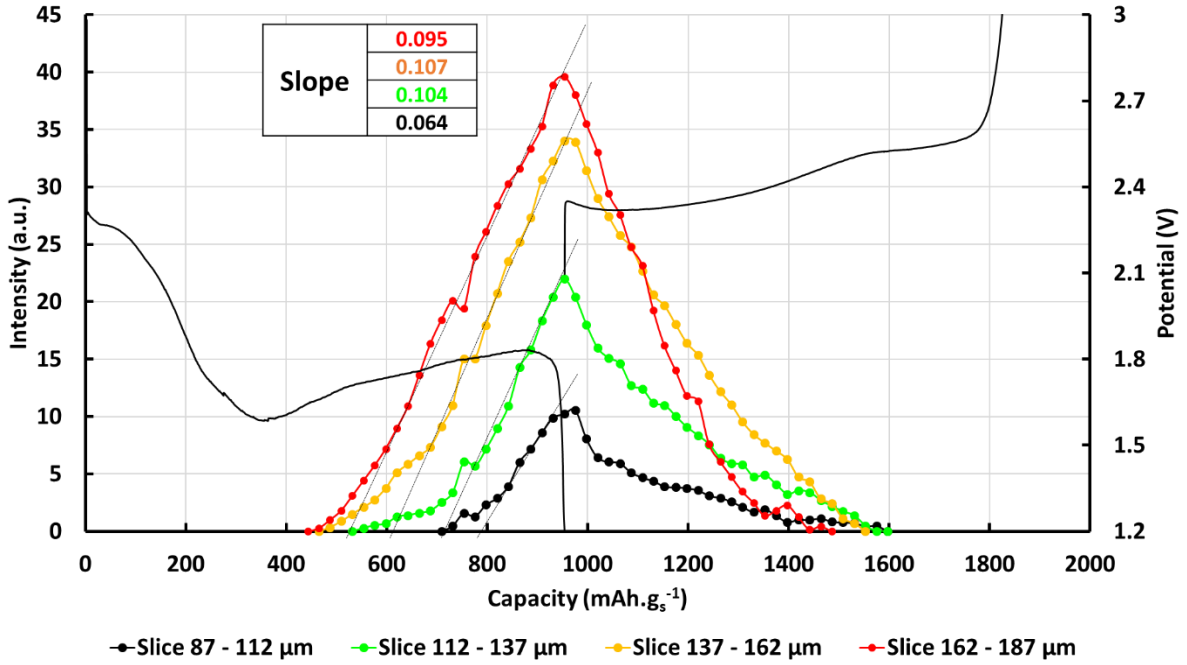

Figure 12: Evolution of Li_2S quantity determined by the Li_2S (111) peak area through the depth of the electrode during the first cycle based on XRDCT data (from cell 1).

Discharge:

During the discharge, all layers seem to evolve in the same manner. There is a long tail with a small slope, when the formation of Li_2S begins. Then a linear evolution of Li_2S formation *vs* the capacity is observed with near the same slope whatever the depth. This linear evolution with the same slope indicates that the same electrochemical mechanism occurs upon the discharge process and the electrode thickness. However, there is a shift in time of the appearance of Li_2S with respect to that expected assuming a linear profile of Li_2S formation and extrapolating the trend. The time shift is approximately 90 mAh.g$_S^{-1}$, i.e. 66 µAh, each with 25 µm shift in the depth of the electrode. One hypothesis, is that the electric potential is not perfectly uniform through the depth of the electrode with a polarization increasing from the electrode/electrolyte interface to the electrode/collector interface. This variation of polarization may favor the formation of short PS in the bulk of the electrode instead of producing Li_2S. Another possible explanation is that this shift may be associated with lithium ions diffusion in the depth of the electrode, explaining the delay of Li_2S formation deeper in the electrode. Indeed, the lithium ion transport through the electrolyte is relatively low[5], meaning that a Li^+ concentration gradient along the separator and the 3D current collector can occur. The lithium ions are less concentrated in the bulk of the positive electrode compared to the electrode surface.

It is thus possible to estimate a diffusion coefficient (D) by:

$$D = \frac{l^2}{6\,t}$$

Where "l" is the thickness of a layer (25 µm), and "t" is the time between the appearance of Li_2S (1h30, *i.e.* 90mAh.g_s^{-1}). The diffusion coefficient is thus given by:

$$D = \frac{(25 * 10^{-4})^2}{6 * 5400} = 0.2.10^{-9}$$

The obtained diffusion coefficient of $0.2.10^{-9}$ $cm^2.s^{-1}$ is a relatively low value compared to the one determined in ether based electrolytes with anions concentration of 1mol.L^{-1}, *i.e. 0.9.*10^{-8} $cm^2.s^{-1}$[5], but a reasonable first estimation. Indeed, the electrode is a more tortuous medium than a porous separator. In addition, the electrolyte used in this study is viscous due to the high polysulfides concentration at this stage of discharge. Furthermore, *Dominko et al.*[8] reported a diffusion coefficient of PS 0.1M in a ether based electrolyte of $3.8.10^{-9}$ $cm^2.s^{-1}$ which is not so far from the obtained diffusion value. The three layers, containing most of the Li_2S quantity, have similar Li_2S formation slopes far from the expected one supposing the reaction S_4^{2-} + 8 Li^+ + $6e^-$ → 4 Li_2S. This means an equivalent reduction process for all layers, even if shifted in time as a function of the electrode depth, as previously said.

In conclusion, a proposed mechanism is that the lithium ions diffusion through the electrode thickness drives the nucleation and formation of the Li_2S in competition with the formation of less reduced species. Therefore, when the nucleation process of Li_2S starts, Li_2S is produced with the same selectivity for each layer probed in the 100 µm depth of the electrode. An equivalent approach was taken to treat the layers from 0 to 87 µm and a similar tendency was observed. However, no quantitative analysis was carried out on these layers due to the low amount of Li_2S present.

Charge:

During the charge, the kinetics depends of the electrode depth. The closer the layer to the electrolyte is, the quicker the disappearance Li_2S is. Indeed, the layer at the top of the current

collector (in red) reacts preferentially compared to the other ones. The kinetics, associated with the consumption of Li_2S, decreases gradually going deeper into the bulk of the electrode. Except for the top of the electrode, Li_2S disappears completely at approximately the same capacity (from 1550 to 1590 $mAh.g_s^{-1}$) for all the electrode depth, just before the potential jump and the formation of beta-sulfur. This can be related to the isolating character of Li_2S, which limits its reactivity compared to more oxidized PS, in accordance with literature[9]. The highest kinetics observed for the top of the electrode may be associated with the large electronic surface area more efficient to induce the oxidation of isolating compounds and possible chemical reactions between Li_2S and oxidized PS.

4.3.3. Beta-sulfur evolution

In the same way as for the α-sulfur and Li_2S evolutions, it was possible to follow the quantity of β-sulfur by following the intensity of the (140) peak at different depths during cycling, as shown in Figure 13.

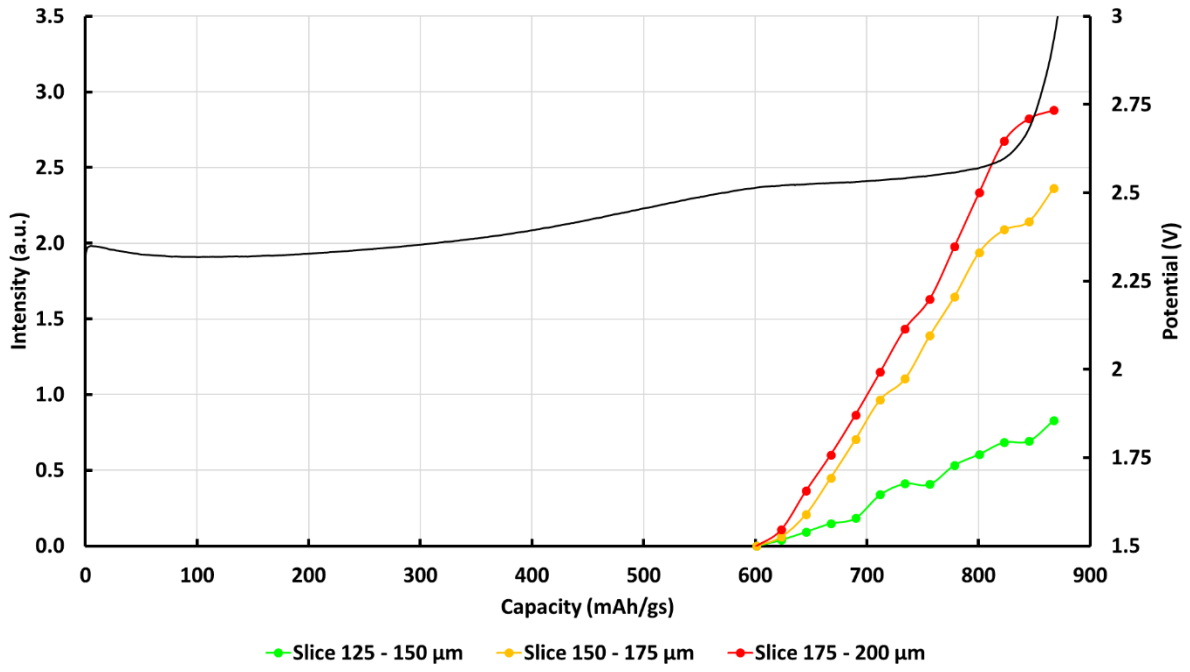

Figure 13: Evolution of β-sulfur quantity as determined by the β-sulfur (140) peak area through the depth of the electrode during the first charge based on XRDCT data (from cell 1).

Contrary to Li_2S, the β-sulfur formation is homogeneous in the different layers and starts near 500 $mAh.g_s^{-1}$.

Active material distributions in the positive electrode at initial state (α-S_8), state of discharge (Li_2S) and state of charge (β-S_8) are shown in Figure 14.

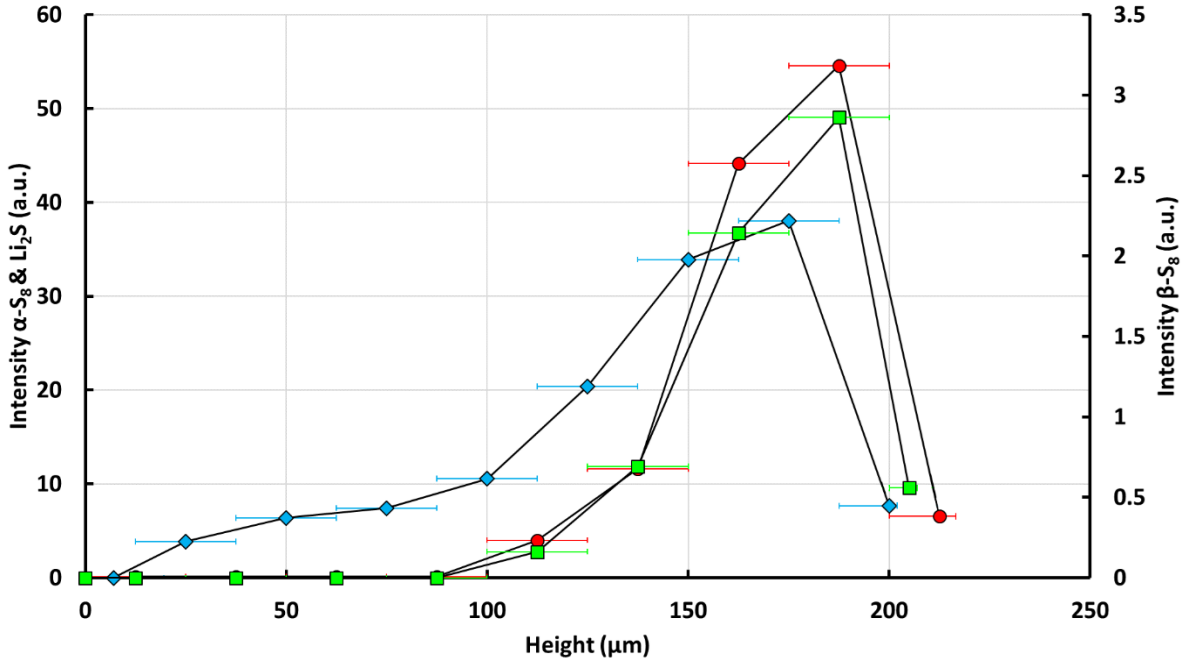

Figure 14: Comparison of the active materials distributions in the positive electrode (α-S_8 (red), Li_2S (blue), β-S_8 (green)) taken at different states of charge (initial state, end of first discharge, end of first charge respectively).

The distribution of β-sulfur is similar to the initial sulfur distribution. Most of sulfur is concentrated on the top of the current collector, where most of the conductive electroactive surface is available thanks to carbon black, even after the collapsing of the CBD layer (chapter 3). The NwC 3D rigid matrix seems to be a solution in term of electrode morphology stability, even if the thickness of the NwC 3D electrode is not favorable for diffusion process and volumetric capacity.

β-sulfur was also monitored by absorption tomography (thanks to cell 2). However, it was not possible to segment correctly the sulfur particles from the NwC fibers and carbon domain, even with the high resolution and high statistics used. Tomograms, taken at different depths in the electrode at the end of the first charge, are shown in Figure 15.

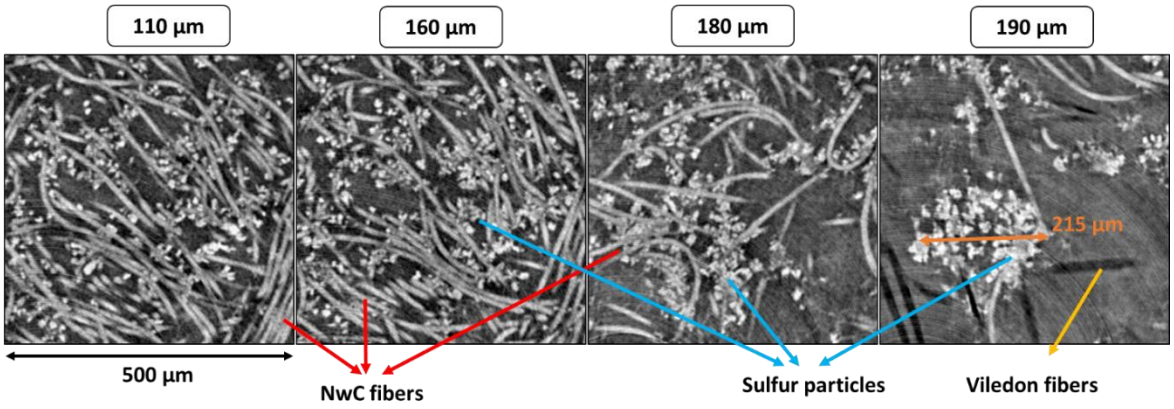

Figure 15: Tomograms in the (x,y) plan of the cell 2, at the end of the first charge at different heights in the electrode (110, 160, 180 and 190 µm from the bottom of the NwC).

The β-sulfur crystallizes in large agglomerates (215 µm) at the surface of the electrode and globally with smaller particles size (10-20 µm in diameter) than the initial α-sulfur (~ 40 µm). The smaller particles size is due to electrochemical nucleation and growth of β-S_8[2,10], which is driven by the surface to volume ratio, with a particles size likely limited by the electronic conductivity of sulfur.

Same image positions as those drawn in Figure 15, were chosen at the end of the second charge, done at a C-rate of C/5 and are drawn in Figure 16.

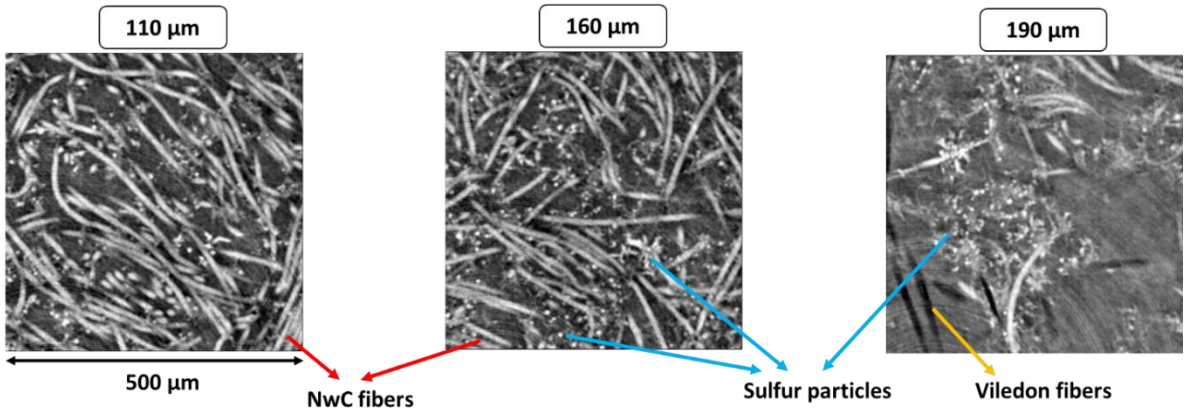

Figure 16: Tomograms in the (x,y) plan of the cell 2, at the end of the second charge (C/5) at different heights in the electrode (110, 160 and 190 µm from the bottom of the NwC).

There is still agglomerates at near the surface of the electrode but less dense. In addition, the amount of sulfur seems to be largely reduced with also smaller particle sizes. It proves that the active material utilization diminishes while cycling and the increase of the current density (C/5

instead of C/10) leads to smaller particles size, meaning that the possible limitation step is the growth of particles instead of nucleation.

4.3.4. Global evolution

It is possible to sum up the evolution of the active materials in the positive electrode looking at each component formation/consumption kinetics (Figure 17).

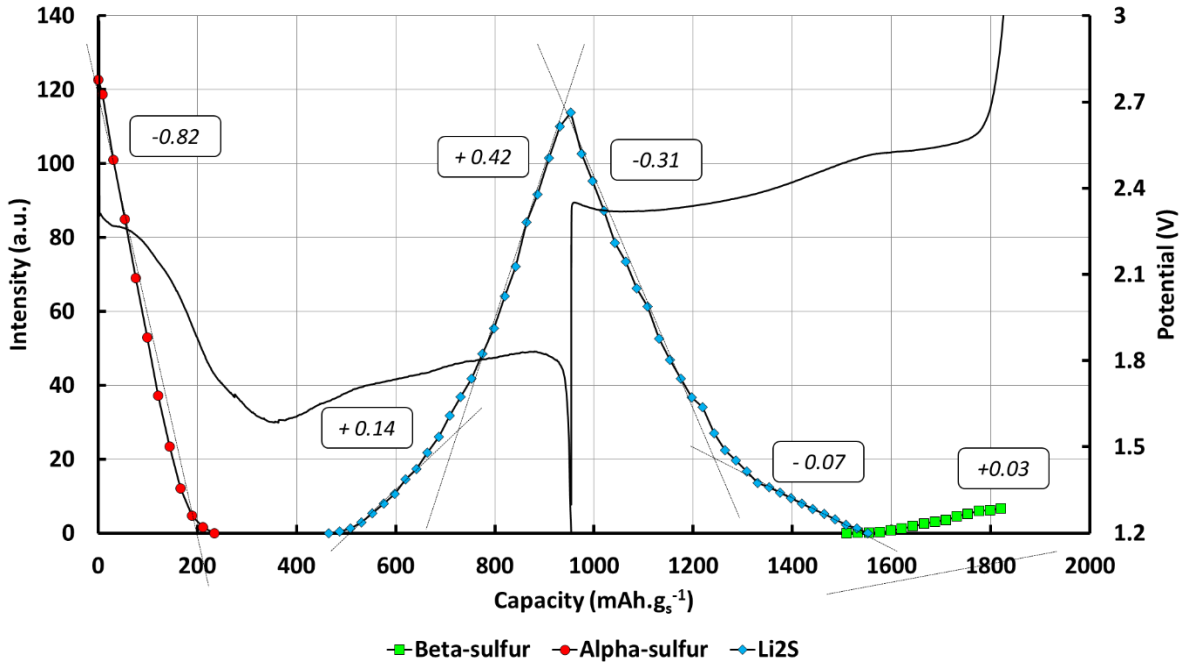

Figure 17: Global evolution of the active species in the first cycle, as derived from XRDCT data.

It is possible to quantitatively analyze the global evolution by calculating how many Li_2S quantity is produced with respect to the consumption of S_8 per mole of electrons. This work is largely based on the work of S. Walus [1].

Different assumptions were made with the aim to obtain an estimation and a tendency of the mechanism:

The ratio (labelled "γ") between peak areas of (222) S_8 and (111) Li_2S has been experimentally defined by S. Walus[1] to be 1.13. Two slopes were defined for the formation of Li_2S, the first one equal to 0.14 and the second to 0.42. The relation between the slopes of S_8 consumption and Li_2S formation (α_1 & α_2) is given by:

$$\alpha_1 = \frac{S_8\ consumption}{Li_2S\ formation} = \frac{Slope\ S_8\ consumption}{Slope\ Li_2S\ formation} * \gamma = \frac{0.82}{0.14} * 1.13 = 6.6$$

$$\alpha_2 = \frac{S_8\ consumption}{Li_2S\ formation} = \frac{Slope\ S_8\ consumption}{Slope\ Li_2S\ formation} * \gamma = \frac{0.82}{0.42} * 1.13 = 2.21$$

Calculations could be done in term of the amount of electrons exchanged, taking into account the following reaction where 2 moles of electrons are exchanged per mole of sulfur:

$$S_8 + 2e^- \rightarrow S_8^{2-}$$

The equations thus become:

$$\alpha_1 = \frac{S_8\ consumption}{Li_2S\ formation} = \frac{1\ mole\ per\ 2\ e^-}{x_{mole} Li_2S\ per\ e^-} = 6.6$$

$$\alpha_2 = \frac{S_8\ consumption}{Li_2S\ formation} = \frac{1\ mole\ per\ 2\ e^-}{x_{mole} Li_2S\ per\ e^-} = 2.21$$

With these equations, it is possible to extract the number of Li_2S moles per mole of electrons exchanged for the two different parts of the Li_2S formation (different slopes):

$$x_{1mole} Li_2S\ per\ e^- = \frac{1/2}{6.6} = 0.075$$

$$x_{2mole} Li_2S\ per\ e^- = \frac{1/2}{2.21} = 0.226$$

Thus 0.075 and 0.226 moles of Li_2S are produced per mole of electron involved in the reduction process in the two linear parts of Li_2S production vs. the capacity, respectively.

Assuming the following reaction, is it possible to extract the number of S^{2-} produced per electron theoretically:

$$2S_4^{2-} + 12e^- \rightarrow 8S_2^-$$

In theory, with the hypothesis of the previous reaction, 0.66 moles of S^{2-} per electron are produced ($8S^{2-}$ / $12e^-$).

Comparing the experimental and the theoretical amount of electrons exchanged, only 11.4% (0.075/0.66) for the first step and 34% for the second step (0.226/0.66) of the exchanged electrons lead to direct Li_2S production from S_4^{2-} reduction in the two parts respectively.

The experimentally obtained capacity for S_4^{2-} consumption in the second plateau is 240 mAh.g_s^{-1}, for the first step and 250 mAh.g_s^{-1} for the second step (490 mAh.g_s^{-1} in total), thus only 26 mAh.g_s^{-1} (0.11*240) and 85 mAh.g_s^{-1} (0.34*250) accounts for the formation of Li_2S respectively.

Regarding the theoretical capacity associated with the reaction ($S_4^{2-} + 6\,e^- \rightarrow 4\,S^{2-}$ i.e. 1256 mAh.g_s^{-1}), only 9% (111/1256) of the expected Li_2S is thus formed.

Regarding the total capacity associated with the second plateau, for the first step, 379 mAh.g_s^{-1} (490 mAh.g_s^{-1} -111 mAh.g_s^{-1}) is involved for the formation of other discharge products, which could correspond, in accordance to the literature data[3], to Li_2S_2 formation..

By assuming the formation of Li_2S_2 from S_4^{2-}, the capacity obtained (379 mAh.g_s^{-1}) corresponds to 91% of the expected Li_2S_2 quantity compared to the theoretical value (i.e. 419 mAh.g_s^{-1}) for the following reaction:

$$S_4^{2-} + 2e^- \rightarrow 2S_2^{2-}$$

The overall reaction associated with the reduction process of S_4^{2-} in the low voltage discharge plateau can be written as:

$$0.91\,S_4^{2-} + 1.82\,e^- \rightarrow\ 2 * 0.91\,S_2^{2-}$$

$$0.09\,S_4^{2-} + 0.54\,e^- \rightarrow\ 4 * 0.09\,S^{2-}$$

Then

$$S_4^{2-} + 2.36\,e^- \rightarrow 2 * 0.91\,S_2^{2-} +\ 4 * 0.09\,S^{2-}$$

This confirms the hypothesis of simultaneous Li_2S and Li_2S_2 formation and the pertinence of using the ratio between the slopes of S_8 consumption and Li_2S formation.

In conclusion, the final discharge product is composed of a mixture of Li_2S_2/Li_2S[3], with a large amount of Li_2S_2, which conveniently explains the practical low discharge capacity obtained (950 mAh g^{-1}).

The amount of Li_2S formed is lower than the one determined by Walus *et al.*[3] in accordance with the lower capacity obtained and the higher polarization of the cell. The weak efficiency to form Li_2S can be related to i) the insulating character of Li_2S which induces a passivation of the electrode surface, and ii) the weak solubility of the Li_2S_2 which may precipitate inside the

electrode porosity. This behavior may be related to the lithium ions diffusion limitation which may favor the formation of Li_2S_2 instead of Li_2S.

The present work based on tomography and XRDCT probes only a small quantity of the active material formed due to large production of soluble species in the process, and may not necessarily reflect the true image of the overall electrode evolution. Additional techniques, allowing the characterization of soluble species, should be coupled to have deeper insight into the mechanisms.

To conclude, the dynamic processes have been characterized in the positive electrode by XRDCT and absorption tomography, which give relevant information on different length scales about the species produced. The lithium ions diffusion seems to be the limiting process i) for the sulfur reduction (chapter 3) and ii) for the kinetic of S_4^{2-} reduction and the formed products. The Li_2S distribution is different than the sulfur formation (or initial coating) probably due to polysulfides migration and the need of a large active surface area. An approach of quantifying the quantity of Li_2S product shows that only a small quantity of Li_2S is produced, which may be associated with lithium ions diffusion limitation and which may favor the formation of Li_2S_2. The precipitation of Li_2S_2 can largely limit the capacity obtained. This study shows the limits of using such technics to probe the kinetic evolution of the active species while cycling. Indeed, not only the observed crystalline species are electrochemically active and thus the analysis does not quantify all active species, including soluble one.

4.4.Following the lithium/electrolyte interface

As explained in the first part of this chapter, both cells were characterized by absorption tomography in order to see the evolution of the lithium/electrolyte interface in regard to the current density. The use of higher resolution allows a better quality of data than that discussed in chapter 3.

4.4.1. Low current density

The first cell was cycled at low current density. Table 2 sums up the experimental parameters and the thickness reduction measured by both the coulometry and the X-ray measurements (Table 2). Concerning the experimental measurements, two calculations have been done. The first one measured the average reduction of the lithium thickness (labelled “total”) taking into

account the homogenous and heterogeneous oxidation. The second one probed solely the homogeneous thickness reduction of the dense lithium, *i.e.* not taking into account the heterogeneity formed along the interface.

Current density ($mA.cm^{-2}$)	Capacity (mAh)	Specific capacity ($mAh.cm^{-2}$)	Thickness reduction (µm)		
			Coulometry	Experimentally	
				Total	Homogeneous
0.23	0.69	3.5	17	16	16

Table 2 : Summary of experimental details and analysis of lithium thickness for the first cell.

First, different vertical tomograms were extracted from the 3D reconstructions, one at the initial state, one at the end of discharge (0%SOC) and one at the end of the first charge (100%SOC), in order to see the morphological evolution of the lithium/electrolyte interface (Figure 18). Contrary to previous chapter, the lithium has been placed at the bottom of the electrode stack and thus the "zero" reference is taken at the bottom of the lithium layer, which does not evolve while cycling.

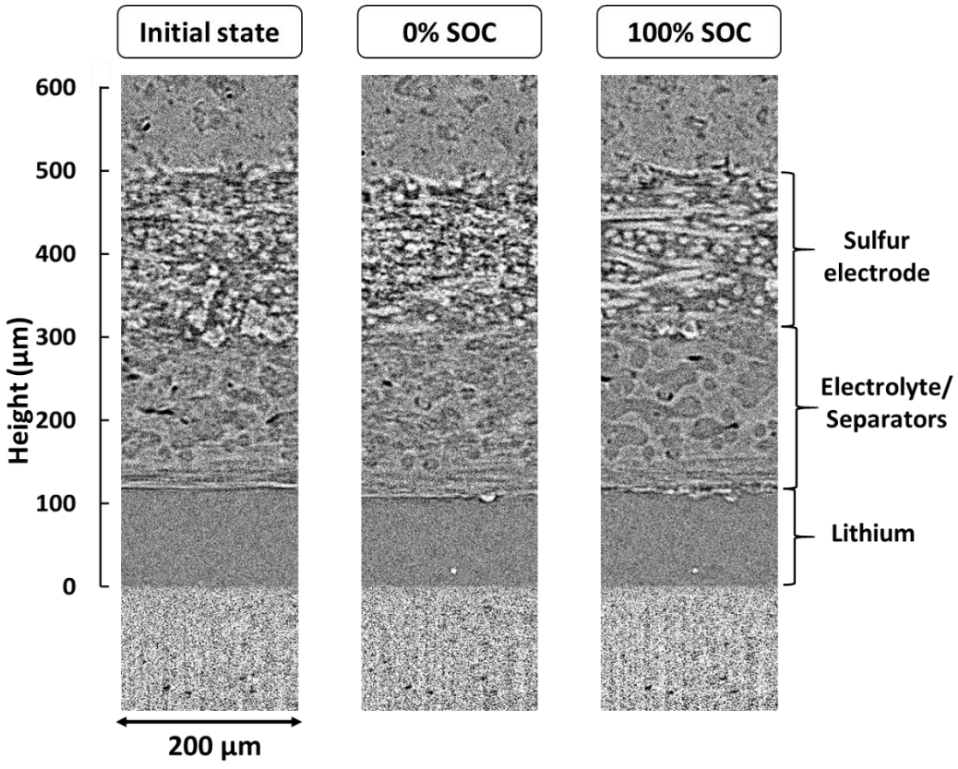

Figure 18: Vertical tomogram slice taken at different states of charge for the second cell.

The interface is relatively flat in the initial state and the lithium density is homogenous. At the end of the discharge, only few objects (pits) have been formed along the interface compared to the previous experiment.

With the low current density, the lithium stripping seems to perform in a homogenous way, with a 16 µm homogeneous oxidation in good accordance with the exchanged electrons (Table 2). During the charge, the lithium seems to be plated in the pits already created but also in a homogeneous way with an accordance between the lithium thickness plated experimentally measured (15 µm compared to the 15.7 µm expected with coulometry) thanks to tomography data. This is due to the lower current density applied (0.23 $mA.cm^{-2}$), which is approximately the half of the 0.41 $mA.cm^{-2}$ applied in the previous chapter where a heterogeneous lithium oxidation was noticed.

To gain a better picture of the processes, quantitative analysis has been carried out, similar to the one presented in the previous chapter. The lithium/electrolyte interface was segmented and the distance between the bottom of lithium electrode and the interface was calculated for each voxel defined in a 2D (x,y) view. Then, a colormap was used to show the distribution of this distance (more information is given in chapter 5). The first 3D map is taken from the top view (looking at the lithium electrode from the top view), and is shown on the left side of Figure 18. The negative of the image is shown on the right side (Figure 19) and is presented to better visualize the pits created in the lithium layer.

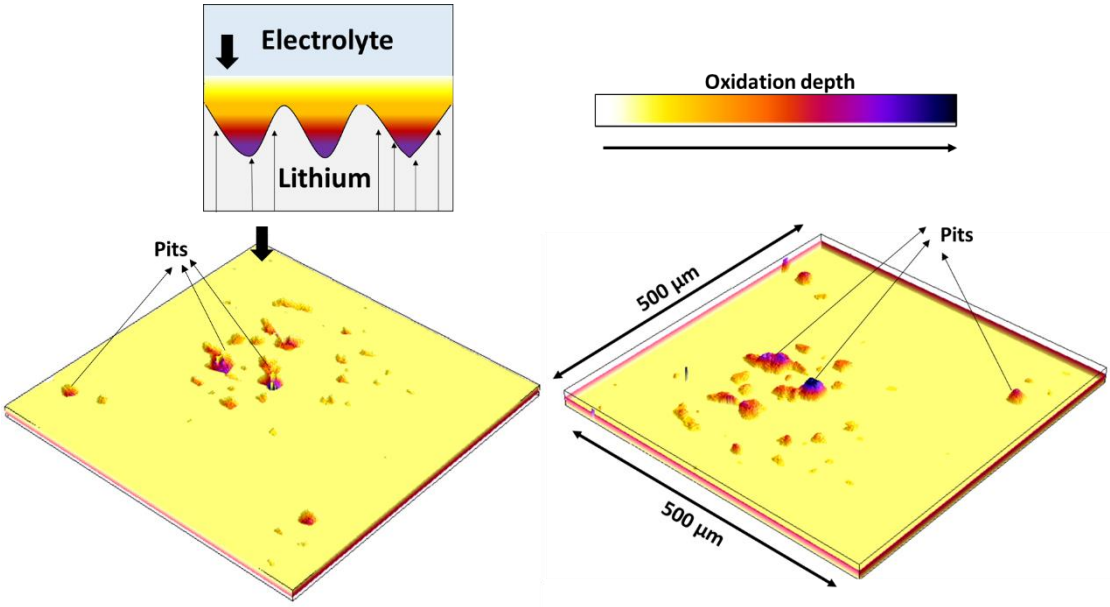

Figure 19: 3D schematic representation of the lithium/electrolyte interface at the end of the first discharge (from the first cell).

Pits created have a hemispherical shape[11] with diameter of 10-20 µm and a relatively small depth of approximately 10 µm. As seen in these figures, there is little pitting on the surface of the lithium electrode. When pits have been created, the oxidation is preferential in this area. Indeed, the few pits created, growth in diameter and in depth, while discharging the cell, as for the previous study.

4.4.2. High current density

The same analysis has been done for the second cell. The experimental parameters are summed up in the Table 3.

Current density (mA.cm^{-2})	Capacity (mAh)	Specific capacity (mAh.cm^{-2})	Thickness reduction (µm)		
			Coulometry	Experimentally	
				Total	Homogeneous
0.55	0.6	3.06	15	16	5

Table 3: Sum up of experimental details and lithium thickness analysis for the second cell.

The interface has been characterized with the same image processing as described before. The current density was 0.55 $mA.cm^{-2}$, while practical capacity obtained were similar, leading to a similar depth of lithium oxidation as for the previous cell in theory (15 µm is expected from coulometry). Different vertical tomogram slices at different states of charge during the first cycle are shown in Figure 20.

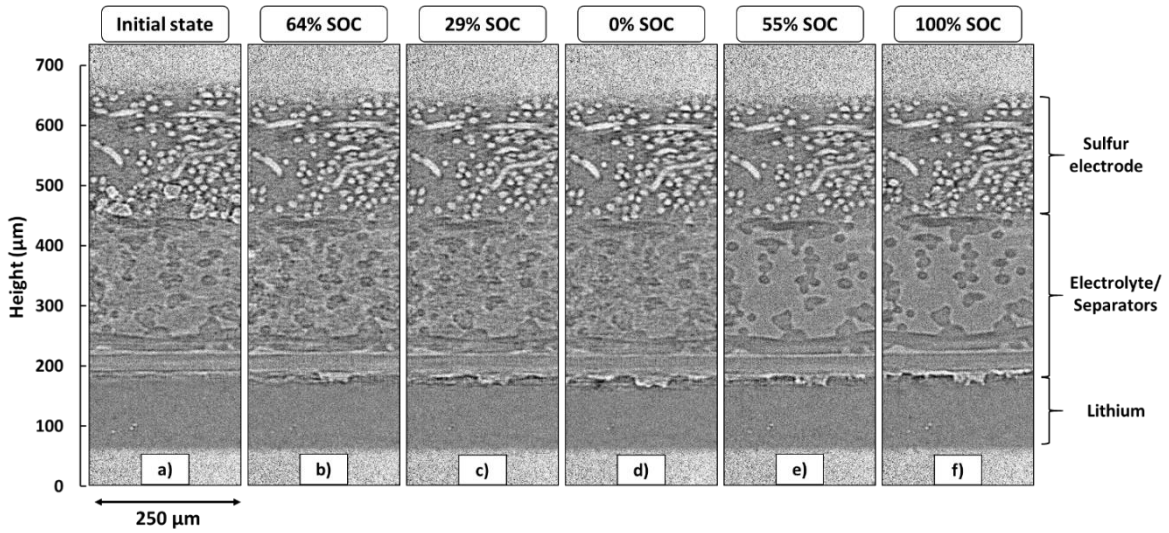

Figure 20: Vertical tomogram taken at different states of charge for the second cell a) initial state, b) 64%SOC, c) 29%SOC, d) 0%SOC, e) 55%SOC, f) 100%SOC.

The interface becomes more and more heterogeneous while discharging the cell. Lithium pits have been created since the first third of the discharge (Figure 20.b, 64% SOC). Gradually, these pits grow in diameter and in depth with new ones emerging. This proves that when the pitting occurred, lithium oxidation is more favorable in these areas. Indeed, pitting leads to SEI cracking and fresh lithium being in contact with the electrolyte, and so it is easier to oxidize this highly reactive area compared to the lithium layer "covered" by resistive SEI. During the charging process, when the lithium is plated, it seems that lithium is being reduced both in the pits formed during the previous discharge and also along the surface. The lithium is plated in a mossy form with the characteristic highly surface developed (Figure 20.e, Figure 20.f), and these lithium pits are favorable for lithium nucleation and deposition. The measured plated lithium thickness is 17.5 µm compared to the 13 µm expected to be obtained thank to coulometry, proving a deposition of thicker lithium layer attributed to mossy lithium deposition.

Thanks to the use of high resolution and phase contrast used for the absorption tomography, it was thus possible to make the same quantitative analysis on the interface between the lithium and the electrolyte.

As before, 2D maps, representing the distance between the bottom of the lithium electrode (shown with arrows) and the interface have been followed at different states of charge with the associated schema allowing a better understanding of the images (Figure 21). The distance between the bottom of lithium electrode and the interface is shown by a purple to white color. The higher is the distance, the whiter will be the color and so lower is the depth of oxidation and *vice versa*.

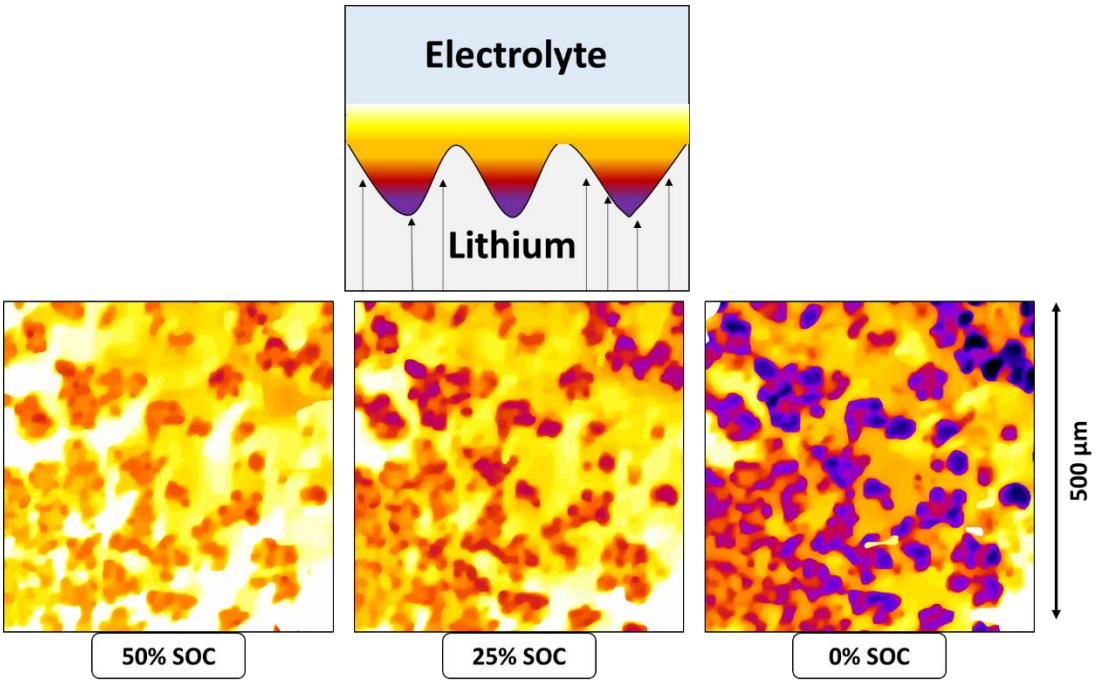

Figure 21: 2D maps of the interface between electrolyte and lithium electrode at different states of charge with a schematic representation allowing a better understanding of the maps.

The three images taken at 50, 25 and 0% SOC are drawn with the same level of color. In other words, the white colors in the different figures represent the same depth of discharge. It means that these areas are not oxidized for the different SOC. At 50% SOC, a large number of pits have already been formed with a certain depth. At 25% SOC, all pits already created grow in diameter and in depth, represented by a purple color. White zones representing area which have not been oxidized (between the different states of charge shown). However, no new pits seem to be created at this state of charge. At the end of the first discharge, (0% SOC), again, pits already created grow in diameter and in depth. The objects are approximately 30-35 µm in

diameter with a depth of approximately 30 µm. Compared to the cell 1 with lower current density (0.23 compared to 0.55 $mA.cm^{-2}$), the objects are three time bigger with depths multiplied by 3 and diameters multiplied by 2 to 3. It means that by more than doubling the current density, it more than doubled the pits parameters. The pits morphology is very similar to those observed in the previous chapter. Even if a slightly lower sulfur loading was used (3.3 compared to previous 5.1 $mg.cm^{-2}$), a similar current density (0.55 compared to previous 0.41 $mA.cm^{-2}$) was applied. This proves again that the heterogeneity of stripping is driven by the current density per square centimeter and not directly driven by the sulfur loading in the electrode. Then the PS concentration in the electrolyte seems to have a negligible effect compared to the current density effect.

A 3D representation is shown in order to better visualize the heterogeneous interface. Two representations are shown. The first one is the classical lithium/electrolyte interface (with the electrolyte pitting) whereas the negative of this images is drawn which allows to better see the pits morphology (Figure 22).

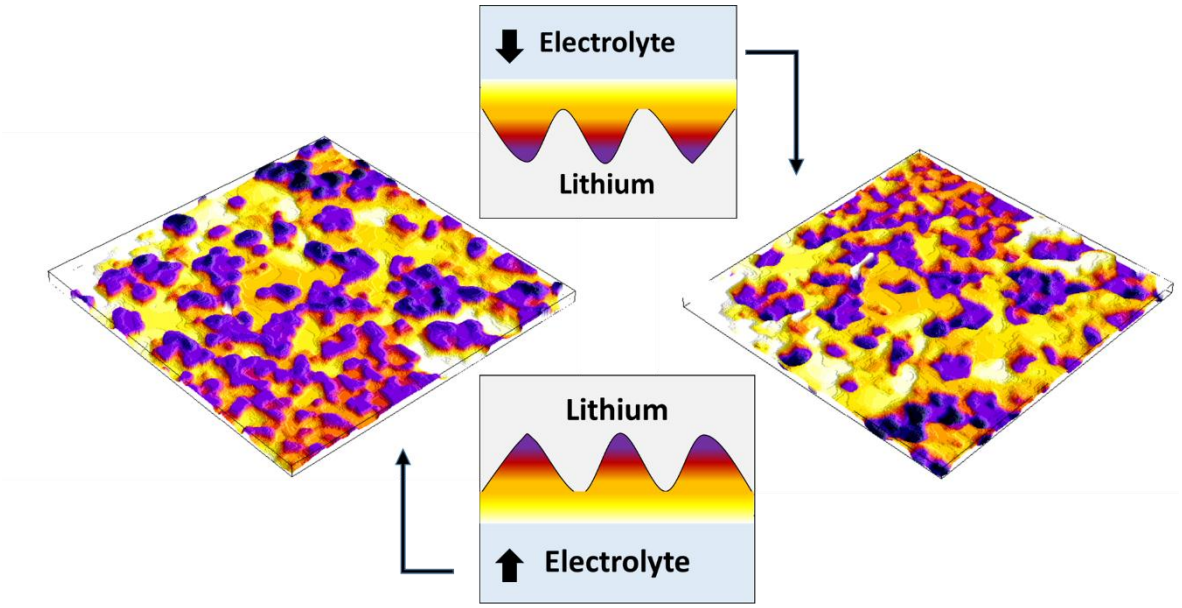

Figure 22: 3D schematic representation of the lithium/electrolyte interface at the end of the first discharge with helping understanding schema (from the second cell).

As said before, the interface is heterogeneous with a large number of pits all along the interface. The same assumption, as previous experiment, can be made that pitting seems to take place in the grain boundaries of the lithium metal electrode by looking at the distribution of pits along the interface.

The second cycle was also been characterized and a 3D "classical" representation of the interface at the end of the second discharge is shown in Figure 23.

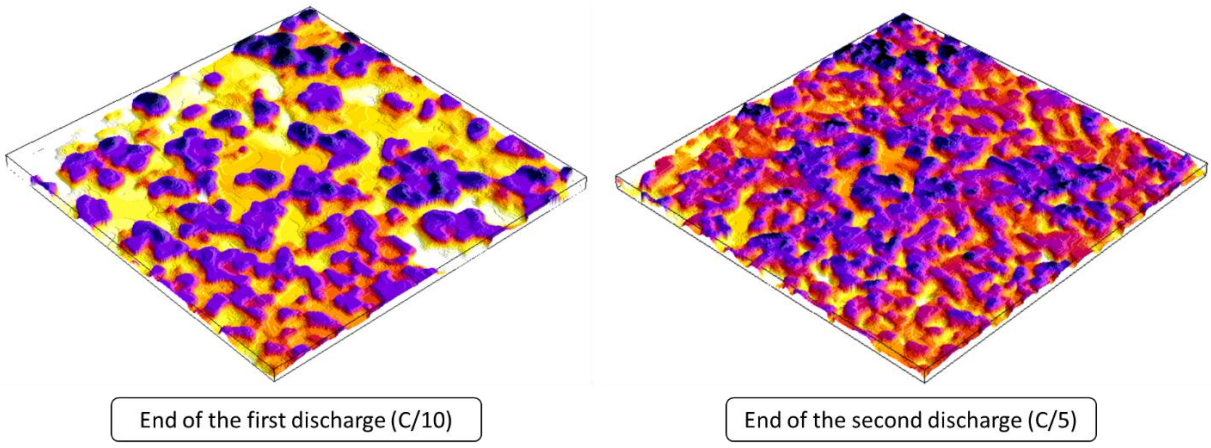

Figure 23: 3D representation of the lithium/electrolyte interface at the end of first discharge (C/10) and the end of the second discharge (C/5).

The interface is more heterogeneous at the end of the second discharge. Pits are formed in the whole surface of the electrode. The depth of the pits is remarkably the same in both images. Therefore, increasing the current density (C/5 for the second cycle) does not lead to deeper pits, but to an increase of the pits number/quantity. Furthermore, the pits already formed during the first discharge, seem to be at the same place during the second discharge. Thus, the lithium heterogeneity starts since the beginning of the cell life and affects the whole cell lifetime.

A summary table is shown to see the different parameters and the results obtained (Table 4).

	Chapter 3	Chapter 4 - Cell 1	Chapter 4 - Cell 2		Literature [12]		
					Carbonates based electrolyte Li//Li		
Loading (mg/cm²)	5.1	3.7	3.3	3.3			
Current density (mA/cm²)	0.41	0.23	0.55	1.1	1	5	10
Thickness reduction (µm)	16	16	15	12			
Pits depth (µm)	30	10	30	30			
Pits diameter (µm)	25 to 30	10 to 20	30 to 35		<10 µm	~30 µm	~ 40-50 µm canals
Distribution	Half of the surface	A few	Half of the surface	All surface	A few	A few	All surface
Morphology	Hemi-spherical	Hemi-spherical	Hemi-spherical Canals	Canals			Canals

Table 4: Sump-up of the different parameters tested and the results obtained.

The results are quite similar between those obtained by Shi *et al.*[12], in carbonate based solvents and symmetrical Li//Li system but with a current density of 1 mA.cm^{-2}, and with the cell 1 (in chapter 4) with current density five time lower. It proves that the electrolyte has a large impact

on the lithium stripping heterogeneities, with both the use of ether solvents and the highly reactive polysulfides. Indeed, the use of ether solvents, which are less reactive than carbonates at the lithium surface[12] and provide less efficient SEI, may favor the formation of heterogeneity on the lithium surface.

4.5. Conclusions

To conclude, XRDCT and absorption tomography allowed to deeper characterize the sulfur positive electrode while cycling. Indeed, the positive electrode state have been quantified at different length scales from the whole electrode to the single particles in order to see the heterogeneity of the electrode functioning. The sulfur consumption is homogeneous in the depth of the electrode, with first the disappearance of the smaller particles. The high resolution absorption tomography enables to see the isotropic reduction of sulfur particles while discharging the cell, and that particles taken at different depths in the electrode seem to evolve in a homogenous way. The results are a bit different that those obtained in the previous chapter, where it has been shown a kinetic gradient at the top of the electrode. However, in this experiment, the XRDCT slices have been taken deeper in the electrode and thus the limitation is not visible. It has been demonstrated that sulfur particles reduction leads to a collapse of the CBD and thus a loss of electrode integrity. The Li_2S formation and consumption show complex behaviors, which may be understood by rate limitation due to by lithium ions diffusion and Li_2S nucleation. The lithium ions diffusion limitation is amplified by the thickness of the NwC, which can have a negative effect on the Li_2S conversion by promoting Li_2S_2 formation and precipitation in the large porous structure. In addition, the low PS diffusion through the electrode could also explain these specific phenomena. However, the NwC stable structure preserves the electronic network along cycling.

Likewise, the quantitative analysis of absorption tomography data showed inherent challenges even with high resolution and high statistics, with the segmentation of particles for a wide sampling requiring well-developed image processing technics. Indeed, the analysis of β-sulfur was not possible. However, it gives relevant images in the *operando* mode and allows to follow the morphological changes while cycling. It could be coupled with FIB-SEM to have a deeper insight in the nanoscale of the electrode. In addition, the NwC, relatively heavy and thick, is not totally used and have to be improved to get the best of this current collector.

The lithium/electrolyte interface heterogeneity has been shown to be driven by the current density. The higher the current density is, the higher the heterogeneity will be at the interface, with the presence of pits. However, with relative low current density (below 0.2 $mA.cm^{-2}$), it has been demonstrated that the lithium stripping/plating is done in a more homogenous way. These values of current density are not relevant, with applications requiring high capacity and/or high C-rate leading to high current density. While discharging, the first pits created along the interface are well places for the lithium oxidation due to the fresh nude SEI being in contact with electrolyte. That is why, the pits grow in diameter and in depth. During the charging process, lithium seems to be plated in the pits already formed and is deposited in a mossy form with a very high specific surface. The next discharge is similar to the previous stripping with the same objects found after 2 cycles. However, these heterogeneities are created at the beginning of the first discharge and probably lead to a progressive degradation of the lithium/electrolyte interface, which will induce a premature end of life. Therefore, understanding the lithium stripping/plating processes in the first cycle is compulsory to follow the cycle life, but looking at prolonged cycling would also allow to see the evolution of these heterogeneities while cycling.

References

[1] S. Walus, Accumulateur Lithium/Soufre : Développement et Compréhension Des Mécanismes Électrochimiques, PhD Thesis, **2015**.

[2] G. Tonin, G. Vaughan, R. Bouchet, F. Alloin, M. D. Michiel, L. Boutafa, J.-F. Colin, C. Barchasz, *Sci. Rep.* **2017**, *7*, 2755.

[3] S. Waluś, C. Barchasz, R. Bouchet, J.-C. Leprêtre, J.-F. Colin, J.-F. Martin, E. Elkaïm, C. Baehtz, F. Alloin, *Adv. Energy Mater.* **2015**, *5*, n/a.

[4] S. Waluś, C. Barchasz, J.-F. Colin, J.-F. Martin, E. Elkaïm, J.-C. Leprêtre, F. Alloin, *Chem. Commun. Camb. Engl.* **2013**, *49*, 7899.

[5] T. Zhang, M. Marinescu, S. Walus, G. J. Offer, *Electrochimica Acta* **2016**, *219*, 502.

[6] J. Zheng, M. Gu, C. Wang, P. Zuo, P. K. Koech, J.-G. Zhang, J. Liu, J. Xiao, *J. Electrochem. Soc.* **2013**, *160*, A1992.

[7] M. Helen, M. A. Reddy, T. Diemant, U. Golla-Schindler, R. J. Behm, U. Kaiser, M. Fichtner, *Sci. Rep.* **2015**, *5*, 12146.

[8] S. Drvarič Talian, J. Moškon, R. Dominko, M. Gaberšček, *ACS Appl. Mater. Interfaces* **2017**, *9*, 29760.

[9] A. ROBBA, Développement et Compréhension Des Mécanismes Électrochimiques Des Accumulateurs Lithium-Ion/Soufre, PhD Thesis, **2018**.

[10] L. Zielke, C. Barchasz, S. Waluś, F. Alloin, J.-C. Leprêtre, A. Spettl, V. Schmidt, A. Hilger, I. Manke, J. Banhart, R. Zengerle, S. Thiele, *Sci. Rep.* **2015**, *5*, 10921.

[11] O. O. Taiwo, D. P. Finegan, J. M. Paz-Garcia, D. S. Eastwood, A. J. Bodey, C. Rau, S. A. Hall, D. J. L. Brett, P. D. Lee, P. R. Shearing, *Phys. Chem. Chem. Phys.* **2017**, *19*, 22111.

[12] F. Shi, A. Pei, D. T. Boyle, J. Xie, X. Yu, X. Zhang, Y. Cui, *Proc. Natl. Acad. Sci.* **2018**, *115*, 8529.

Table of figures

Chapter 5: Experimental methods and techniques

5.1. Electrochemical characterizations

5.1.1. Electrode preparation

The electrode elaboration was largely based on Sylwia Walus thesis[1]. First, an ink was prepared from a sulfur commercial powder (-325 mesh, Aldrich) and carbon additive (Super P®, Imerys) was added to ensure the electronic conductivity of the electrode, as sulfur has a very weak electronic conductivity. A carbon/sulfur blend was thus prepared in mortar and was grinded with a small amount of cyclohexane. A polymer binder composed of PVdF (5130, Solvay) dissolved at 10% in N-methyl-2-pyrrolidone (NMP, anhydrous) was used. The mixture thus obtained has the weight ratio of 80/10/10 wt% (S_8, Super P®, PVdF). After homogenization in a dispermat® (4000 rpm during 10 minutes), the mixture was coated using a doctor blade technic, usually onto a non-woven carbon collector[1] (NwC). The NwC current collector is composed of carbon fibers interweaved and the ink penetrate in the porosity creates by the carbon matrix. The NwC porosity is 80%. However, it remains a coating on the current collector which could be linked to a crust and be called the carbon binder domain (CBD) with an approximate porosity of 40%. The adjustment of ink viscosity, by adding NMP as well as the speed of the blade allowed to control the loading on the electrode by tuning sulfur penetration into the current collector.

As the weight of the 3D current collector could vary up to 1 mg per disk of 14 mm in diameter of NwC, the current collector disks were cut and weighted before electrode coating. A schematic representation is shown in Figure 1.

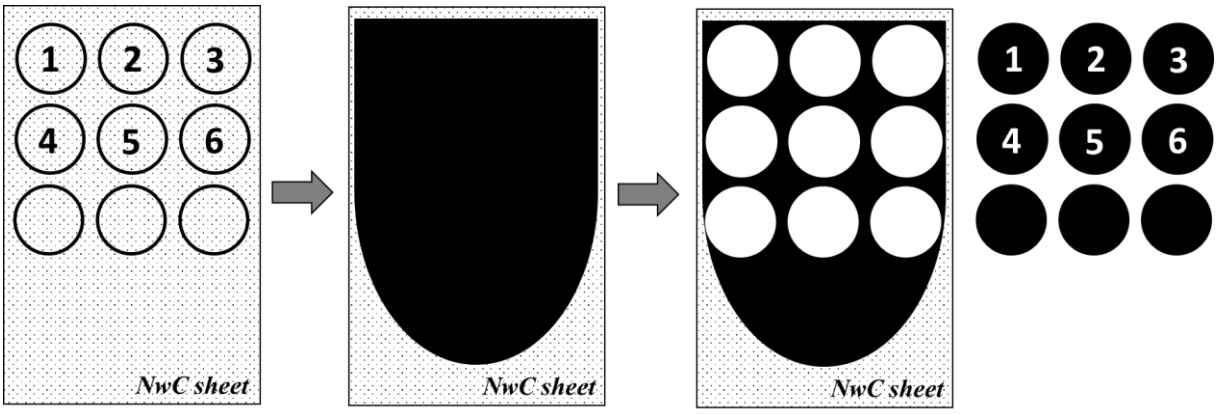

Figure 1: Schematic representation of the electrodes fabrication.

With this technic, it was possible to diminish considerably the uncertainty of the loading determination and thus of the real capacity of the electrodes. All the electrodes were prepared

with this technic for both coin and *operando* cells. The electrodes were then dried in an oven at 55°C during 48 hours with the purpose of evaporating the NMP used for coating. The loadings obtained were from 3 to 5.0 $mg_s.cm^{-2}$ and corresponds approximately to a coating thickness of 30 to 50 µm on the top of the current collector. The electrodes were then put into glove box for the cell assemblage.

5.1.2. Coin cell preparation

The coin cells were assembled in a glove box filled with argon in order to avoid any reactions of the lithium metal and the electrolyte with oxygen and moisture. The positive electrode, cut as 14 mm in diameter, was placed in the upper (positive) casing and was filled with the electrolyte (Figure 2). Two separators were then placed (each with a 16.5 mm diameter): the first one is the Viledon®, a porous (55%) polyolefin membrane of 250 µm thick, which acts as electrolyte reservoir and the second one is a Celgard® 2400, a porous (41%) polypropylene membrane of 25 µm thick, which acts as physical barrier between the two electrodes. 150 µl of electrolyte were then added to fill the separators porosity. After that, the lithium foil (16 µm in diameter, 135 µm, Rockwood Li) was placed on the separator and covered with a 0.5 mm thick stainless steel spacer. A spring was then placed on the spacer in order to maintain sufficient pressure on the electrode stack. Finally, the negative casing was placed on the spring and the coin cell was made airtight (Figure 2).

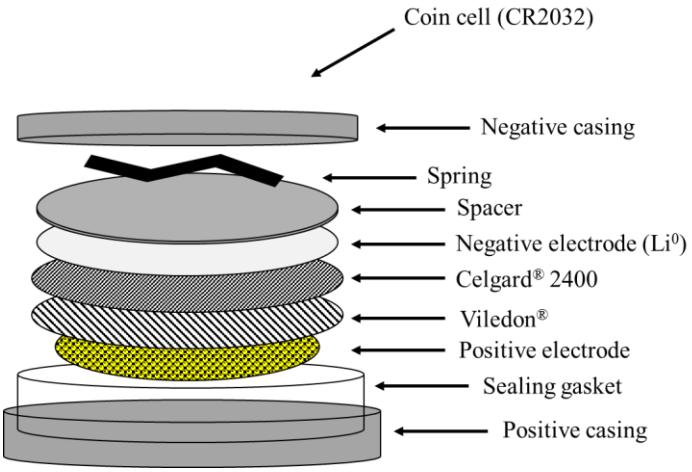

Figure 2: Schematic representation of a two-electrodes coin cell (CR2032).

The electrolyte, based on Céline Barchasz[2] thesis, was composed of bis(trifluoromethylsulfonyl)amine lithium salt (LiTFSI, Aldrich) dissolved at 1 $mol.L^{-1}$, in a

mixture of tetraethylene glycol dimethyl ether (TEGDME, Aldrich) and 1,3-dioxolane (DIOX, Aldrich) in an equivalent volume ratio. 0.1 M of lithium nitrate ($LiNO_3$)[3] was added. The solvents were previously dried on 3Å molecular sieves, the lithium salts and $LiNO_3$ were dried in Buchi ® at respectively 150°C and 50°C under vacuum for 48h.

5.1.3. Electrochemical testing

The coin cells were then cycled using Arbin or VMP® biologic battery cyclers in galvanostatic mode. The C-rate was generally fixed at C/20 which corresponds to a full theoretical discharge (or charge) in twenty hours.

The cut off potentials were fixed at 1.5-3.0V.

The cycling temperature was fixed at 22°C and the theoretical capacity was calculated based on the specific capacity of sulfur (1675 $mAh.g_s^{-1}$) and the loading of the electrode in the cell. Typical galvanostatic curves are shown in Figure 3. The classical shape, largely commented in literature[3–5], is obtained. After several cycles the capacity is stabilized up to 750 $mAh.g_s^{-1}$ in accordance with the performances obtained with this configuration[1] (C/20, TEGDME-DIOX, 1M LiTFSI + 0.1M $LiNO_3$ based electrolyte, 3.8 $mg.cm^{-2}$).

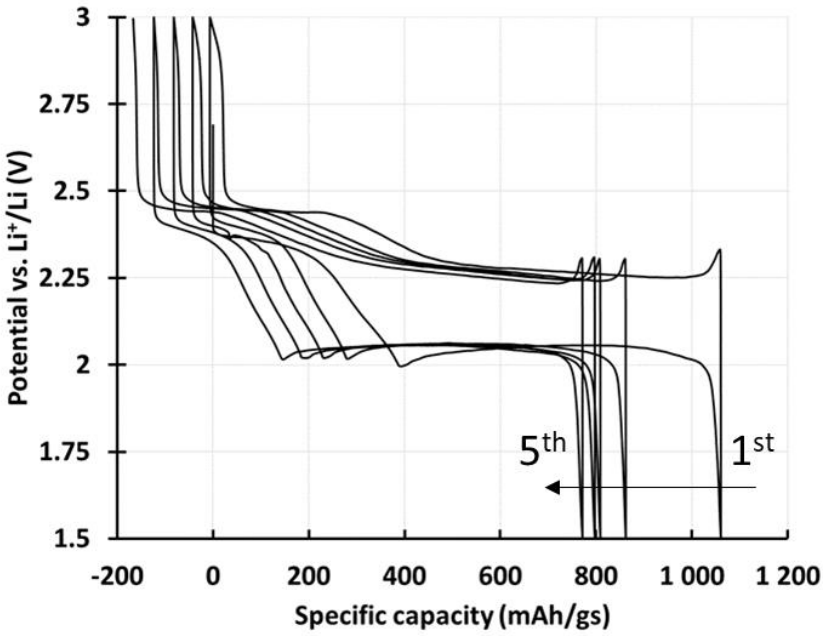

Figure 3: Galvanostatic curve of the first 5 cycles of a Li/S coin cell.

5.2. Operando cell developments

In order to perform synchrotron characterization, a suitable new *operando* cells had to be developed. A large amount of effort went into this design and the subsequent improvement of the cell between the experiments.

5.2.1. First *operando* cell

The first cell was developed before my thesis, with the aim of being suitable with synchrotron experiments, by reducing, as much as possible, the cross-section of the cell, compared to coin cells, without altering the electrochemical performances.

The cell was prepared in an aluminum crucible with a diameter of 6.7 mm and a height of 5 mm (Figure 4).

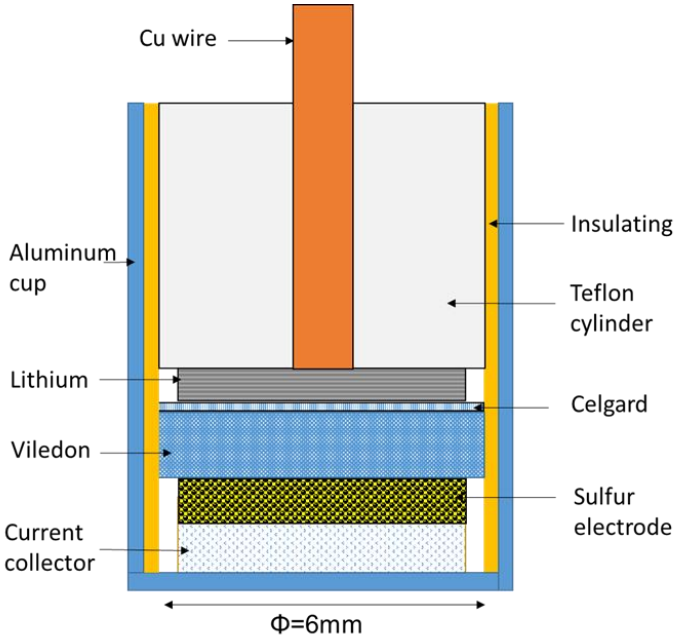

Figure 4: Schematic representation of the 1st operando cell.

An insulating layer of Kapton® was taped inside the aluminum container to avoid any short-circuit when assembling the cell. The cell was assembled in a dry room (−40 °C dew point) using a positive electrode (described above, soaked with organic electrolyte), a lithium foil, a porous separator (Celgard® 2400) and a Viledon® electrolyte reservoir, both soaked with organic electrolyte. Electrochemical tests were carried out with VMP® biologic in a voltage range of 1.5–3.0 V at the current rates of C/20 (≈0.33 mA.cm^{-2}) for the first cycle and C/40 for the second (≈0.17 mA.cm^{-2}).

Despite the general suitability of the cell for synchrotron experiments, several problems have been identified during the first run of experiment at synchrotron facilities. Thus new cell designs have been developed in order to improve the electrochemical performance, control the pressure on the electrode stack and optimize the geometry for X-ray scattering and absorption experiments. This is the main objective of the next section.

5.2.2. Development of *operando* cell

5.2.2.1. Pressure controlled environment

As explained in the chapter 2, a lack of pressure has been shown during the experiment which probably enhance certain undesirable phenomena while cycling, such as leading to a large increase of the lithium electrode thickness during plating. Thus, a new design has been conceived and developed in order to control the *operando* cell pressure, as for coin cells. For that, a spring has been used to implement a pressure in the same range as the one measured in coin cells.

The pressure applied by the spring on the electrode stack in coin cells was estimated with two methods.

First estimation of the pressure:

The first method was to measure the thickness of the electrodes/electrolyte stack, and estimate the spring compression. By considering that each layer is incompressible, and estimating the thicknesses of the cell components (see Figure), the compression ("L") of the spring with an initial height ("L_0") is given by :

$$L = L_0 - (Height_{coin\ cell} - Thickness_{2\ casings} - Thickness_{elect/electrolyte/elect})$$

The height of coin cell was measured with a micrometer lever gauge, and a mean value of 10 measures was taken, with an average height equal to 3.1 mm. The thickness of the casing measured with a micrometer lever gauge too and validated by absorption tomography was equal to 0.29 mm. The thickness of the electrodes stack was measured summing all the cell components (sulfur electrode, separators, lithium and spacer) thicknesses.

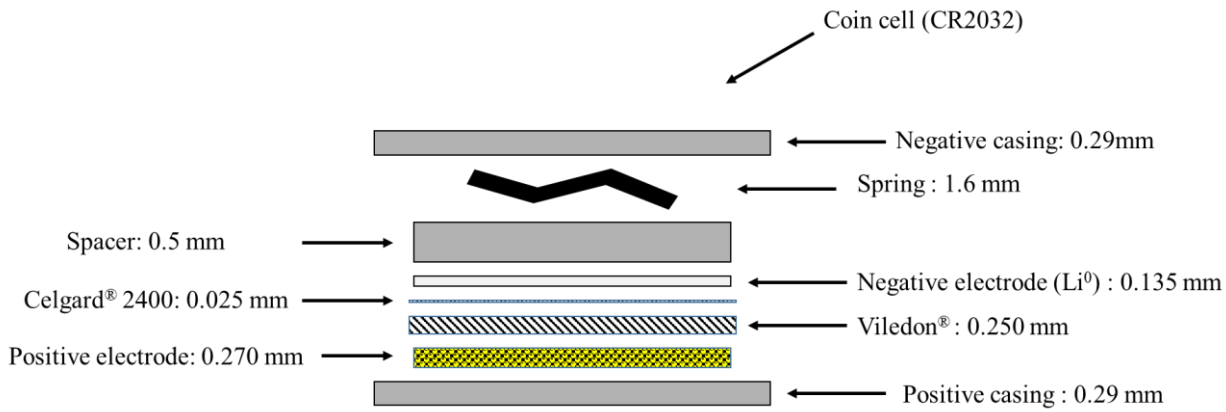

Figure 5: Schematic representation of a coin cell with the associated thicknesses of each layer.

From Figure 5, the spring compression is thus given by:

$$L = 1.6 - (3.1 - \ 0.58 - 1.18)$$

$$L = 0.26 \text{ mm}$$

The spring stiffness ("k") was measured in a compression machine and the value obtained was 87 $N.mm^{-1}$.

So the pressure applied by the spring on the electrode stack is ("r" being the radius of the electrode):

$$P = \frac{k * L}{\pi * r^2} = \frac{87 * 0.26}{\pi * 8^2} = 112\ kPa = 1.1\ bar$$

The pressure applied by the spring on the spacer is approximately 1.1 bar. However, this analysis assumes that all cell components are incompressible, which may not be representative of the porous electrode and the separators behaviors. That is why a second estimation of the pressure was done in order to confirm the previous calculation.

Second estimation of the pressure:

A coin cell was assembled in a glove box, but without electrolyte. The assumption is that adding the electrolyte has a negligible effect on the pressure applied on the electrode stack. Then, this coin cell was compressed at constant displacement under a compression machine. With this coin cell configuration, during the first four millimeters of displacement, a linear evolution of the force applied versus the displacement was observed with a value of 1.2 bars by dividing the

force by the cross-section. It allowed to confirm the previous estimation of the cell pressure, with a difference below 10%. For the subsequent parts of the cell characterization, the pressure applied was approximately fixed at 1.2 bars (0.12 $N.mm^{-2}$) thanks to the better precision of the second method of estimation.

So the force needed to be applied in the *operando* cell, where the electrode surface ("S") was 5 mm in diameter, is given by:

$$F = P * S = 0.12 * 2.5^2 * \pi$$

$$F = 2.4\ N$$

The force required on the electrodes stack was thus about 2.4 N and will be control with a spring compression.

5.2.2.2. Estimated electrolyte volume

Another improvement performed, concerns the electrolyte/sulfur weight ratio, which has a large impact on the electrochemical performance. The necessary volume of electrolyte to be comparable with coin cell has been deduced from coin cell assembly.

The amount of electrolyte was deduced from the free volume of coin and *operando* cells. However, one should keep in mind that this approach is based on practical values because the exact value of electrolyte in a coin cell is unknown. The different parameters of each part of stack are detailed in Table 1.

	Diameter (mm)	Surface (mm^2)	Thickness (µm)	Volume (mm^3)	Porosity	Free volume (µL)
C2400	16.5	213.8	25	5.3	41%	**2.2**
	6	28.3	25	0.7	41%	**0.3**
Viledon	16.5	213.8	240	51.3	55%	**28.2**
	6	28.3	240	6.8	55%	**3.7**
NwC	14	153.9	210	32.3	80%	**25.9**
	5	19.6	210	4.1	80%	**3.3**
Electrode	14	153.9	50	7.7	40%	**3.1**
	5	19.6	50	1.0	40%	**0.4**

Coin cell

Operando cell

Table 1: Estimated free volume of each cell components, for both coin cell (blue) and operando cell (beige).

The free volume of the different cell components of a coin cell is 59.4 µL (2.2 + 28.2 + 25.9 + 3.1) and the amount of electrolyte introduced in total is equal to 150 µL, thus in large excess, and part of this excess is removed when the coin cell is sealed. In the *operando* cell, the free volume of the stack is 9.4 µL so, the amount of electrolyte added is fixed at 24 µL in order to be in the same conditions as those in coin cells. Part of the electrolyte is used to soak the electrode and separators before the assembly.

5.2.2.3. New *operando* cell design

In order to improve the data resolution, a new architecture of the *operando* cell was also developed. As for the first experiment, the dimensions have been chosen to be 5 mm in diameter for electrodes and 6 mm for the separators. In this case, a glass tube has been used as a casing, in order to optimize the homogeneity of the diffraction signal from the cell container beneficial to the reconstruction process[6]. A spring and two pistons, both in stainless steel, were used to maintain a well-defined and controlled constant pressure on the electrodes stack and ensure an airtight sealing with the used of two sealing gaskets per piston. A pressure evacuation system, consisting of a 1 mm hole through the upper piston, was used to avoid the increase of internal pressure while assembling the cell when inserting the upper piston. In order to guarantee the sealing of this upper piston, the top was threated. A schematic representation of the cell is shown Figure 6.

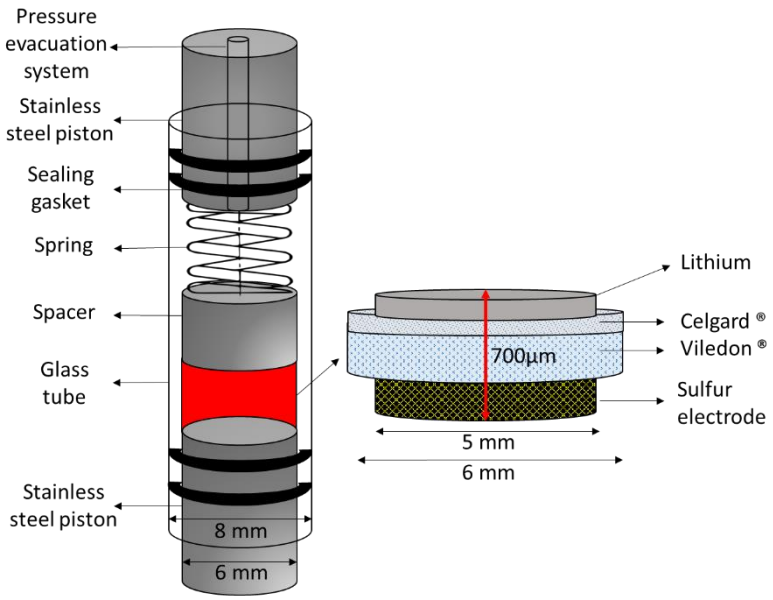

Figure 6: Schematic representation of the operando cell with the pressure evacuation system.

After assembling cells in a glove box, they were transferred in dry room, under controlled atmosphere, whose purpose is to seal the cell using a compression machine. In order to apply the desired force to the *operando* cell (2.4 N, 1.2 bar in pressure, see the paragraph above), the compressive machine applied a displacement of 4.8 mm for a 0.5 $N.mm^{-1}$ spring. After that, the two pistons were sealed onto the glass tube with glue and maintained in the compressive machine during at least 2 hours. This architecture was assumed to be the most suitable for synchrotron experiments and was validated in galvanostatic tests. This design was suitable for initial cycling (first cycles were observed only), and was chosen for the characterization at the ESRF (second experiment, see chapter 3). Indeed, it was difficult to perform prolonged cycling in this type of cell due essentially to the large dead volume and that electrolyte dry out along the spacer leading to a loss of active materials.

The last improvement was made to improve the quality of the data. Indeed, as the beam is being diffracted when passing through the sample with an angle of up to ca. 45°, as represented in the Figure 7, the materials used for the spacer can cause significant absorption in the diffracted beam. As the diffraction in a given pixel of the detector comes from various places along the beam path, carrying out an analytical absorption correction is non-trivial, requiring an iterative ray-tracing algorithm. A better solution is to use a light material along the beam path so that diffracted beam attenuation is negligible and can be neglected.

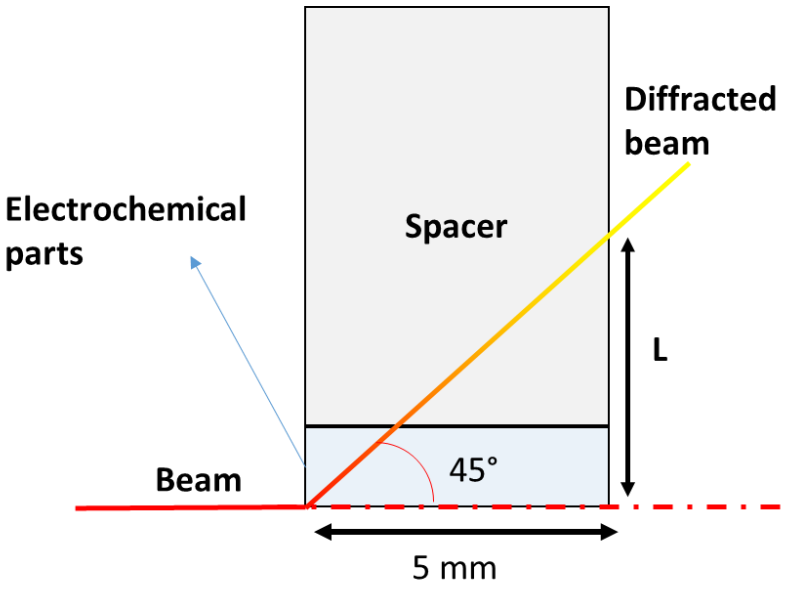

Figure 7: Schematic representation of X-ray diffracted beam.

Therefore, graphite has been chosen to replace the stainless steel in the upper piston (diffraction was measured in the upper quadrant of the pattern). In addition, a minimum height of the spacer could be estimated "L", which represents the maximum distance of beam deviation. The calculation is given by the following equation, where 5 mm is the electrode diameter and 45° the angle of diffraction:

$$L = 5 * \arctan(45)$$

The spacer therefore needs to be at least 7.7 mm in height. An 8 mm spacer was used in these experiments. The same design as before has been chosen by replacing the spacer by a graphite one.

This design has been chosen for the last experiment at the ESRF (see chapter 4).

The experimental set-ups of the three experiments are detailed in the next section.

5.3. Experimental set-up

5.3.1. 1st Experiment

In situ and *operando* XRD and X-ray absorption measurements were carried out at beamline ID15A at the European Synchrotron Radiation Facility (ESRF: Grenoble, France) with a monochromated incident energy of λ = 0.1778 A (69.7 keV). This high energy was required in order to have sufficient X-ray signal after the beam go through the cell (2 aluminum walls to be passed through) and to minimize the diffraction peak broadening effects due to sample thickness, by compressing the diffracted pattern to low angles. XRD patterns and absorption tomography data were recorded alternatively with a recording frequency of approximately 20 min, assuming that this time is characteristic of the phenomenon occurring while cycling at a C-rate = C/20. The time for switching geometry and to measure the absorption tomography took 5 min. The beam size was varied around 1.5*1.5 mm² for tomography, and 20*20 µm² full width at half maximum (FWHM) for diffraction, by inserting X-ray compound refractive lenses into the beam for the latter measurements. Due to the large size of the cell, only local tomography was carried out on a cylinder in the center with a diameter of 1210 µm, corresponding to the size of the detector used. Due to the relative homogeneity in absorption within the cross section of the cell at a given height, it was considered that the errors induced by performing local tomography were small. The entire active height of the cell (~650 µm) was probed. The image resolution for the tomography was 1.2*1.2*1.2 μm^3 per voxel,

corresponding to the size of a detector pixel. X-ray diffraction beam was carried out over the entire height of the active part of the cell, in 20 μm steps.

One electrical contact was made to the aluminum casing by welding and the second with the upper copper wire. As the cell rotated a half turn during measurement and rewound, no rotate contacts were necessary.

5.3.2. 2nd Experiment

As shown in chapter 2, classical XRD requires almost perfect alignment of the beam perpendicular to the cell axis in order to not degrade the spatial resolution through the depth of the electrode. In order to overcome this limitation, as well as to have spatially resolved information in the plane of the electrode, X-ray Diffraction Computed Tomography (XRDCT) was used for the second experiment (high energy for parallax and no correction). It allows the reconstruction of the XRD pattern in each voxel of the cell with a resolution defined by the beam size and produces time resolved 3-dimensional maps. The reconstruction is similar as the one in absorption tomography. As the technic requires the sample to translated and rotated through the beam to collect an adequate number of projections to achieve the desired spatial resolution, it is necessarily time consuming, but improvements in the beamline, notably the acquisition of a new detector and the refinement of data collection algorithms, allowed the experiments to be carried out with a comparable time resolution to the first series, with notable higher quality data acquires.

The beam requirements for XRDCT are almost identical to those of the classical microdiffraction carried out previously, where the need for high energy incident beam is further enhanced in order to avoid having to carry out additional absorption corrections on the data, and to reduce the parallax error due to sample thickness which greatly degrades the quality of the reconstruction.

In addition to XRDCT, absorption in the phase contrast mode has been done in order to better differentiate, with respect to pure absorption contrast tomography, the species in the electrode part, which have a similar electron density value, *i.e.* a similar absorption coefficient. In particular, the distinction between sulfur and carbon are generally complicated in pure absorption mode.

The electrical wires were welded to the pistons for electrical contacts and then fixed to rotating electrical couplings (slip rings) to allow the continuous sample rotation (Figure 8) required for XRDCT.

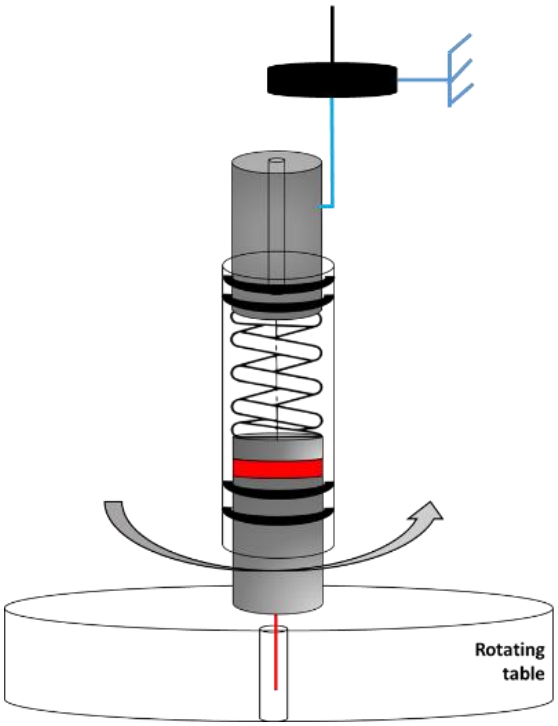

Figure 8: Schematic representation of the operando cell with the slip ring.

Operando XRDCT and X-ray absorption and phase contrast tomography measurements were performed at beamline ID15a at the ESRF as well, with a monochromated incident wavelength of λ=0.1897Å (energy 65.35 keV). XRDCT and absorption tomography data were recorded alternatively with a period of 32 minutes. The XRDCT measurement took approximately 20 minutes. The time to switch configuration and measure absorption and phase contrast tomography took approximately 12 minutes.

The measurements were carried out on the whole cell, a cylinder of 6 mm diameter and 650 µm height. The image resolution for the absorption tomography was 3.18*3.18*3.18 μm^3 per voxel, corresponding to the size of the detector pixel. X-ray diffraction tomography required acquisition of diffraction patterns while scanning the sample through the beam and rotating. The rotation speed was approximately 60 rpm. The patterns were acquired so that each voxel was 300*300 μm^2 in the (x,y) plan perpendicular to the battery axis and 20 µm in the vertical direction, which corresponds respectively to 21*21 patterns per slice and 32 vertical layers (~14 000 patterns overall per time step).

Diffraction patterns were azimuthally integrated using locally modified versions of pyFAI software[7,8]. Data were corrected for detector geometry, response and transparency. Reconstructions were performed using local codes for filtered back projection point-by-point in the diffraction patterns. Spatial and temporal phase maps were constructed using multiple peaks of the phases of interest.

5.3.3. 3rd Experiment

To improve the electrical contact (see chapter 3), it has been decided to glue the upper wire along the cell and pass through the hole of the rotating table. The schematic representation is shown in Figure 9.

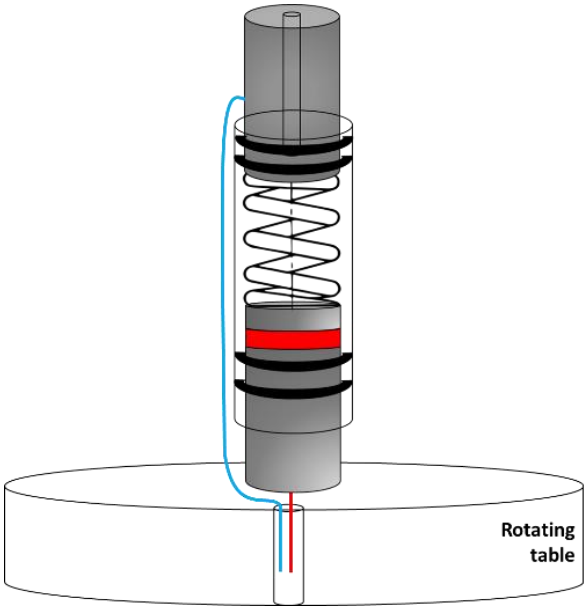

Figure 9: Schematic of operando cell used for the 3rd experiment, with wires passing through the rotating table.

This allowed to avoid any force on the cell which could misalign the cell to the beam and induce electrical contacts problems and lower the electrochemical response. However, in each rotation, the signal of the rotation wire was recorded, and it contribution to the diffraction data had to be suppressed in the reconstruction.

Operando XRDCT and X-ray absorption and phase contrast tomography measurements were performed at beamline ID15a at the ESRF. XRDCT and absorption tomography data were

recorded alternatively with a period of 22 minutes. The XRDCT recording took approximately 13 minutes.

As in the second experiment, the resolution was determined by experimental considerations. The time necessary to carry out the XRDCT experiment goes essentially as the inverse of the product of the in-plane resolution squared and the vertical resolution. Since the variation in the cell is higher in the vertical direction, along which the different elements are packed, this direction was measured with almost the highest resolution obtainable with optical configuration used. The in-plane resolution, which has a higher impact on the time of the experiment, was then determined so as to achieve the desired time resolution.

The absorption tomography measurements were carried out on the center part of the cell, a cylinder of 1.84 mm diameter and 650 µm height with an image resolution of 0.717*0.717*0.717 μm^3 per voxel, corresponding to the size of the detector pixel. The XRD patterns were acquired on the whole electrode diameter and thickness so that each voxel was 300*300 μm^2 in the (x,y) plan perpendicular to the battery axis and 25 µm in the vertical direction, which corresponds respectively to 31*31 patterns per slice and 23 vertical layers (~22 000 patterns overall per time step).

A summary of the experimental set-up and conditions is shown in Table 2.

		1st experiment	2nd experiment	3rd experiment
		First coupling *operando* absorption tomography and XRD.	Characterization of the sulfur domains. Characterization of the negative electrode in the first discharge. Half cycle (on the first quasi-plateau).	Characterization of a complete cycle (both positive and negative electrodes). Different current densities and C-rate.
Tomography	Resolution	1.2 µm/pixel	3.18 µm/pixel	0.717 µm/pixel
	Area probe	1.2 mm in diameter	6 mm in diameter	1.8 mm in diameter
	Improvment		Phase contrast Better contrast Segmentation of sulfur particles possible	Phase contrast + Paganin Better contrast 3D analysis of sulfur particles
XRD	Resolution	Global resolution 20 µm in the z axis All (x,y) in plane	Local resolution 20 µm in the z axis 300*300 µm in the (x,y) in plane	Local resolution 25 µm in the z axis 300*300 µm in the (x,y) In plane
	Improvment		XRDCT	XRDCT (high quality data)

Table 2: Summary of the experimental set-up and conditions for the three experiments.

5.4. Data analysis

5.4.1. XRD data

5.4.1.1. Peak integration

The XRD peaks were integrated using the quadrature i.e. the midpoint rule. As this method is not the most accurate, another test has been done. For each XRD pattern a polynomial background were estimated under the peak and then subtracted. The remaining peak were fitted with a Gaussian-Lorentzien curve then the area of the curve was calculated. As the difference between this two methods of calculation give approximately the same results with an error lower than five percent, the midpoint rule was used for all the data due to the easier way to do it in such amount of XRD data.

5.4.1.2. XRDCT

As previously said, XRDCT allows spatial resolution in 3 dimensions. This is a powerful and very relevant tool to be used with using a 3D current collector. Another advantage is that this technic allows the acquisition of XRD patterns less influenced by the signal of the casing. By comparing the XRD pattern obtained from "classical XRD" and XRDCT, it is clear that the resolution is better in the second case (see Figure 10).

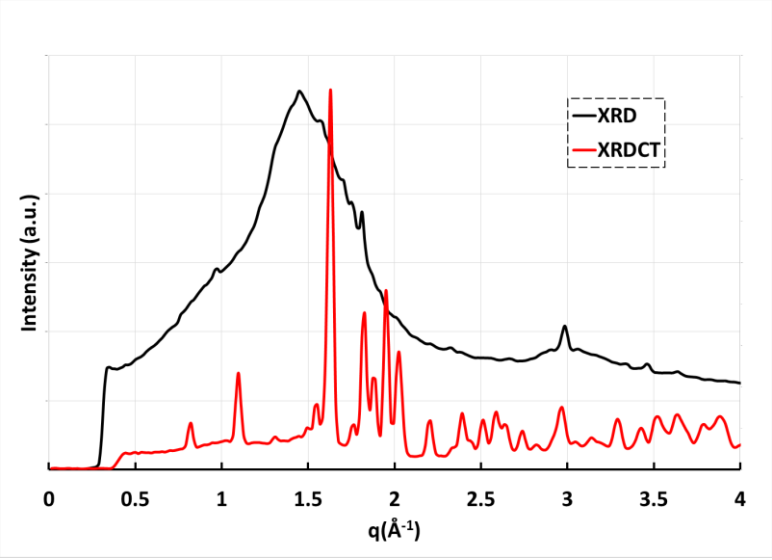

Figure 10: Comparison between XRD and XRDCT pattern of the positive electrode (sulfur). The XRD pattern goes through the entire layer and thus measures all the materials present, whereas the XRDCT pattern has been reconstructed only within the volume of interest, i.e. within the electrode itself.

The XRDCT data were analyzed in the same way as the XRD. The area of select sulfur peaks was integrated with the midpoint rule. A restricted zone representing solely the electrode was analyzed in each cell characterized. Two different methods have been used to deal with this data:

First methods:

This first one is to integrate, for instance sulfur peaks, in one "slice" defined by the beam size and look at the distribution of the peak in order to see the homogeneity of the species in one slice. This method was used to draw Red, Green, Blue, (RGB) maps in the chapters 3 and 4.

Second methods:

The second one is to follow the total amount of a species in one slice (by adding all the peaks area of one specie in "one slice") and follow this amount while cycling in order to draw kinetics law in each layer of the electrode for each crystalline species. This method was employed to draw kinetics laws in the chapters 3 and 4.

5.4.2. Tomography data

5.4.2.1. Sulfur electrode

The tomography data were reconstructed in a 3D volume and each tomogram can be cut in, for example, the (X,Y), (X,Z) and (Y,Z) planes in order to display 2D slices. The value of the intensity in the map is proportional to the electronic density of the voxel probe. Each tomogram was analyzed using Matlab and the ImageJ software.

5.4.2.1.1. Image treatment in the phase contrast mode

The cell was analyzed in either/or absorption or phase contrast mode. Indeed, with the phase contrast mode, is it possible to have a better contrast that those obtain in pure absorption mode. As previously said, with phase contrast mode, it is thus possible to visually segmented species which have a similar electronic density and so on similar absorption coefficient.

All the images were analyzed in the ImageJ software using different filters in order to obtain the desired segmented images. The image processing (for chapter 3) is detailed in the next paragraph.

For the chapter 3:

The raw images obtained in absorption and phase contrast mode are presented in Figure 11.

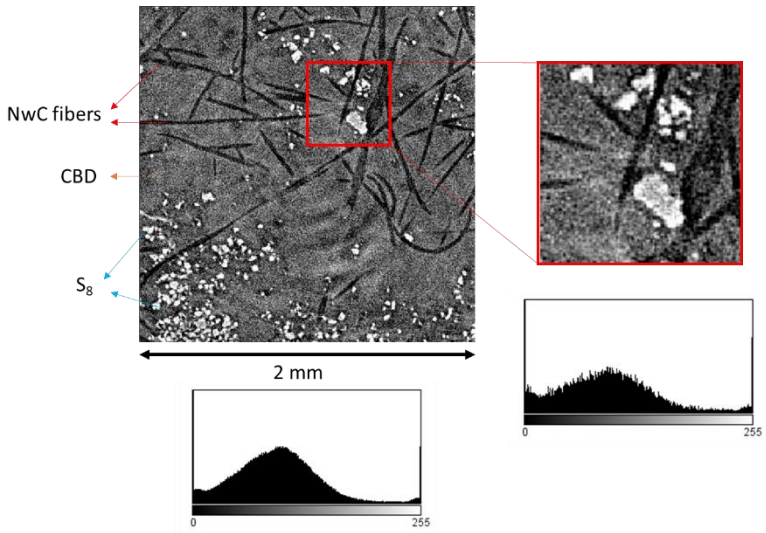

Figure 11: Raw images from absorption and phase contrast mode with the associate histograms.

These images in absorption and phase contrast mode show that it is possible to visually separate the carbon-binder domain (composed of carbon and PVdF) and the sulfur, even if the absorption coefficient, *i.e.* electron density of sulfur and carbon, are relatively close. However, as seen in the histogram, a simply greyscale treatment is not possible because pixels seem to fall within a Gaussian-like curve. That is why, different filters have been used in order to segment the images.

- *1st filter:*

The first filter is "Despeckle", it corresponds as a 3x3 mean filter. Each pixel was replaced by the median value of their 3x3 neighborhood. It enabled to suppress the "salt & paper" noise.

- *2nd filter:*

After that a plugin developed by the EPFL[9] was used. It is called Bi-Exponential Edge-Preserving Smoother (BEEPS). The aim is to transform an input image to an output image with the same size while enhancing contrast without blurring. The effect highlights objects without altering the edge of objects. The intensity of each pixel is a weighted average of nearby pixels. The range filter is a Gaussian-like and is controlled by a "standard deviation". On the one hand, a small standard deviation corresponds to a strong effect with a narrow range but keeping the edges highlighted. On the other hand, it is possible to weakly smooth all and preserve solely

the strongest edges. In the tomogram, sulfur particles edges are relatively well defined, however the inner part of a particle could be composed of different shades of grey. The aim is so to preserve the edge and smooth the inner part of the particle. That is why a relatively small standard deviation was used. The other parameter is the spatial decay. The lower is the value, the longer-range and stronger smoothing is the filter. This filter could be applied several times.

After testing several combination of parameters, these were fixed to 15 for the standard deviation, 0.01 for spatial decay and 6 iterations.

3rd filter:

After this a threshold based on shade of grey was used. It was fixed at (172,255), this means that all pixel above 172 were being blacked and all below being white (for the global segmentation of particles).

4th filter:

Finally, a binary processing has been applied which erodes and dilates pixels. It allows the suppression of the isolate pixels and the smoothing of the object.

All the image processing is summed up in Figure 12.

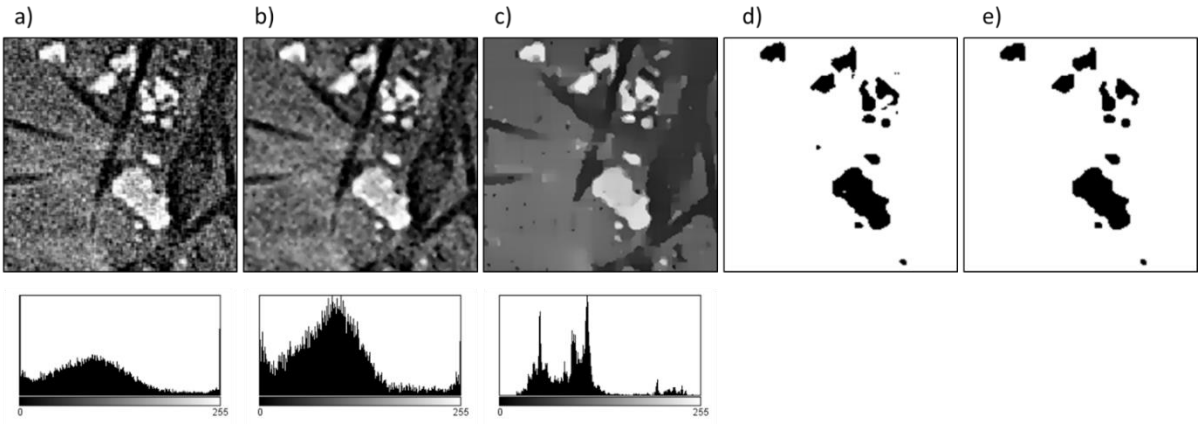

Figure 12: Positive electrode image treatment a) raw image, b) After despeckle, c) After BEEPS, d) After threshold, e) After open with the associate histogram.

After the image processing, in each tomogram, pixels representing sulfur were summed in order to draw sulfur kinetic reduction in the CBD.

5.4.2.1.2. Paganin mode

The use of absorption and phase contrast modes allow the better separation and visualization of the different objects, as seen in the previous section. However, the histogram of such a reconstruction shows that pixels are convolved with each other and thus the image treatment is relatively complicated. That is why, in the last experiment (chapter 4), Paganin[10] reconstruction has been done in order to make the segmentation easier. Figure 13 shows the interest of using such technics.

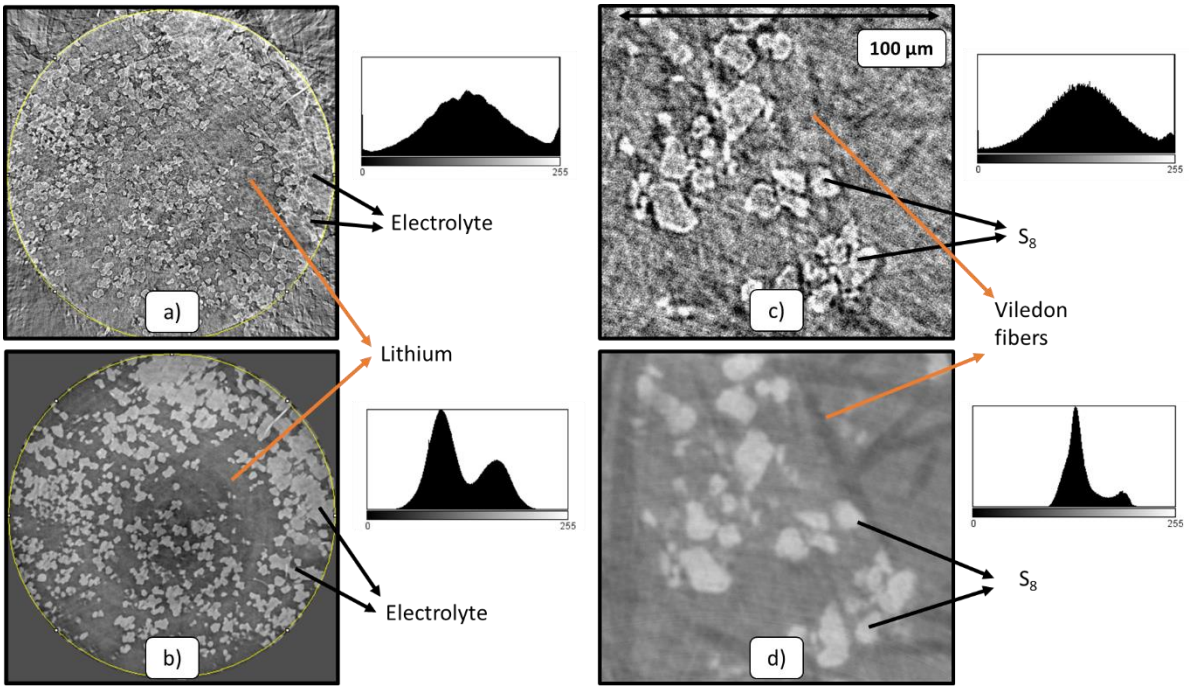

Figure 13: a) Phase contrast image of the lithium/electrolyte interface (end of discharge) , b) Paganin reconstruction of the same image (end of discharge). c) Phase contrast image of sulfur particle (initial state). d) Paganin reconstruction of the same image, with the associate histogram.

In the first image (Figure 13.a.), a horizontal slice with the associated histogram shows that the convolution of the pixels and the difficulty to carry out segmentation via grey levels. In the Paganin mode (Figure 13.b.), is it possible to separate the different phases/species and have a shade of grey "acceptable" for data treatment as shown in the histogram. This method will be beneficial for image analyzes and segmentation of sulfur. The "paganin parameter", which drives the phase contrast on an image, could be changed and different values of this parameters were tested in order to select the most relevant value allowing the better segmentation of the

image. A schematic explanation is shown Figure 14 where the ratio was varied from 0 to 500, 1000, 1500, 2500 and finally 10 000.

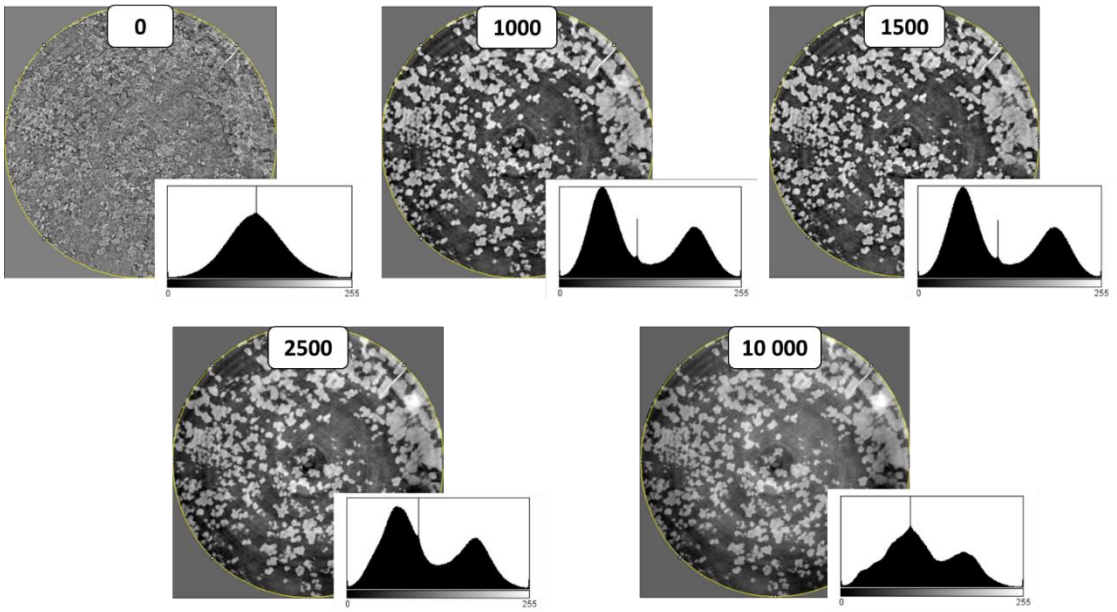

Figure 4 : Test of different Paganin parameters (0; 1000; 1500; 2500 and 10 000) and the associated histogram.

As the histograms show, above the value of 1000, there is a god separation of the grey levels. With a much higher values, 2500 and 10 000, some artefacts are added. That is why a value of 1500 was chosen because it corresponds to the best separation in the shades of grey histogram without adding artefacts.

For the chapter 4:

All the image in the last experiment (chapter 4) were treated in the Paganin mode with a parameter defined at 1500.

For the positive electrode, the same image processing has been performed. First, BEEPS filter, with standard deviation of 10 was performed twice. Then a threshold in shade of grey allow to segment the image and therefore a binary process was used to suppress the isolate pixels and smooth the object.

For the analysis particle by particle, restricted zones were chosen and the parameters of filter were tuned to segment the image as best as possible. After that, the plugins “Object counter” was used. It calculates separate objects by counting the number of pixel contained in each object.

5.4.2.2. Lithium electrode

5.4.2.2.1. Image treatment

For each experiment, the lithium thickness was measured by counting the number of pixel in the layer from the integrated 3D tomographic reconstruction. In order to make quantitative analysis, similar image processing as that done for the sulfur electrode has been carried out.

For the chapter 3:

1st filter:

"Despeckle" was used in order to median filter the images and suppress the "salt & pepper" noise.

2nd filter:

After that, a BEEPS filter has been applied. The standard deviation was chosen at 15 because the edge of lithium pits is quite well defined. In addition, as these edges were well defined, 10 iterations have been applied in order to completely smooth the interface.

3rd filter:

A threshold in shade of grey at 100 was implemented.

4th filter:

A "Close" and "Open" filter was used in order to suppress the "small" black and white isolate objects.

The summary of this image processing is shown in Figure 15.

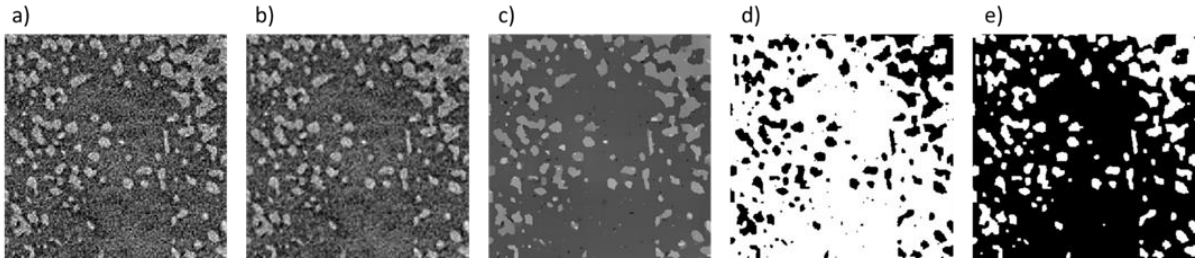

Figure 15: Segmentation of the lithium/electrolyte interface, a) Raw, b) After Despeckle, c) After BEEPS, d) After threshold, e) After Close & Open.

After slices were segmented, they could be stacked along z view in order to produce a 3D image of the interface, as shown in chapter 3.

For the chapter 4:

The images were analyzed thanks to the Paganin mode. A similar image processing to the one described in the previous section has been done.

1st filter:

BEEPS with a standard deviation of 10, applied twice. Thanks to Paganin mode, not so much iterations are needed.

2nd filter:

A threshold in shade of grey at 140 was implemented.

3rd filter:

A "Close" and "Open" filter was used in order to suppress the "small" black and white isolate objects.

After that, the obtained images could be quantitatively analyzed.

5.4.2.2.2. Roughness calculation

The roughness calculation, called "Ra" for arithmetical roughness, has been done with the plugin on ImageJ. The value is the representation of the mean value of the lithium pits without taking into account the number of pits (Figure 16).

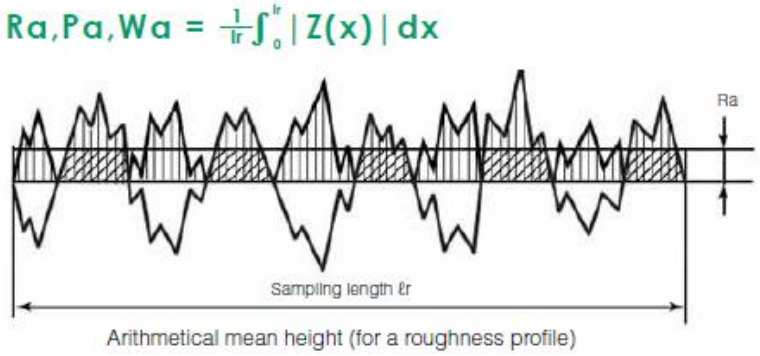

Figure 16 : Calculation method of the roughness parameters[11].

5.4.2.2.3. Local current density map

In order to draw a local current density map, a short automatic code has been written. The bottom of the electrolyte/lithium interface was taken as a reference (dashed lines in Figure 17), which corresponds to the lithium pits bottoms.

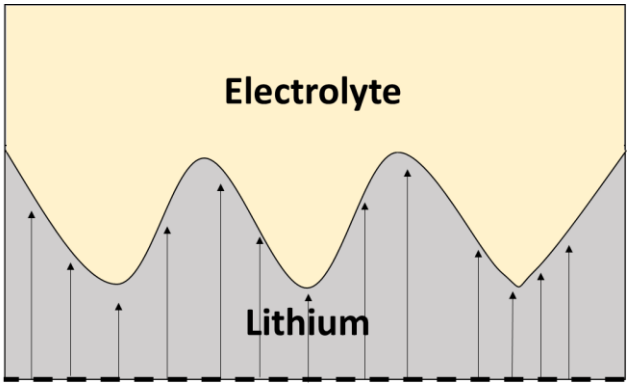

Figure 17: Schematic representation of lithium/electrolyte interface.

The pixels, representing the lithium pits, were probed and the distances between the bottom of the lithium layer (dash lines) and the interface were calculated in order to analyze the lithium pit depth (representing with arrow). Then a colormap was used to show the distribution of this distance in the in plane view.

For the chapter 3:

It was assumed that the distance between pixels and interface is linked to the local current density applied. The average local current density is represented in green and correspond to the mean of the expected lithium thickness oxidation. In other words, blue pixels correspond to areas which have been less oxidized than expected (thanks to coulometry) and the red pixels correspond to areas which have been more oxidized than expected. In this way, 2D maps of the heterogeneity of the interface could be drawn (Figure 18).

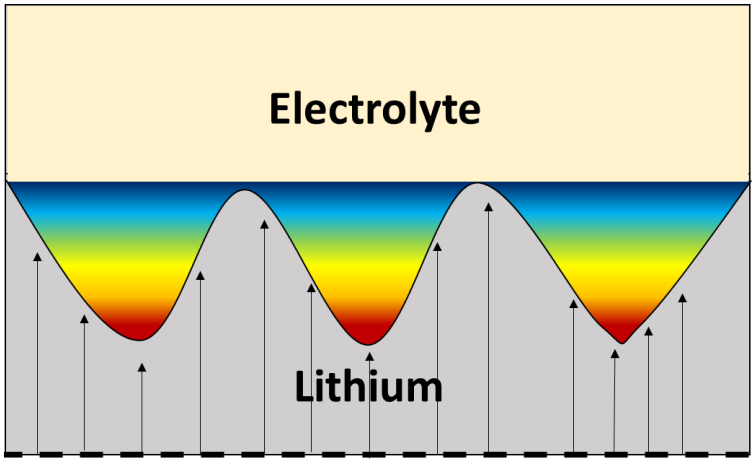

Figure 18: Schematic representation of the electrolyte/lithium interface with the colormap corresponding to the oxidation depth, i.e. local current density (for the chapter 3).

For the chapter 4:

The same image processes have been done in this chapter. Another colormap has been used to represent the interface. The same 2D maps have been shown. In addition, a 3D stack has been drawn in order to better see the zoology of the objects. Two representations have been shown to better visualize the objects (view from the red arrow), the "normal" one (Figure 19.a.) and the negative one (Figure 19.b.).

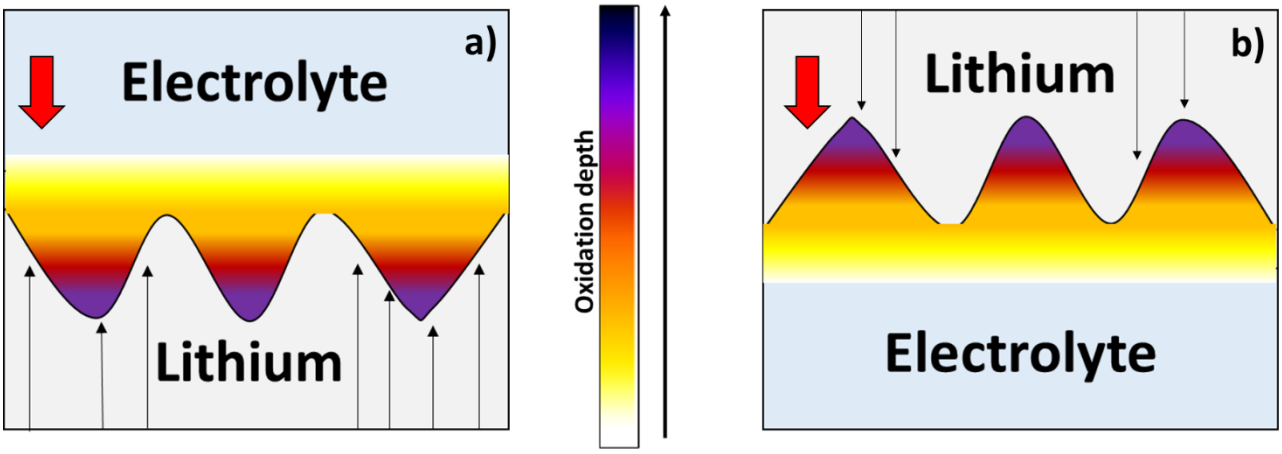

Figure 19: Schematic representation of the electrolyte/lithium interface with the colormap corresponding to the oxidation depth a) "normal" view, b) "negative" view.

References

[1] S. Walus, Accumulateur Lithium/Soufre : Développement et Compréhension Des Mécanismes Électrochimiques, PhD Thesis, **2015**.

[2] C. Barchasz, Development of Lithium-Sulfur Batteries, Theses, Université de Grenoble, **2011**.

[3] C. Barchasz, F. Molton, C. Duboc, J.-C. Leprêtre, S. Patoux, F. Alloin, *Anal. Chem.* **2012**, *84*, 3973.

[4] M.-K. Song, E. J. Cairns, Y. Zhang, *Nanoscale* **2013**, *5*, 2186.

[5] Y. Jung, S. Kim, *Electrochem. Commun.* **2007**, *9*, 249.

[6] G. Tonin, G. Vaughan, R. Bouchet, F. Alloin, M. D. Michiel, L. Boutafa, J.-F. Colin, C. Barchasz, *Sci. Rep.* **2017**, *7*, 2755.

[7] G. Ashiotis, A. Deschildre, Z. Nawaz, J. P. Wright, D. Karkoulis, F. E. Picca, J. Kieffer, *J. Appl. Crystallogr.* **2015**, *48*, 510.

[8] J. Kieffer, S. Petitdemange, T. Vincent, *J. Synchrotron Radiat.* **2018**, *25*, 612.

[9] "BEEPS," can be found under http://bigwww.epfl.ch/publications/thevenaz1202.html, **n.d.**

[10] D. Paganin, S. C. Mayo, T. E. Gureyev, P. R. Miller, S. W. Wilkins, *J. Microsc.* **2002**, *206*, 33.

[11] "Arithmetical Mean Height (Ra, Pa, Wa) | Surface Roughness Parameters | Introduction To Roughness | KEYENCE America," **n.d.**

Table of figures

Conclusions & Perspectives

The Li/S battery has attracted more and more attention in the last few years. Indeed, thanks to its high capacity, low environmental impact, availability of raw materials and expected low cost, it has been shown to be a good candidate as an alternative to current lithium-ion system. Nevertheless, this system suffers from several technological hindrances and constraints, which have so far limited the industrialization and commercialization of this technology. Despite the many advantages associated with the use of lithium metal as a negative electrode, such as high specific theoretical capacity and low electrochemical potential, it suffers from several issues, such as safety problems associated with dendrite formation and low cyclability due to heterogeneous lithium stripping/plating. Concerning the positive electrode, the morphological changes and the complex mechanisms occurring while cycling raise also issues leading to lowering the performances. However, numerous characterization tools have been used to better understand the system and to identify the degradation phenomena occurring while cycling, but with lack of spatial and/or temporal resolutions. One solution is to perform *operando* characterization on both the sulfur and lithium electrodes with 3D characterization tools such as absorption and X-ray diffraction tomography allowing to probe the crystalline species involved and the morphological changes while cycling.

This thesis was focused on characterizing a Li/S system by both absorption and X-ray diffraction tomography, in *operando* mode. The first cycle was characterized in depth because large irreversible changes occur during this cycle which have consequences on further cycles. Different cell configurations and cycling conditions were also evaluated.

A new adapted *operando* cell design has been developed to be suitable with synchrotron experiment such as XRDCT and absorption tomography. The aim was to reduce the cell cross-section while keeping representative electrochemical performance. Despite the success in characterizing the first generation of *operando* cells made with aluminum crucibles, a lack of control of the pressure on the electrode stack was identified and has probably exacerbated certain phenomena. That is why a second generation of *operando* cell design has been developed in order to be as close as possible to coin cell characteristics in terms of pressure and electrolyte quantity. The pressure applied on the stack has been fixed at 1.2 bar and controlled by spring compression. This allowed the cell to be comparable to coin cells but also capable of performing XRDCT with the high speed continuous rotation needed thanks to slip ring contact. Finally, a last generation of cell has been developed by welding the electrical contacts on the

pistons which enabled to perform XRDCT during a complete cycle despite the high rotation speed required, and kept representative electrochemistry.

The XRD technique allowed the following of the crystalline species while cycling and showed that there is a linear decrease in sulfur quantity which corresponds to a unique electrochemical reduction of sulfur. The sulfur amount vanishes at 210 $mAh.g_s^{-1}$ which is in good accordance with the theoretical value and proves a total utilization of the initial sulfur. Using XRDCT, the distribution of the sulfur at the initial state was found to be a bell-shaped curve resulting from the doctor blading process where most of the material is contained in the carbon binder domain (CBD) at the top of the current collector. The sulfur also penetrates into the 3D current collector to approximately 100 to 120 µm depth, depending of the electrode loading and the ink viscosity. Phase contrast and absorption tomography allows also the measurement of the distribution of sulfur particles with a resolution on the order of micrometers compared to 20-25 µm for XRDCT. The distributions are similar to those obtained with XRDCT but there exists a plateau in the sulfur distribution (along the depth of the electrode) such that the sulfur amount reaches a maximum concentration at 40 µm depth between the CBD and the top of the NwC. The distribution showed that the 3D composite electrode is heterogeneous in terms of composition and sulfur amount. Even if the evolution of the whole electrode can be seen by XRDCT and absorption tomography to be linear with time, there is a kinetic gradient of sulfur consumption and formation along the depth of the electrode. Indeed, by going deeper in the electrode, the kinetic of sulfur reduction is diminished compared at the electrode surface (in contact with the separator). This behavior, during the discharging process, may be due to the limitation of sulfur reduction by the lithium ion diffusion through the electrode.

To further extend the study, high resolution absorption tomography (0.717µm/pixel) coupled with the Paganin mode was performed allowing to probe separated particles in the depth of the electrode. This analysis showed that particles taken at different depths seem to have a similar evolution, in terms of volume reduction. However, even with high resolution, it was difficult to perform a 3D complete analysis without the use of complex and non-automated image filtering The reduction of the sulfur particle is also associated with an increase of porosity in the carbon-binder domain (CBD), which collapses due to the spring pressure. However, the rigid carbon matrix of the 3D current collector (NwC) keeps its morphology while cycling, and allows the

maintenance of a good electrochemical performance despite the morphological changes of the CBD. After the sulfur vanished, a soluble domain is observed, associated to the 200 $mAh.g_s^{-1}$, before the formation of the Li_2S discharge product.

The Li_2S distribution showed a higher concentration on the top of the current collector thanks to high conductive surface area available, but Li_2S also precipitates deeper into the electrode compared to the initial sulfur. This behavior could be attributed to the diffusion of anionic species S_4^{2-} & S_2^{2-}, which homogenize the PS concentration in the electrode depth, and to the large surface area needed to precipitate the insulating species Li_2S. This leads to a deeper precipitation of Li_2S into the electrode. The Li_2S formation is linear *vs* the capacity for the whole electrode but a shift in time has been observed. In other words, it takes a certain time to nucleate and form Li_2S in the depth of the electrode, but when the first crystallites of Li_2S are produced the formation kinetics are similar in the different layers. In addition, a quantitative analysis has given an estimation of the Li_2S and Li_2S_2 formation. This has shown that only a low percentage (~14%) of Li_2S is really formed and main of the product formed seems to be Li_2S_2. This is probably due to the lithium diffusion through the bulk of the electrode, which limits the nucleation of Li_2S in comparison to Li_2S_2 formation in the depth of the electrode. The Li_2S formation is also driven by the insulating nature of Li_2S, inducing a passivation layer on the top of the current collector and the weak solubility of the Li_2S_2. The Li_2S disappearance has different kinetic reactions in the depth of the electrode and is attributed to lithium ions diffusion through the electrode, where the upper region reacts preferentially and quickly than the deeper one. The Li_2S totally vanishes while charging the cell and the formation of the known beta-sulfur phase is then observed. While recharging the cell, the beta-sulfur is produced but with a smaller particle size than the initial sulfur and is redistributed more sparsely in the NwC. The particles seem to be organized in large agglomerates on the top of the current collector. In the next cycle, the sulfur quantity seems to be relatively low with reduced particle size, maybe due to the increase of current density. It proves also that the sulfur is not fully utilized and there is a possible loss of active material due to the electrolyte loss along the piston.

The characterization with absorption tomography on a complete cycle allowed to quantitatively analyze the evolution of the lithium metal electrode in a pressure controlled cell and during a complete cycle. The initial lithium layer is dense and homogenous. However, while discharging

the cell, the lithium foil oxidation is done in a heterogeneous way with pits formation along the interface. Indeed, the surface roughness rapidly increases from the beginning of the discharge. The surface roughness and heterogeneity are driven by the current density applied. With high current density (up to 0.4 $mA.cm^{-2}$), pits of 30 µm in depth are observed at the interface. However, the pit depth seems to reach the same maximum value even by doubling the current density. With lower current density (lower than 0.23 $mA.cm^{-2}$), a more homogenous oxidation takes place but there is still formation of small pits. The heterogeneous oxidation of lithium layer seemed to begin at the grain boundaries of the metallic foil. During the charging process, lithium is plated preferentially in the pits formed during the previous discharge, in a mossy form, which leads to highly developed surface. It has also been demonstrated that, with the cell in which the pressure was not controlled, a large increase of the lithium electrode thickness was observed while plating, with a relative low density (17%) due to the formation of a moss which is electrochemically inactive in the next cycle. This large increase was notably reduced by controlling the pressure applied on the cell.

In the subsequent discharge, the oxidation is dependent on the previous cycle and the interface becomes more heterogeneous with pitting-like oxidation in the whole surface.

The perspectives of this work is notably to help improving the architecture of the current collector. Indeed, the NwC has been shown to be a good current collector thanks to its good mechanical properties, and allows to ensure a good stability in terms of performances. Improvements in terms of weight and thickness could be achieve because the NwC is heavy and not optimum in terms of thickness. In addition, the porosity, size of carbon fibers and tortuosity could be improved to allow reaching the better value of volume/surface ratio, developed surface area and better ionic and electronic conduction. Furthermore, work on the CBD in order to improve its mechanical properties would also contribute to the improvement of cycle life. In addition, it could be interesting to encapsulate the sulfur into a 3D matrix in order to keep the sulfur active material within the positive electrode, or even force the penetration of all sulfur in the current collector without forming a crust on the top, by for example melting the sulfur and impregnating the current collector. Last but not least, work on the electrolyte in order to perfectly tune the viscosity and the ionic conduction in order to increase the lithium ion diffusion through the electrode thickness could be done.

Different strategies could be applied to the lithium metal electrode. An increase of the surface roughness by implementing a pattern on the surface could improve the distribution of the current density, and thus a lower local current density applied on the lithium metal electrode. A lithium surface treatment such as coating of a thin layer of lithium ion conductor could be also a good solution to avoid the formation of pitting-like oxidation. In that way, having lithiophilic sites[1] on the interface could allow to control the oxidation and deposition processes of the lithium electrode.

This works suggests several perspectives on characterizing the Li/S system. Indeed, both positive and negative electrodes were characterized but there is a lack of electrolyte characterization while cycling in a real system, whereas a part of electrochemical reactions are taking place in solution. One possible characterization technique could be Pair Distribution Function (PDF) analysis. This technique uses the XRD patterns acquired during the experiment, but focuses on the treatment of the entire scattering within the XRD patterns. PDF is essentially the Fourier transform of the scattering pattern, and gives the probability of finding an interatomic distance between atoms, regardless of whether they are found in crystalline or amorphous phases, or even in solution. Indeed, it is possible to find the interatomic distances between lithium/lithium, lithium/sulfur and sulfur/sulfur and the proportion of both. Using XRDCT, it could be possible to reconstruct a PS "mean" profile in each voxel of the electrolyte and thus see the possible gradient of PS along the depth of the electrode and in between the two electrodes.

In addition, it would be interesting to have a complete 3D analysis thanks to absorption and phase contrast tomography by developing a systematic and automatic image processing allowing particle by particle characterization, and have sufficiently high statistics to allow the understanding of the dynamic processes at the particle scale. This would allow a complete analysis from the global evolution (electrochemistry), to "layer by layer" evolution and finally to the particle scale. Moreover, looking at cells which have done prolonged cycling could also be interesting to see the heterogeneity evolution both on the morphology of the positive electrode but also on the lithium/electrolyte interface.

Finally, this complex system still has technological limitations but it seems possible to improve cell performances by taking into account knowledge obtained from the understanding of the mechanisms and identifications of degradation phenomena as demonstrated in this thesis work.

Caractérisation *operando* des accumulateurs Li/S par tomographie d'absorption et diffraction des rayons X, vers une meilleure compréhension des mécanismes électrochimiques.

L'objectif principal de la thèse était d'identifier les processus limitants et les phénomènes de dégradation intervenant lors du cyclage d'un accumulateur Li/S, et d'expliciter l'évolution des performances électrochimiques au cours du temps. Pour ce faire, une cellule électrochimique a été développée permettant de réaliser des caractérisations à l'ESRF par diffraction et absorption des rayons X en mode *operando*. Ces deux techniques complémentaires ont permis de mettre en évidence des changements morphologiques importants et des cinétiques de réactions limitées par le transport de matière au sein de la structure 3D de l'électrode positive de soufre. L'oxydation/réduction de l'électrode négative de lithium a également été caractérisée, permettant de mettre en évidence une évolution hétérogène de l'interface lithium/électrolyte, fonction de la densité de courant induisant une diminution des performances électrochimiques en cyclage.

Li/S accumulators: Electrochemical mechanism investigation using *operando* analysis by absorption and X-Ray diffraction tomography.

The main objective was to identify the degradations phenomena and the limiting processes occurring while cycling Li/S accumulators to therefore put in relation the electrode morphology, the cell design, the electrochemical performances and the degradations phenomena. A new design of *operando* cell has been developed to be suitable with ESRF experiments. *Operando* Absorption and X-ray Diffraction tomography technics were performed. Thanks to both technics, the morphological changes and transport limitation kinetics along the 3D positive electrode have been evidenced. In addition, the lithium electrode/electrolyte interface has been characterized and heterogeneous stripping/plating has been evidenced, leading to low electrochemical performances while cycling.